BIBLIOTHEQUE
CERN
1 5 OCT. 1960

UCRL 9194

UNIVERSITY OF CALIFORNIA

CERN LIBRARIES, GENEVA
P00037156

Ernest O. Lawrence

Radiation Laboratory

PHOTOPION PRODUCTION FROM DEUTERIUM NEAR THRESHOLD

BERKELEY, CALIFORNIA

Thesis-1960-Swanson

UCRL-9194
UC-34 Physics and Mathematics
TID-4500 (15th Ed)

UNIVERSITY OF CALIFORNIA
Lawrence Radiation Laboratory
Berkeley, California

Contract No. W-7405-eng-48

PHOTOPION PRODUCTION FROM DEUTERIUM NEAR THRESHOLD

William P. Swanson

(Thesis)

April 1960

134/

2213238

Printed in USA. Price $2.50. Available from the
Office of Technical Services
U. S. Department of Commerce
Washington 25, D.C.

Contents

Contents (continued)

Contents (continued)

PHOTOPION PRODUCTION FROM DEUTERIUM NEAR THRESHOLD

William P. Swanson

Lawrence Radiation Laboratory
University of California
Berkeley, California

ABSTRACT

The reactions (1) $\gamma + d \rightarrow \pi^- + 2p$ and (2) $\gamma + d \rightarrow \pi^+ + 2n$ have been observed near threshold by using the Lawrence Radiation Laboratory electron synchrotron and a 4-inch deuterium bubble chamber modified for operation in a high-energy photon beam. A 194-Mev bremsstrahlung beam, hardened by one radiation length of LiH, with an average intensity $0.8 \cdot 10^6$ Mev/pulse, was incident on the chamber. A total of 1309 analyzable π^- and 447 π^+ events was found in 200,000 photographs. The events were kinematically analyzed by an IBM 650 computer using a least-squares method. Two-prong events were weighted for chamber geometry by an IBM 704 computer using a Monte Carlo technique. The ratios σ^-/σ^+ were determined as a function of laboratory-system photon energy k and meson c.m. angle θ (two-body kinematics): by connecting observed ratios of reactions (1) and (2) for final-state Coulomb effects:

k (Mev)	θ (deg)	σ^-/σ^+
152-158	0 to 90	1.08 ± 0.14
158-165	90 to 140	1.27 ± 0.18
165-175	135 to 180	1.44 ± 0.20

These ratios include negative Coulomb corrections of 13%, 7%, and 7%, respectively. An attempt was made to obtain the free-nucleon cross sections ($\gamma + n \rightarrow \pi^- + p$) by using the Chew-Low technique of

extrapolating data from Reaction (1) to a pole in the transition amplitude located at a negative (nonphysical) value of the kinetic energy of the lower-energy proton in Reaction (1). Straight-line extrapolations at five effective laboratory-system photon energies in the range k = 153 to 174 Mev gave an average value $\sigma^-/\sigma^+ = 1.7 \pm 0.2$ when compared with recent positive photomeson data. Total and differential cross sections for Reaction (1) were obtained for the photon energy range k = 150 to 157.5 Mev. The data are lower than those of Adamovich et al. by approx. 32%. They are consistent with isotropy in the $(\gamma + d)$ c.m., but there is a strong suggestion of a negative $\cos^2\theta^*$ term in the angular distribution.

I. INTRODUCTION

A. R, the Photopion σ^-/σ^+ Ratio

Every reasonable meson theory that includes nucleon recoil has led to the conclusion that the processes $\gamma + n \rightarrow \pi^- + p$ and $\gamma + p \rightarrow \pi^+ + n$ should occur at threshold in the ratio R = 1.3 to 1.4 if final-state Coulomb interactions are excluded. This result comes about regardless of the details of the meson-nucleon interaction assumed. For this reason it would be of major theoretical importance if it were found experimentally to be otherwise. Since a firm experimental value of R has proven to be elusive,[1-15, 91] the research described here was undertaken to measure the apparent value of R near threshold by using deuterium as a target, and to obtain information on the $\gamma + d \rightarrow \pi^- + 2p$ final state, useful in relating the apparent (deuterium) ratio to R itself. In addition, an attempt was made to obtain the free-nucleon cross section $\sigma(\gamma + n \rightarrow \pi^- + p)$ in a way that eliminates deuteron binding effects and kinematical smearing, by means of a Chew-Low extrapolation.[16]

Naively, one would expect the cross sections $\sigma^- \equiv \sigma(\gamma + n \rightarrow \pi^- + p)$ and $\sigma^+ \equiv \sigma(\gamma + p \rightarrow \pi^+ + n)$ to be about equal, on the basis of charge independence. That negative mesons in fact are photoproduced with higher probability near threshold may be crudely grasped by noting that a neutron, when viewed as a virtual proton—negative-meson system, has an electric dipole moment proportional to $(1 + \mu/M)$, whereas a proton viewed as a neutron—positive-meson system has a dipole moment proportional only to unity, as illustrated in Table I. The cross sections are proportional to the squares of the interactions of these virtual dipoles with the incident photon. Significantly, $(1 + \mu/M)^2 = 1.32$, in agreement with more sophisticated theories.

Table I

Nuclear virtual dipole moments

Virtual process	Position of particles: -1	0	$+\mu/M$	Dipole moment
$n \to \pi^- + p$	π^-	Center-of-mass	p^+	$(1 + \mu/M)$
$p \to \pi^+ + n$	π^+		n^0	$(1 + 0)$

The earliest predictions concerning the ratio **R** were obtained by considering the final-state currents only.[17] The interaction may be expressed as $\int \vec{j} \cdot \vec{A}\, d\tau\, dt$, where the integral is taken over all space and time. Assuming the cross section to be proportional to the square of the appropriate interaction, we have the result

$$\frac{\sigma^-}{\sigma^+} = \left[1 - \frac{\omega}{M}(1 - \beta\cos\theta)\right]^{-2} = 1.38, \text{ for } \omega \to 1 . \qquad (1)$$

Here, μ is the meson total energy, M is the nucleon mass, and β is the meson velocity ($\hbar = c = \mu = 1$). This formula was also derived from first-order perturbation theory.[18]

On the other hand, an interaction between the photon and the nucleon magnetic moments leads to[18]

$$\frac{\sigma^-}{\sigma^+} = \left[1 - \frac{g_p + g_n}{g_p - g_n}\,\frac{\omega}{M}\,(1 - \cos\theta)\right]^{-2} = 1.06 \text{ for } \omega \to 1, \qquad (2)$$

where g_p and g_n are the nucleon total magnetic moments, in nuclear magnetons. A phenomenological approach by Watson, based on measurements of the ratio at higher energies,[7] also led to a threshold value $R = 1.24$. These arguments, whether semiclassical or based on perturbation theory, lead to results in qualitative agreement with experiment. Actually, the recoil-current interaction gives values generally too large, and the magnetic-moment interaction gives results closer to unity than is the case experimentally, since $(g_p + g_n)/(g_p - g_n) \approx 0.2$. The increase in σ^-/σ^+ with meson angle, which is experimentally true[19] up to around 1 Bev photon energy, is indicated by these semiclassical results.

Dispersion theory,[20] much more reliable than the older perturbation calculations, gives the ratio

$$R = \frac{\sigma^-}{\sigma^+} \left[\frac{1 + (g_p + g_n)/2M}{1 - (g_p + g_n)/2M}\right]^2 = 1.30 \quad \text{for} \quad \omega = 1, \tag{3}$$

consistent with all earlier theories that include nuclear recoil. Actually, that the semiclassical and perturbation theories are in such close agreement with the dispersion relations is perhaps fortuitous. The disperion relations approach to photoproduction is considerably sounder than the other theoretical attempts described above.

The basis for confidence in this result is that, apart from recoil effects which are essential in determining R, the important terms in near-threshold photoproduction are the gauge-invariance term $\vec{\sigma} \cdot \hat{\epsilon}$ and the direct-interaction term $\dfrac{\vec{\sigma} \cdot (\vec{k}-\vec{q})\ \hat{\epsilon} \cdot q}{\omega k_0 - \vec{q} \cdot \vec{k}}$. Here $\vec{\sigma}$ is the nucleon spin, $\vec{k}$ the photon momentum, k_0 the photon energy, $\vec{q}$ pion momentum, ω the pion total energy, and $\hat{\epsilon}$ the photon polarization direction. These terms are classical in origin and are not as mysterious as terms which become important only at higher energies. Their inclusion in any theory can hardly be avoided.[21] Moreover, general low-energy theorems add weight to the theoretical results. The Kroll-Ruderman theorem[22, 23] gives $R = \left(\dfrac{1 + x}{1 - x}\right)^2$, where x is of order (μ/M).

Thus, the prediction R = 1.3 to 1.4 is seemingly based on very strong theoretical grounds. However, it must be pointed out that theoretical corrections to Eq. (3), which may alter our expectations concerning R, have recently been estimated by Ball.[24] He obtained the form

$$R = 1.28\,(1-0.19\ \Lambda\,), \tag{4}$$

where Λ is the parameter which arises in the photon—three-pion interaction.[25] The magnitude of Λ may be derived from data or positive and neutral photopion production, and from measurements of the neutral-pion lifetime. Such data as exist are not inconsistent with a value of Λ as large as unity.

B. The Low-Energy Parameters

Apart from specific assumptions concerning meson theory, there is a basic connection between the experimental parameters of low-energy pion physics.[26] An apparent inconsistency among these parameters has been the source of much discussion in recent years.[27-39] The first of these parameters is $R = \dfrac{\sigma(\gamma + n \to \pi^- + p)}{\sigma(\gamma + p \to \pi^+ + n)}$, measured at threshold and excluding the final-state interactions, as defined in the preceding section. The second is the Panofsky ratio

$P = \dfrac{\sigma(\pi^- + p \to \pi^0 + n)}{\sigma(\pi^- + p \to \gamma + n)}$, determined by allowing negative pions to stop in hydrogen. The reaction takes place from an S state, and thus the pions are at slightly below zero kinetic energy. Experimental values of P have fluctuated widely from one investigation to another, but several recent experiments have given consistent results. A noncritical weighted average of seven experiments[32, 40-45] gives $P = 1.63\pm0.05$. Using this together with the theoretical value $R = 1.30$ gives $PR = 2.12$.

Now if we rearrange the factors in the product of these ratios, we obtain

$$PR = \frac{\sigma(\gamma + n \rightarrow \pi^- + p}{\sigma(\pi^- + p \rightarrow \gamma + n)} \cdot \frac{\sigma(\pi^- + p \rightarrow \pi^0 + n)}{\sigma(\gamma + p \rightarrow \pi^+ + n)} . \quad (5)$$

By detailed balance, the left-hand brackets simply contain $\frac{q^2}{2k^2}$, where the 2 comes from the two possible polarizations in the case of an outgoing photon. Here, q and k are the center-of-mass pion and photon momenta, respectively ($\hbar = c = \mu = 1$). The quantities $\sigma(\pi^- + p \rightarrow \pi^0 + n)$ and $\sigma(\gamma + p \rightarrow \pi^+ + n)$ are to be obtained from experiment and extrapolated to zero pion kinetic energy.

Experimental results on positive photopion production[8, 16, 46-52] near threshold have recently undergone revision due to new experiments[49-53] and new techniques[30] in extrapolating existing data which take into account the important direct-interaction term.[54] The extrapolated value

$$\lim_{\omega \rightarrow 1} \frac{d\sigma}{d\Omega} = (20 \pm 10\%) \times 10^{-30} \frac{q}{(1 + 1/M)^2} \frac{cm^2}{sr},$$

or $\sigma \approx 0.19q$ mb, is based on data compiled by Bernardini.[38] Here ω is the meson total energy, and M is the nucleon mass ($\hbar = c = \mu = 1$). This result is not in disagreement with the dispersion relations of Chew, Goldberger, Low, and Nambu,[20] for $f^2 = 0.074$, and $N^{(-)} = 0$ to -0.05.

Extrapolation of the charge-exchange data is done by means of the expression[55]

$$\sigma(\pi^- + p \rightarrow \pi^0 + n) = \frac{8\pi}{9} \frac{1}{q^2} \frac{v_o}{v_-} (\delta_3 - \delta_1)^2 , \quad (6)$$

and depends critically on the S-wave scattering phase-shift difference $(\delta_3 - \delta_1)$. P waves are neglected. Here, v_0/v_- is the ratio of velocities of outgoing neutral meson and incoming negative meson. Older extrapolations assumed $\frac{\delta_3 - \delta_1}{q}$ to be independent of ω near threshold. A fit made by Orear[56] to existing data, using this assumption, gave $(\delta_3 - \delta_1) = (0.26 \pm 0.04)\, q$. However, Cini et al.[36] have pointed out that the charge-exchange amplitude must vanish for zero pion energy, and therefore a value lower by 10% is preferable. Near threshold, $(\delta_3 - \delta_1) = 0.24\ q$ is the value they obtained by means of an S-wave effective range approximation based on dispersion relations.

Fitting these parameters together, we get PR = 1.89 for the left side of Eq. (5). This is gratifyingly close to 2.12, realizing that a straightforward use of experimental data gave PR = 3.27 only two years ago,[30] in serious disagreement with accepted P and R values. Although the threshold discrepancy is not serious now, further study of the pion-nucleon S state is desirable.

C. Photoproduction from Deuterium

Experimentally, the simplest way to get information on the reaction $\gamma + n \rightarrow \pi^- + p$ is by studying the reaction $\gamma + d \rightarrow \pi^- + 2p$ either directly or by observing the ratio of negative to positive mesons produced. Either method presents difficulties due both to three-body kinematical smearing and to the final-state nuclear and Coulomb interactions. The final-state nuclear interactions should be identical for negative and positive mesons, but the Coulomb forces are not identical, because three charged particles are present in negative-meson production and only one in the positive-meson case. The Coulomb correction is important for the low-relative velocities near threshold.

In the energy region $k \leqslant 200$ Mev, experiments on the ratio have been performed by several groups.[1-8, 10-12] In the region ($k \leqslant 175$ Mev) where corrections due to final-state Coulomb interactions should be small, the observed ratio is on the order of 1.4 to 1.5, as shown in Fig. 1. At lower photon energies (k = 160 to 165 Mev), the apparent (uncorrected) ratio rises to around 2. Two-body kinematics are assumed in determining the photon energy.

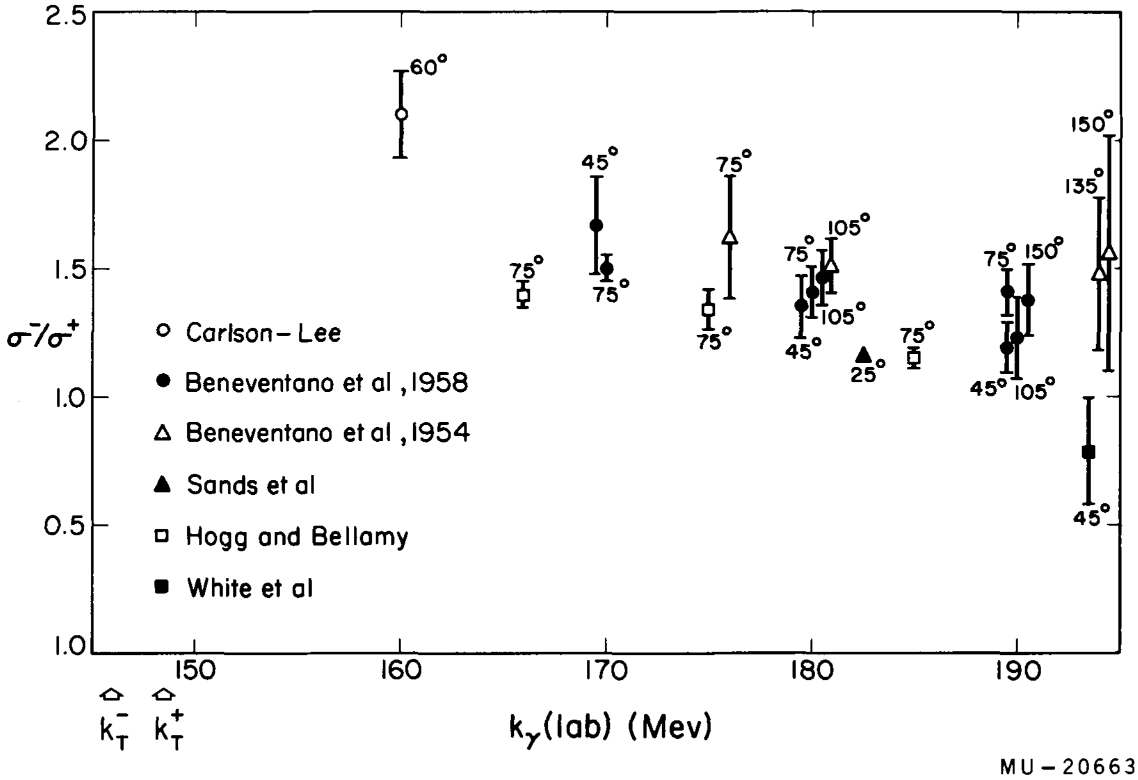

Fig. 1. Apparent values of σ^-/σ^+ obtained in deuterium as a function of photon energy k. Two-body kinematics are assumed. Angles are in the laboratory system. No corrections for Coulomb effects have been made.

Theoretical approaches to deterium photoproduction have usually utilized the impulse approximation.[57-59] This approximation assumes that the production amplitudes from the two nucleons can be linearly superposed. This assumption is valid if the distance between the nuclei is large compared with the production amplitudes, the time of interaction is short with respect to a nuclear period, and the interaction distance in nuclear matter for incoming photon and outgoing meson are long compared with the nuclear size. All these criteria apply to deuteron photopion production.

The most complete theoretical study of deuteron photomeson production via the impulse approximation has been made by Baldin.[33,34] He took into account final-state nuclear interaction of the two recoiling nucleons, and the Coulomb interactions of all recoiling particles. His work makes definite predictions concerning the recoil-proton distributions, which agree with the experimental work of Adamovich et al.[6,13-14] When his corrections are applied to the total cross sections $\sigma(\gamma + d \rightarrow \pi^- + 2p)$ as measured by Adamovich et al., and these results are compared with the cross sections[8] $\sigma(\gamma + p \rightarrow \pi^+ + n)$, the result **R** = 1.3 to 1.4 is obtained, in agreement with theory.

When the Baldin corrections are applied to the apparent ratios from deuterium at low energies, results consistent with theory are again obtained.[15] However, the agreement at low energy should perhaps be regarded as tentative until discrepancies with dispersion relations at higher photon energies are resolved[10] and the connections between **R** and other pion phenomena through the parameter $\underset{\sim}{\mathbf{\Lambda}}$ are more fully explored.

D. Polology

A powerful technique suggested by Chew and Low[16] has made it possible to determine free-nucleon cross sections $\sigma(\gamma + n \rightarrow \pi^- + p)$ by using the neutron bound in the deuteron as a target. This method depends upon an extrapolation of observed cross sections to a negative (nonphysical) value of the recoil-proton kinetic energy. The essential role played by a pole in the S matrix has lent the name Polology to this method of analysis.

The technique may be visualized in the following way. Imagine an incident photon striking the neutron at a time when the proton is far away. That part of the complete photoproduction amplitude A arising from interaction of the photon with the neutron alone to produce a negative pion is proportional to the T matrix for the process $\gamma + n \rightarrow \pi^- + p$ multiplied by the Fourier transform $(\alpha^2 + p^2)^{-1}$ of the deuteron asymptotic wave function. Here $\alpha = \sqrt{(B.E.) \times M}$ is the inverse deuteron radius and p^2 is the square of the spectator proton recoil momentum. Owing to this transform there is a first-order pole which determines the behavior of the complete amplitude A near $p^2 = -\alpha^2$. The residue of the pole, proportional to T, can be found by extrapolating measured values of A multiplied by $(p^2 + \alpha^2)$ to $p^2 = -\alpha^2$. At this point the spectator proton has a negative kinetic energy in the final state just equal to its share of the (negative) deuteron binding energy in the initial state. Thus, the recoil proton truly becomes a spectator at the extrapolated point.

Small values of proton recoil momentum mean little interaction between the proton and the other reacting particles. As pictured here, this situation corresponds to the case in which photoproduction occurs on the neutron when the proton is far away. Since low-momentum recoil events have most effect on the extrapolation, we were in retrospect justified in using the deuteron asymptotic wave function to obtain the Fourier transform.

Experimentally, what we observe is a complicated differential cross section $\frac{\partial^2\sigma}{\partial p^2 \partial w^2} \propto A^2$, rather than A itself. Here, p is again the recoil momentum of the spectator (lower-kinetic-energy) proton, and w is the total internal energy of the $\pi^- + p$ system. Clearly p^2 and w^2 have physical limits depending on the photon energy k, as illustrated in Fig. 2. The differential cross section is formed in the conventional way by counting events in various Δp^2, Δw^2 bins, on a graph such as Fig. 2.

Free-nucleon cross sections are obtained as a function of w^2 by using the formula

$$\sigma(\gamma + n \rightarrow \pi^- + p) = \lim_{p^2 \rightarrow -\alpha^2} \frac{4\pi k^2}{\Gamma^2} \frac{M_D}{M_p} \frac{(p^2+\alpha^2)^2}{(w^2-M_n^2)} \frac{\partial^2\sigma}{\partial p^2 \partial w^2} , \tag{7}$$

where w^2 corresponds to a definite value of effective laboratory-system photon energy. Here $\Gamma^2 = \frac{4}{M_p} \frac{\alpha}{1 - \alpha r_0}$, where r_0 is the neutron-proton triplet effective range. As can be judged from Fig. 2, the distance over which the extrapolation must be made is not long compared with the physical range of p^2 generally observable.

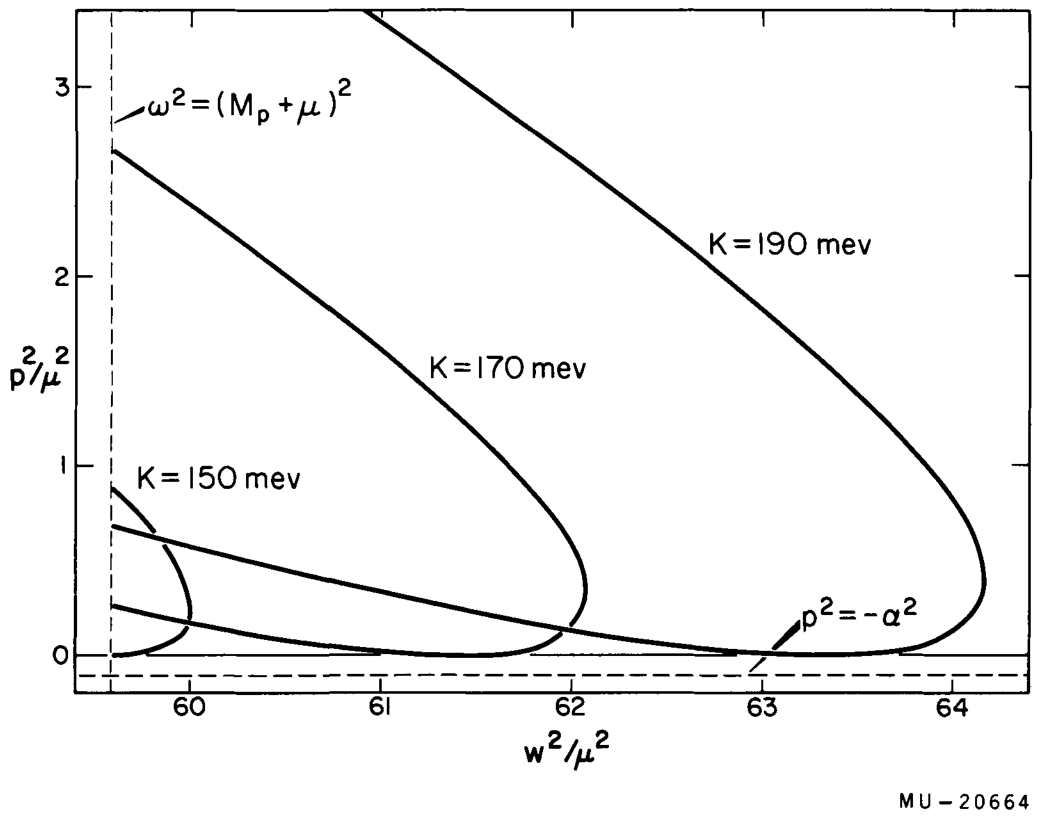

Fig. 2. Polology diagram showing kinematically allowed regions of the variables p^2 and w^2 (pion units). Experimental cross sections are to be extrapolated to $p^2 = - \alpha^2$.

II. EXPERIMENTAL TECHNIQUE

A. Introduction

In order to observe the low-energy particles from the reactions $\gamma + d \rightarrow \pi^- + 2p$ and $\gamma + d \rightarrow \pi^+ + 2n$ near threshold, the Alvarez 4-inch deuterium bubble chamber was placed in a bremsstrahlung beam from the Lawrence Radiation Laboratory electron synchrotron. A nominal peak energy E_{max} of 194 Mev was chosen for this experiment for two reasons. It eliminated much of the electron-pair background that would have been caused by the higher-energy photons. Secondly, it removed ambiguity in the analysis of some events whose measurements allowed more than one interpretation corresponding to different photon energies. In preliminary runs, it was found that chamber efficiency dropped rapidly above 180 Mev; this was unimportant since measurements close to threshold (k_T=145.83 Mev for π^-; 148.62 Mev for π^+) were of primary interest.

To remove electron background caused by the Compton effect at low photon energies, approximately one radiation length of LiH beam hardener was used. Its attenuation of the bremsstrahlung beam was largest at low photon energies, as verified by the measurements described in Sec. III.C.

B. General Description of Setup

The experimental arrangement is shown in Figs. 3, 4, and 5. A 194±2-Mev bremsstrahlung beam from the synchrotron was collimated to 1/8-in. diameter 57-in. from the internal 20-mil Pt target. A 1/2-in. collimator immediately following the first was used for additional shielding. The beam then traversed 74.5 in. of LiH beam hardener (about one radiation length) immersed in 6.43- and 7.63-kgauss sweeping fields, and passed through a tapered 3/8-in. tertiary collimator to remove "halo." The beam passed through a 5-mil brass window into a 6-ft vacuum extension. The tertiary collimator and vacuum entrance were in a 10.1-kgauss field (Fig. 6). The beam entered the 4-in. bubble chamber through a 7-mil Mylar window 7/8 in. in diameter. The approximate intensity used was 2.2×10^6 Mev per pulse before hardening, or 0.8×10^6 Mev after hardening. The beam monitor was a thick-walled Cu ionization chamber of the Cornell design.[60]

C. Synchrotron Operation

The peak energy of the synchrotron was lowered from 324 Mev to 194 Mev by reducing the voltage on the magnet capacitor bank from 14.9 to 8.76 kv. The voltage was electronically regulated to ±0.1%. The 20-μsec beam fallout duration was monitored continuously throughout the run and kept within 100 μsec of synchrotron peak field, corresponding to a variation in peak energy of at most ±0.03%. The synchrotron was pulsed in the normal manner at 6 beam pulses per second.

A total of 472 rolls of film containing an average of 400 exposures was exposed under these conditions during a 6-week run. In addition, 24 rolls were taken with the beam fallout occurring 3.875±0.010 msec before synchrotron peak field. This produced beam at a peak energy E_{max}=138±1.5 Mev, slightly below pion threshold, in order that a background subtraction could be made for two- and three-prong photoproton scatterings simulating negative-meson events.

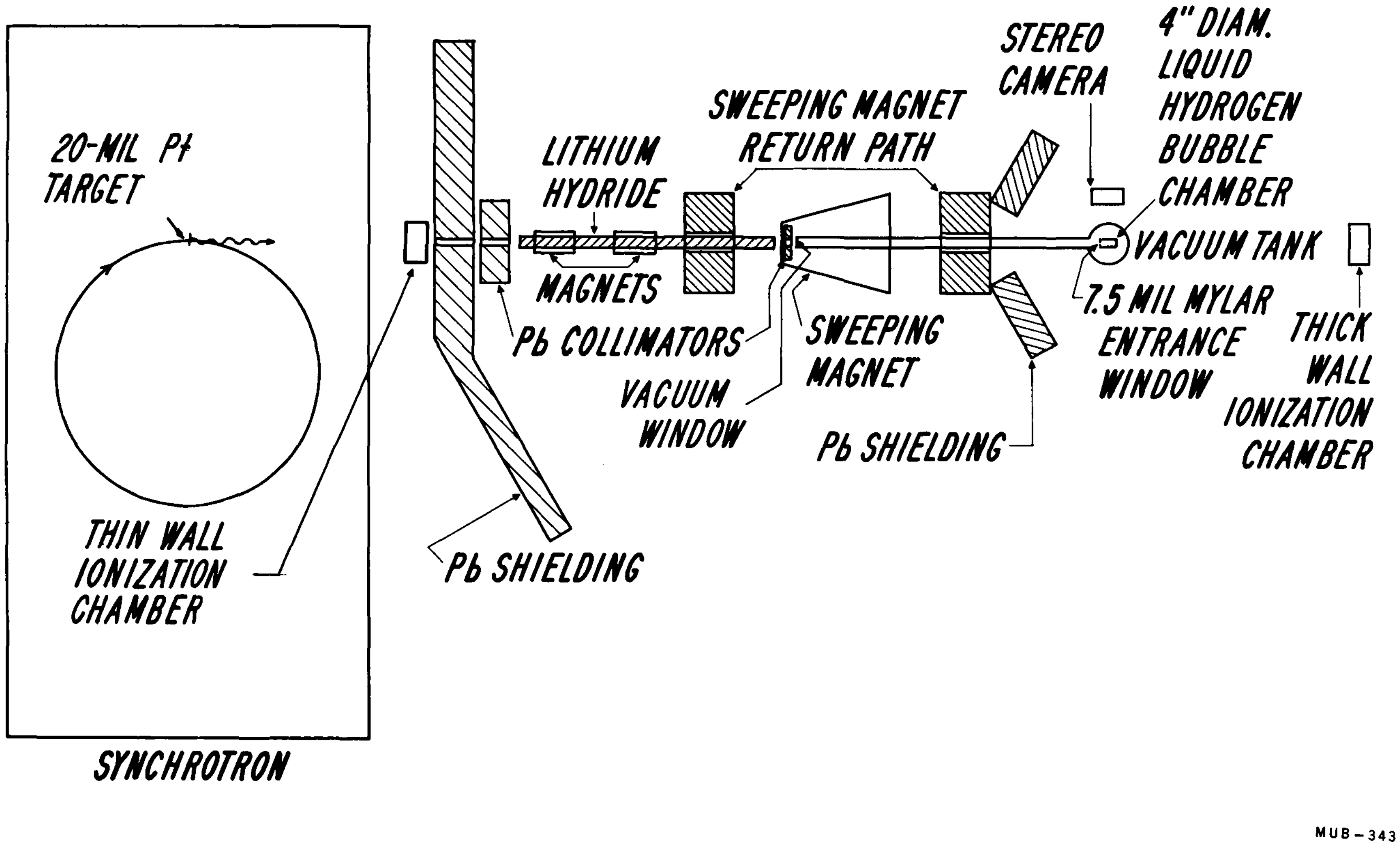

Fig. 3. Schematic diagram of setup.

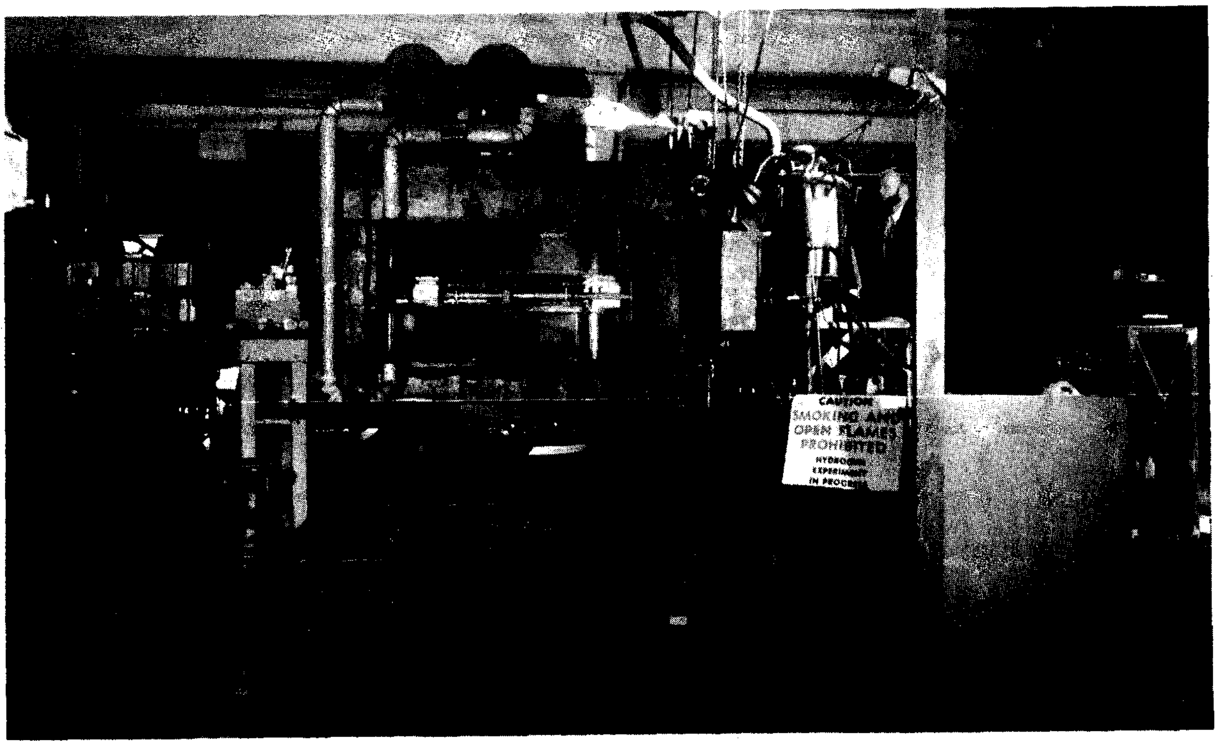

ZN-2523

Fig. 4. General view of setup. Beam leaves the synchrotron at extreme left, is collimated, passes through the LiH beam hardener (here seen disassembled on table at left), tertiary collimator, and vacuum extension. The bubble chamber is at the right.

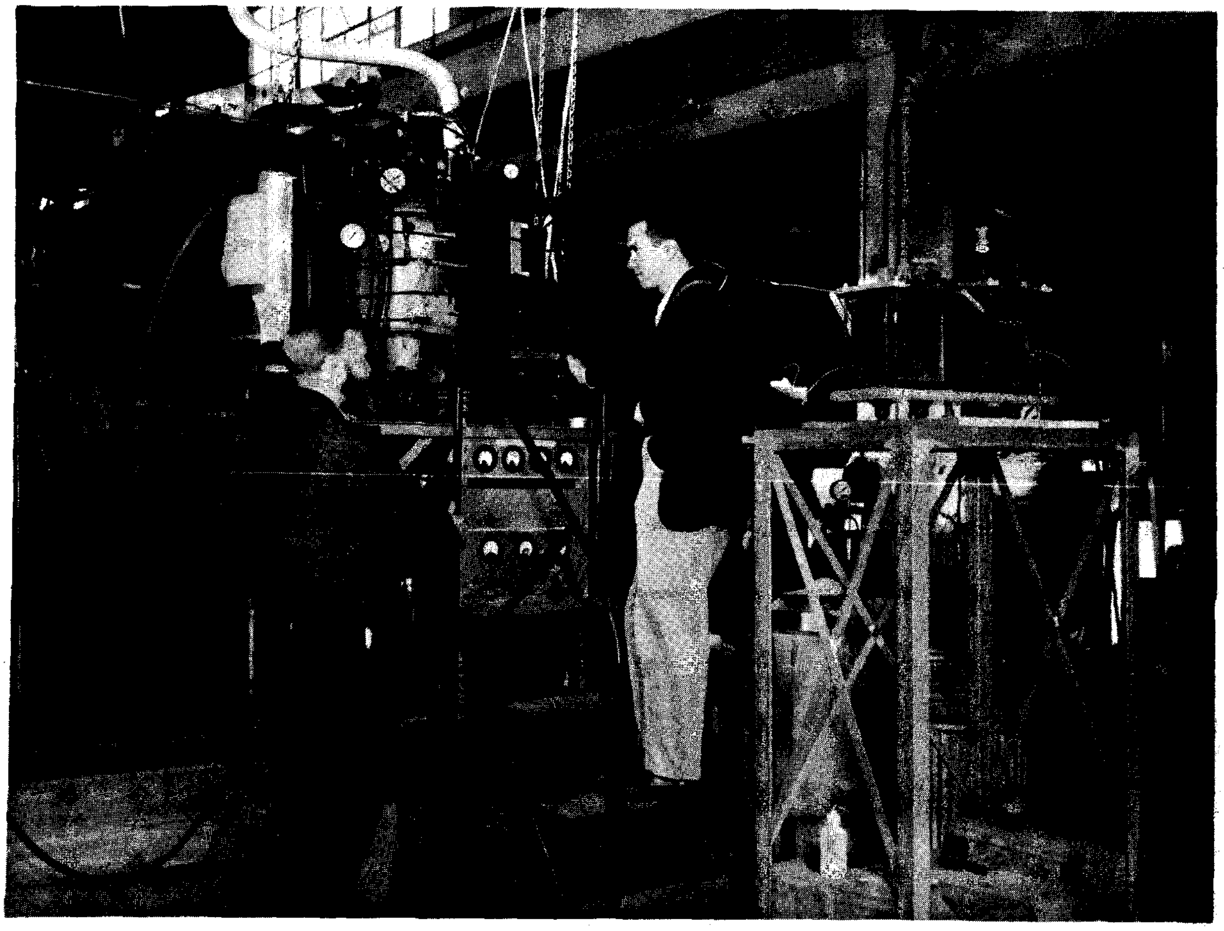

ZN-2522

Fig. 5. Bubble chamber in position.

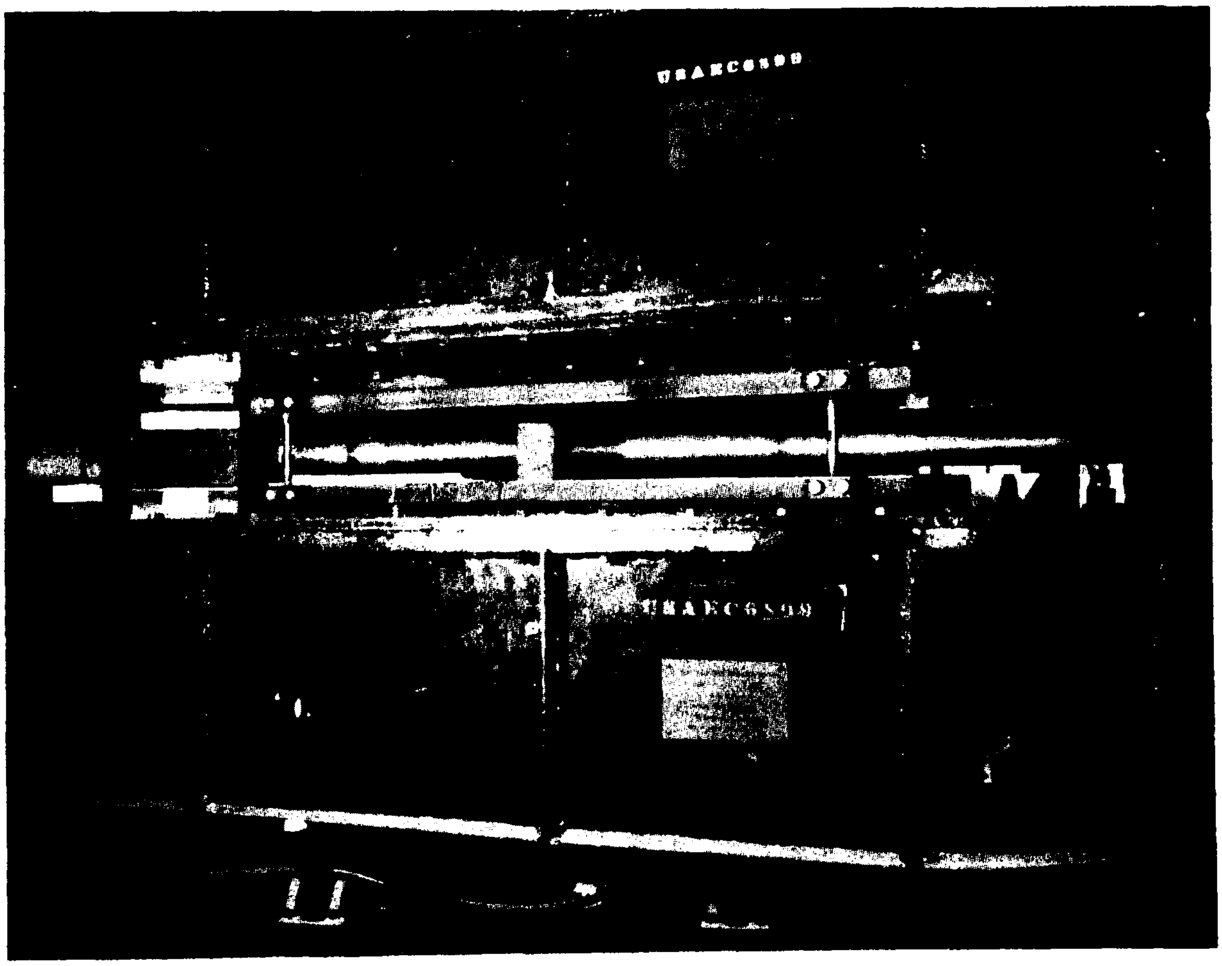

ZN-2521

Fig. 6. Detail showing beam hardener, tertiary collimator, and vacuum extension positioned in pair-spectrometer-sweep magnet.

D. Bubble Chamber

The bubble chamber used was originally built by the Alvarez group as a prototype for larger chambers.[61,62] Its nominal inside diameter is 4 inches and depth 2.154 inches. This chamber, shown in Figs. 5 and 7 through 10, has had extensive use for research[53,63-67] and perhaps has been pulsed more times (around 2×10^{6}) than any bubble chamber now in existence.

Modifications were made to adapt the chamber for use with a bremsstrahlung beam.[66] Thin entrance and exit windows, shown in Figs. 9 and 10, were used to avoid the background present from electromagnetic and photonuclear effects in the walls. Seven-mil Mylar used to form the 7/8-in.-diameter window was attached by means of a flange and lead gasket. The exit window was of 10-mil stainless steel soldered into the chamber wall. A 6-ft vacuum extension was used before the chamber to eliminate the background from this path length of air. The 5-mil brass vacuum window was placed in a 10.1-kgauss sweeping field, as shown in Figs. 4 and 6. As a result of these precautions the ratio of Compton and pair electrons entering the chamber to those produced in the chamber was only 1/3, as determined in a previous experiment employing the same experimental arrangement.[67] Tracks of photonuclear reaction products from the exit wall were virtually unseen, whereas they were a common source of background in earlier runs without the thin windows.

Deuterium taken from the bubble chamber following the run was analyzed with a mass spectrograph. About 1.04% of the atoms in the sample were found to be H^{1}. Other impurities were present only in negligible amounts.

No magnetic field was used on the chamber, since its use would have slowed the pulsing rate by a factor of 3. Field strengths readily obtainable would have been of marginal value in the identification of short tracks because the distribution in apparent curvature due to multiple Coulomb scattering would have been of the same order of magnitude as curvature due to the field.

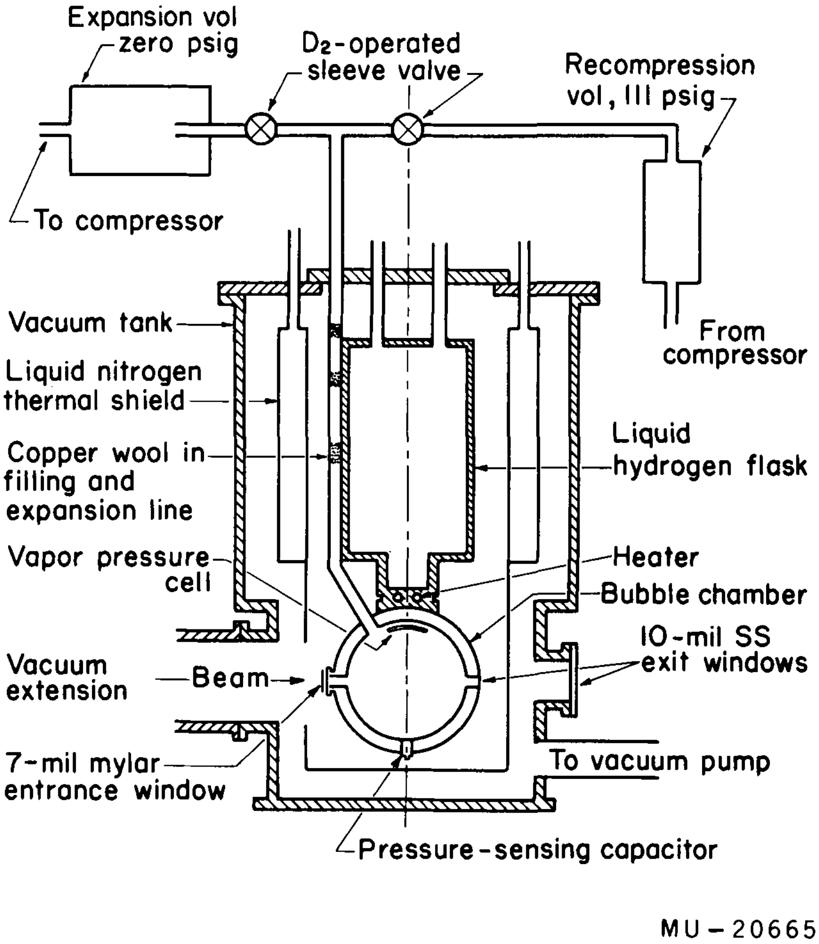

Fig. 7. Schematic of 4-inch bubble chamber.

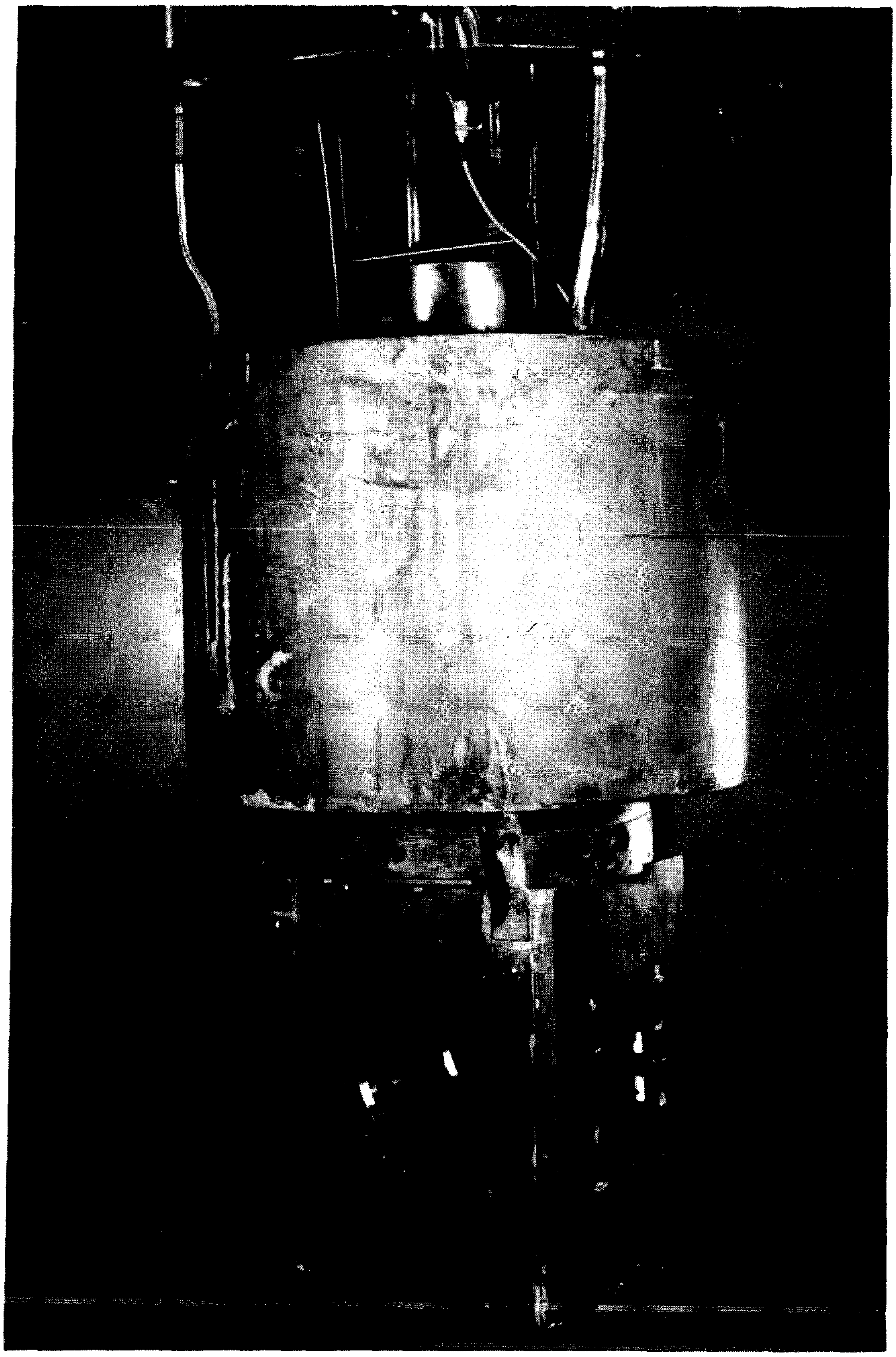

ZN-2520

Fig. 8. Bubble chamber removed from vacuum jacket, showing the liquid-nitrogen-temperature thermal shielding.

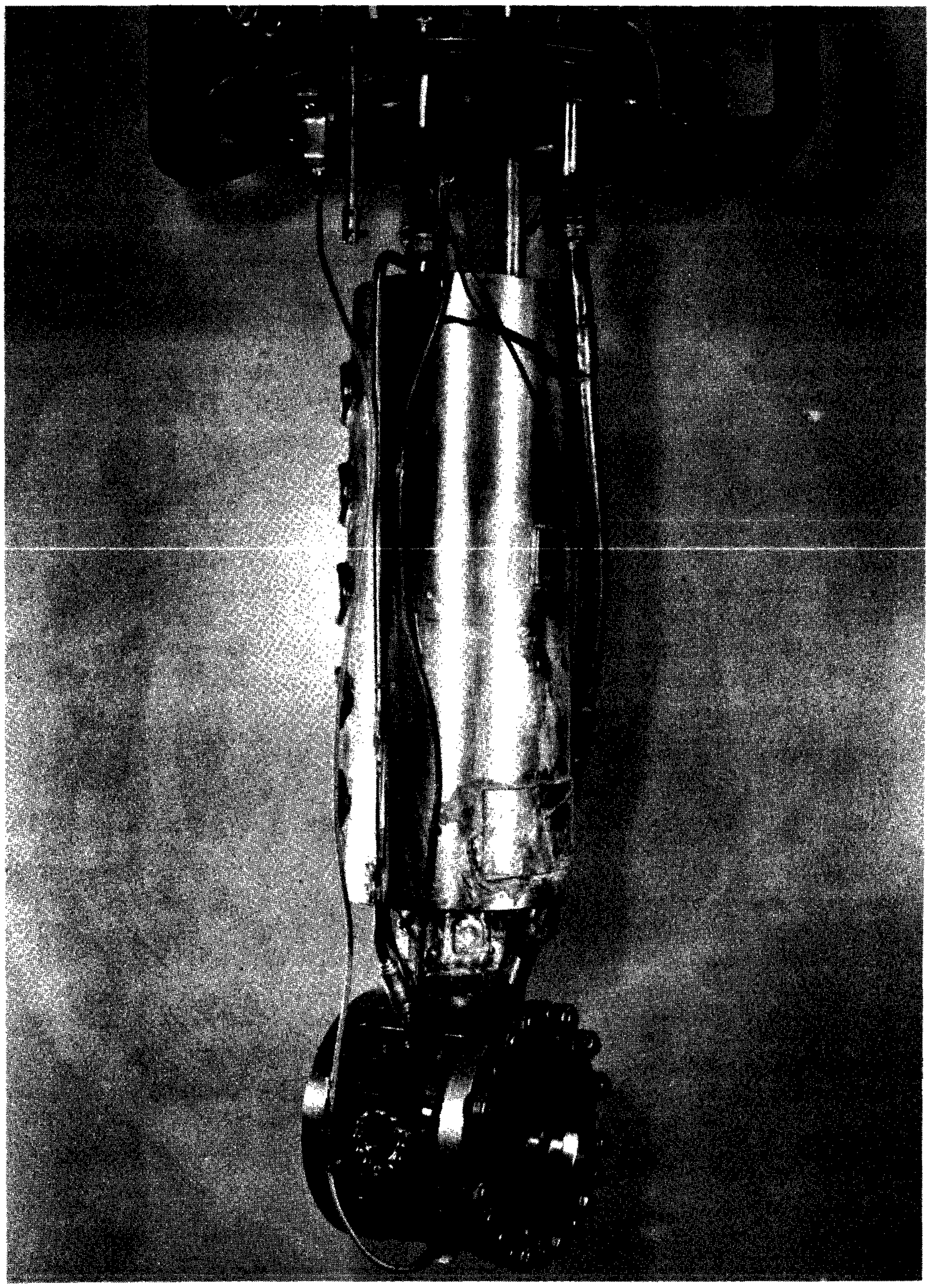

ZN-2519

Fig. 9. Bubble chamber suspended from the liquid hydrogen flask. The chamber entrance and exit windows are visible to the left and right, respectively. The coaxial cable at the left is connected to the Linlor pressure-sensing capacitor. The expansion line is visible at the right.

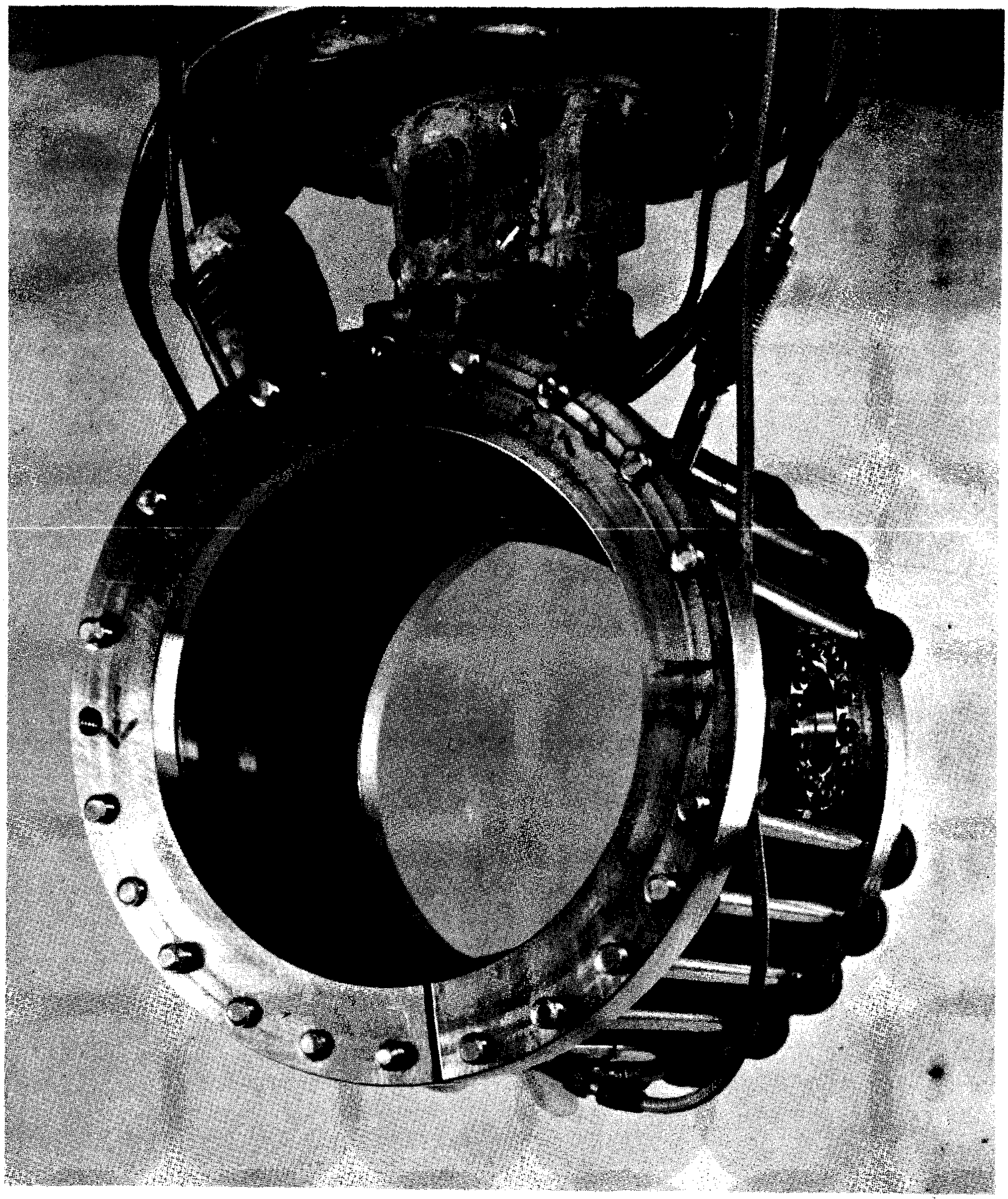

ZN-2518

Fig. 10. Detail of bubble chamber, showing the arrangement of the windows. The stainless steel chamber is supported from the liquid hydrogen flask by an OFHC copper heat leak. The vapor-pressure cell is the crescent-shaped cell at the inside top of the chamber. The small tube at the right is an intergasket window pumpout, while the one at the left is an emergency pressure release.

E. Chamber Timing

The chamber was expanded every 6 seconds. Because the sensitive time of each expansion was only a few milliseconds in duration, careful timing with respect to the synchrotron beam was required. Figure 11 shows the sequence of events for each chamber pulse.

Since the chamber expansion cycle had to begin about 15 msec before the beam arrived in the chamber, the cycle was initiated by the preceding synchrotron magnet pulse. These control pulses were provided by the synchrotron at the machine pulsing rate of six per second. One such pulse was selected every 6 seconds by a Flex-O-Pulse, a clock-operated switch. An electronic master delay of about 152 msec produced a second trigger just preceding the subsequent (used) synchrotron beam pulse. This trigger caused a deuterium-operated sleeve value to open, allowing the chamber pressure to fall from 111 psig to 59±4 psig. Shortly thereafter another pulse caused the recompression sleeve valve to allow deuterium gas at 111 psig to return to the chamber. Mechanical inertia caused the pressure dip and rise to occur about 6 msec behind their initiating pulses. The pressure dip was about 20 msec in length and was timed so that the beam passed through the chamber at the pressure minimum. About 1 msec was allowed for the bubbles to grow to 70 μ diameter before the main strobe light was flashed.

Roughly 1 second later, a light was fired to illuminate the data-readout panel. This panel contained the expansion counter and other data to be photographed with each chamber expansion. The film was advanced just following the data-light firing.

These timing pulses were continuously displayed on an oscilloscope during the run, along with the signal from a Linlor pressure gauge.[68] This gauge employs a pressure-sensing capacitor in connection with a fast pulser. A comparison between the pulses

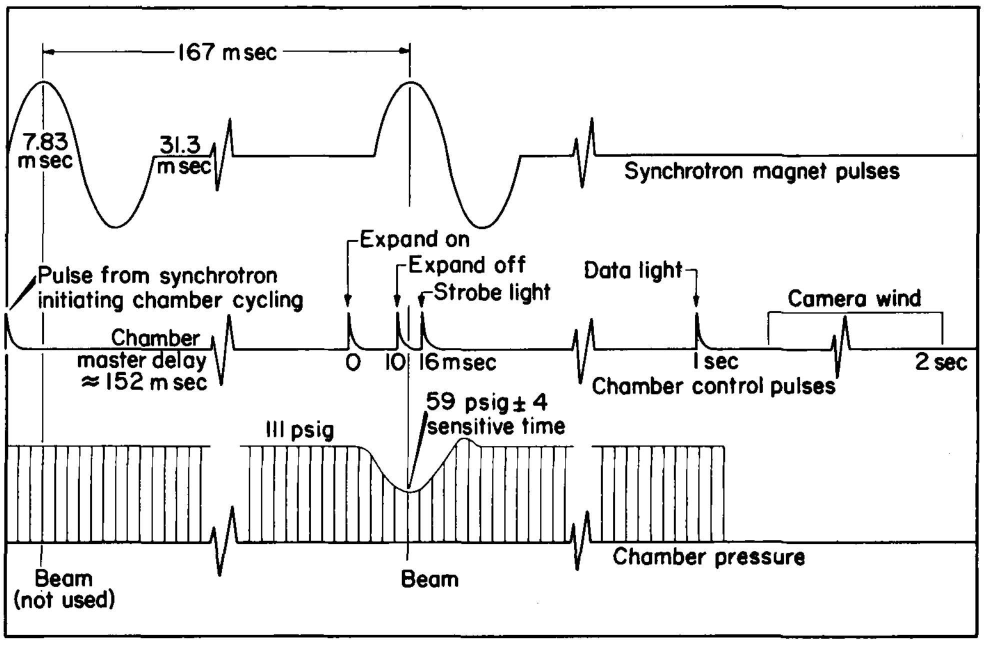

MU-20666

Fig. 11. Schematic of bubble chamber timing. The top axis represents synchrotron magnet pulses, the middle axis represents bubble chamber control pulses, and the lower one displays the chamber pressure variation as measured by a Linlor condenser pressure gauge.

reflected from the sensing capacitor and those from a fixed capacitor provided the signal schematically indicated in Fig. 11. Figure 9 shows the position of the sensing capacitor in the chamber wall.

F. Temperature Biasing of Chamber

Because of the large number of Compton and electron pair-production reactions produced within the chamber by such a beam, it was imperative to employ "temperature biasing" to reduce background caused by them. The temperature of the chamber was lowered to the point at which rapid, lightly ionizing particles left very light tracks whereas slowly moving particles left clearly distinguishable dark tracks. (It can be seen in Fig. 22 that the meson and protons stand out clearly against the background of one or two hundred light electron tracks.) A temperature of 0.1^0K higher would cause electron tracks to become dense enough to obscure all detail. A cooler chamber would make the heavy particles harder to see. Temperature was controlled during the run by a vapor-pressure-operated switch which caused either full or partial power to be applied to a heater which warmed the chamber. The chamber contained a small vapor-pressure (VP) cell charged with deuterium(Fig. 10). The pressure of this cell was transmitted to one side of a diaphragm, the other side of which held a fixed backing pressure for comparison. Differences between the backing pressure and the vapor pressure operated the heater switch.

The nominal vapor pressure was 105 psia (corresponding to 32.7° K) and our arrangement regulated VP to ± 0.5 psi or $\pm 0.025^{\circ}$K. The temperature required for good tracks sometimes drifted 1 or 2 psi over periods of a day. This was caused in part by ambient temperature fluctuations and probably by changes in chamber expansion timing and other chamber parameters.

Visual checks of chamber conditions were made every hour by means of film test strips and Polaroid Land pictures. Of the 472 rolls of film taken at E_{max} = 194 Mev, 444 were taken with good chamber conditions and were used as sources of data.

G. Chamber Optics and Photography

Direct dark-field illumination was employed in this experiment, as shown in Fig. 12. The G. E. FT-218 tube was fired at 5 watt-seconds by discharging a 10-μf capacitor charged to 1000 volts. The 1/2-in.-diameter light source was focused by a 6-in. condenser lens to a spot equidistant between the camera stereo lenses. The average radius of the illuminated region in the chamber was 4.6 cm, as determined from measurements on tracks leaving the chamber.

The data-readout panel was illuminated by a Kemlite FA-100 tube fired at 7.0 watt-seconds, and its image appeared on the film adjacent to the lower stereo picture. One-hundred-foot rolls of 35 mm Eastman Kodak unperforated Panatomic-X were used in a Recordak stereoscopic camera. The lenses were spaced 3.5 in. apart, 19 in. from the chamber center. The apertures were set at f/16 to insure adequate depth of field.

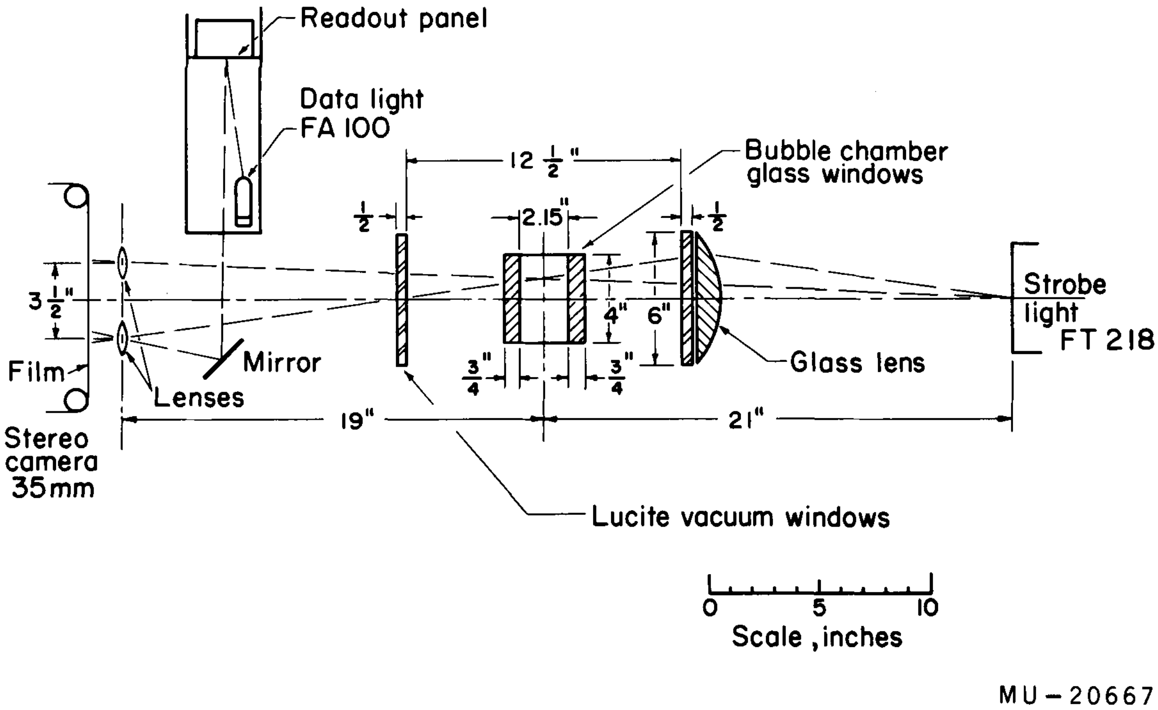

Fig. 12. Bubble chamber optics. The main light source at the right illuminates the chamber, which is viewed by a stereo camera at the left.

III. BEAM ANALYSIS

A. Beam Size and Distribution

The beam diameter was determined by a 1/8-in. collimator 57 in. from the synchrotron internal target. A second collimator, 1/2 in. in diameter, immediately following the primary collimator, and a tapered third collimator, 3/8 in. in diameter, following the LiH beam hardener were used to clean up the edges of the beam. In the chamber, the beam diameter was 0.50 ±.10 in. as verified by x-ray pictures (see Fig. 14), taken during the run, and by an analysis of the event origins.

The alignment of the chamber was facilitated by a small lead fiducial point, Fig. 13, marking the center of the Mylar entrance window. X-ray pictures exposed before the run showed the outline of the beam with the image of the fiducial marker superposed, Fig. 14. The fiducial marker could be withdrawn from the path of the beam from outside the vacuum system without disturbing the bubble chamber.

Measurements of the origins of 483 negative-meson events gave a more detailed picture of the beam profile. The event origins are projected in a plane normal to the beam direction in Fig. 15. This distribution also hints of the eccentricity seen in the x-ray picture. The beam center was taken as the average of the x and y coordinates.

By counting points in concentric rings about the center, dividing by the area, and normalizing to unity, the intensity profile shown in Fig. 16 was determined. The diameter at half intensity is 0.49 in. in agreement with the x-ray measurements. The observed eccentricity was ignored in obtaining this profile.

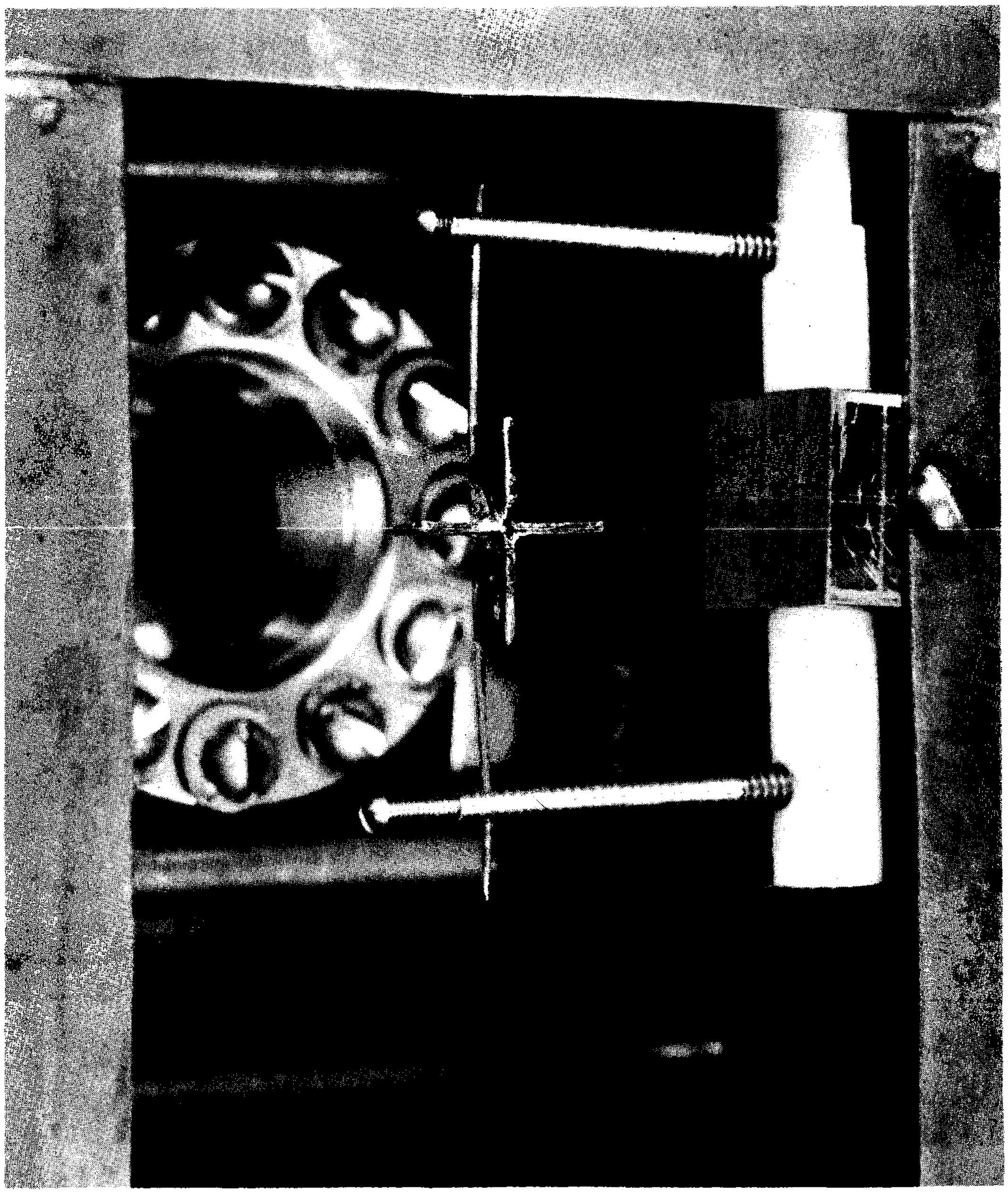

ZN-2517

Fig. 13. Detail showing the position of the lead fiducial marker used during x-ray lineup of chamber.

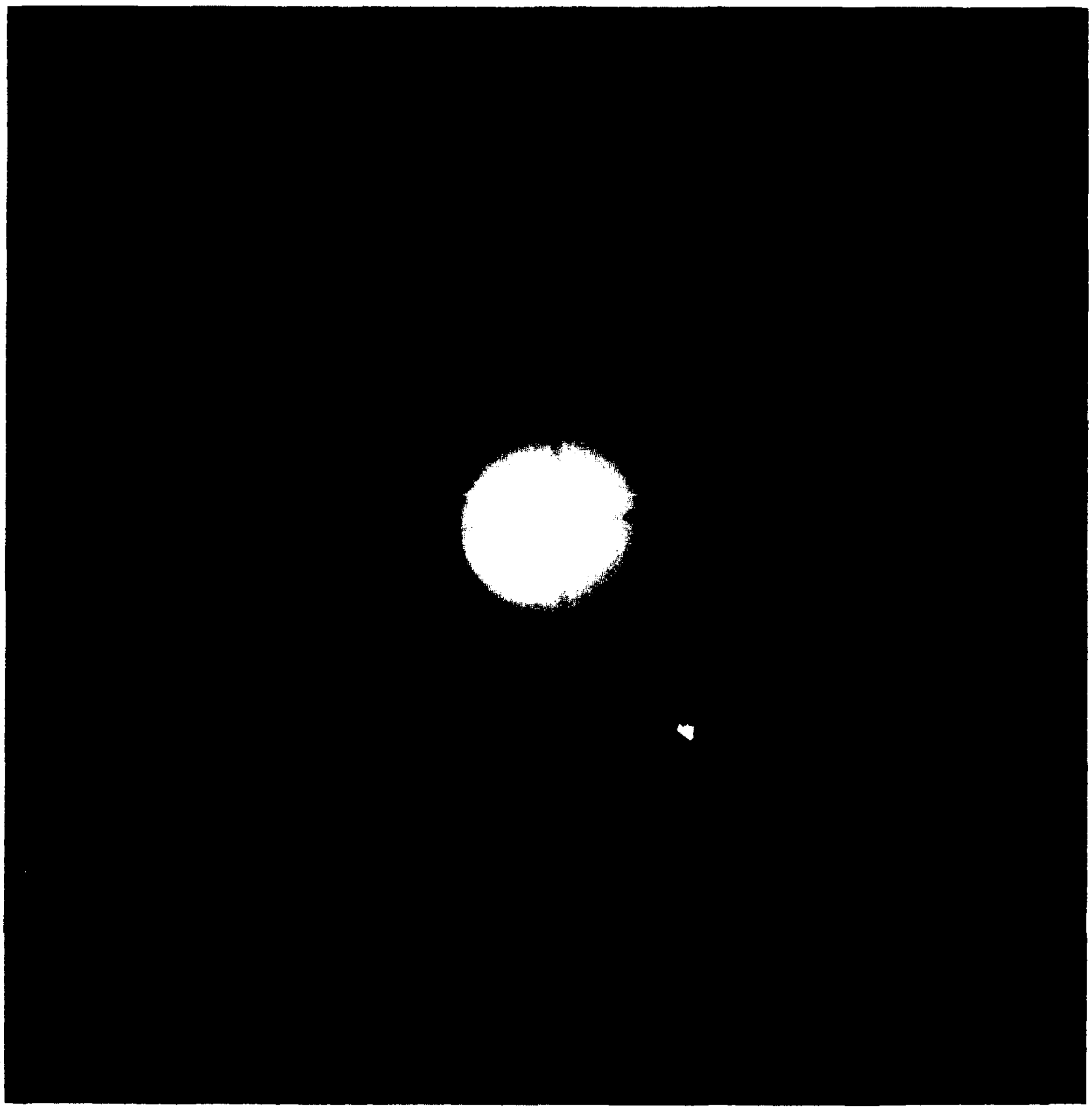

ZN-2525

Fig. 14. Contact print of beam-lineup x-ray, showing the beam size with lead fiducial image superimposed.

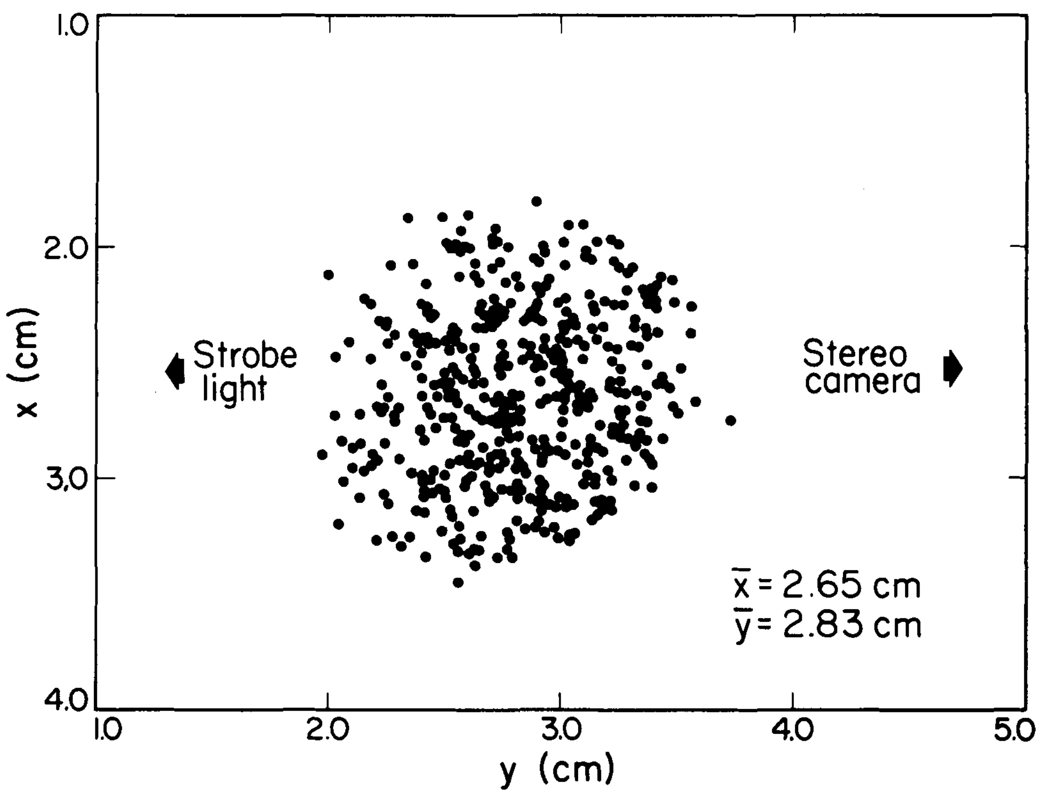

MU-20668

Fig. 15. Distribution of $\gamma + d \rightarrow \pi^- + 2p$ event vertices, used to determine the beam profile of Fig. 16.

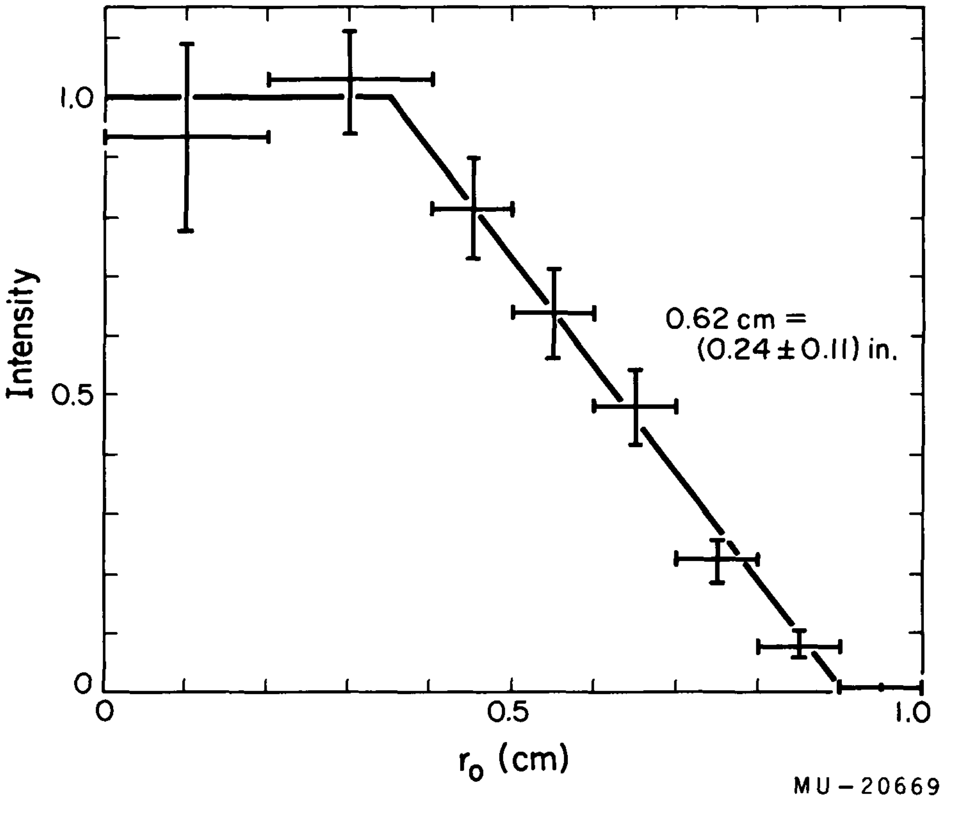

Fig. 16. Beam intensity as a function of radial distance, obtained from event distribution of Fig. 15. The trapezoidal shape was fitted by inspection.

B. Peak-Energy Measurements

To determine the exact peak energy of the synchrotron, E_{max}, the 60-deg pair spectrometer was used.[69] It was moved forward, as shown in Fig. 17, and a fourth magnet introduced to take its place as a sweep magnet. The absolute pair-spectrometer field had previously been calibrated, in terms of the voltage measured on a standard shunt, by means of a nuclear-magnetic-resonance technique. These measurements were verified at the time of the run by a 1%-of-full-scale rotating coil device. In order that a given spectrometer should current always correspond to the same magnetic field, the magnetic history of the iron was erased by saturating the magnet and then turning off the current before setting the desired current. The absolute-field measurements were taken under the same conditions. Shunt voltages were read on a potentiometer whose accuracy was 0.1%. The error in the magnetic field was assumed negligible in the reduction of the data.

Independent peak-energy cutoffs were made with both coincidence circuits, as illustrated in Fig. 18. Runs were made with a 10-mil Ta converter, background was measured with no converter present, and accidentals were counted by inserting a 2.0×10^{-8}-sec delay in one counter channel of each coincidence pair. This time roughly corresponds to one synchrotron beam rotation (2.10×10^{-8} sec). The combined corrections due to background and accidentals are also indicated on Fig. 18. The results of fitting the corrected points to straight lines are presented in Table II.

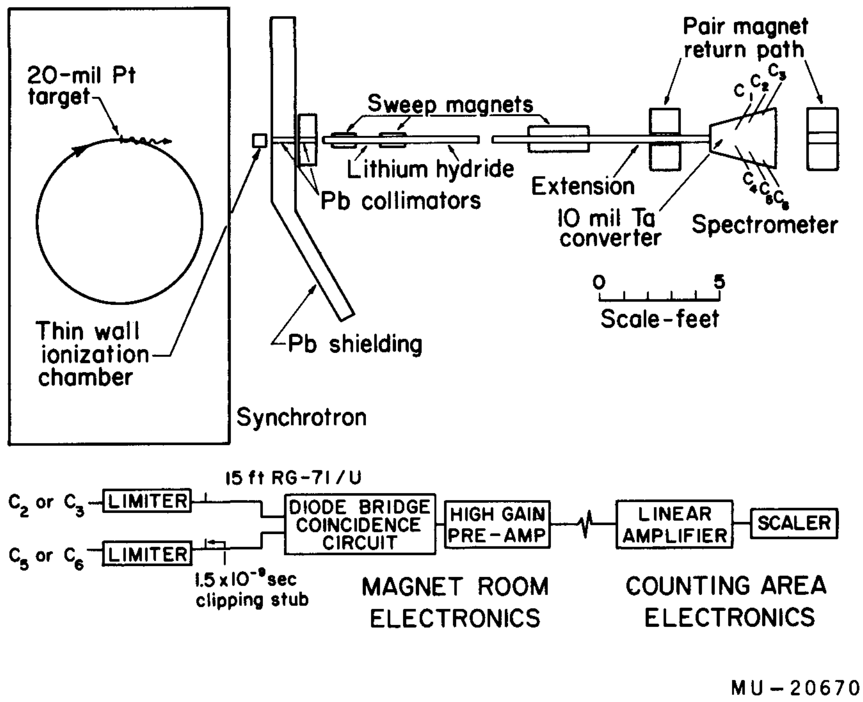

Fig. 17. Schematic of setup during pair-spectrometer measurements. The setup resembles that of Fig. 3 except that the pair-spectrometer magnet was moved forward, replacing the bubble chamber, and a fourth sweep magnet introduced. The LiH was removed for peak-energy measurements.

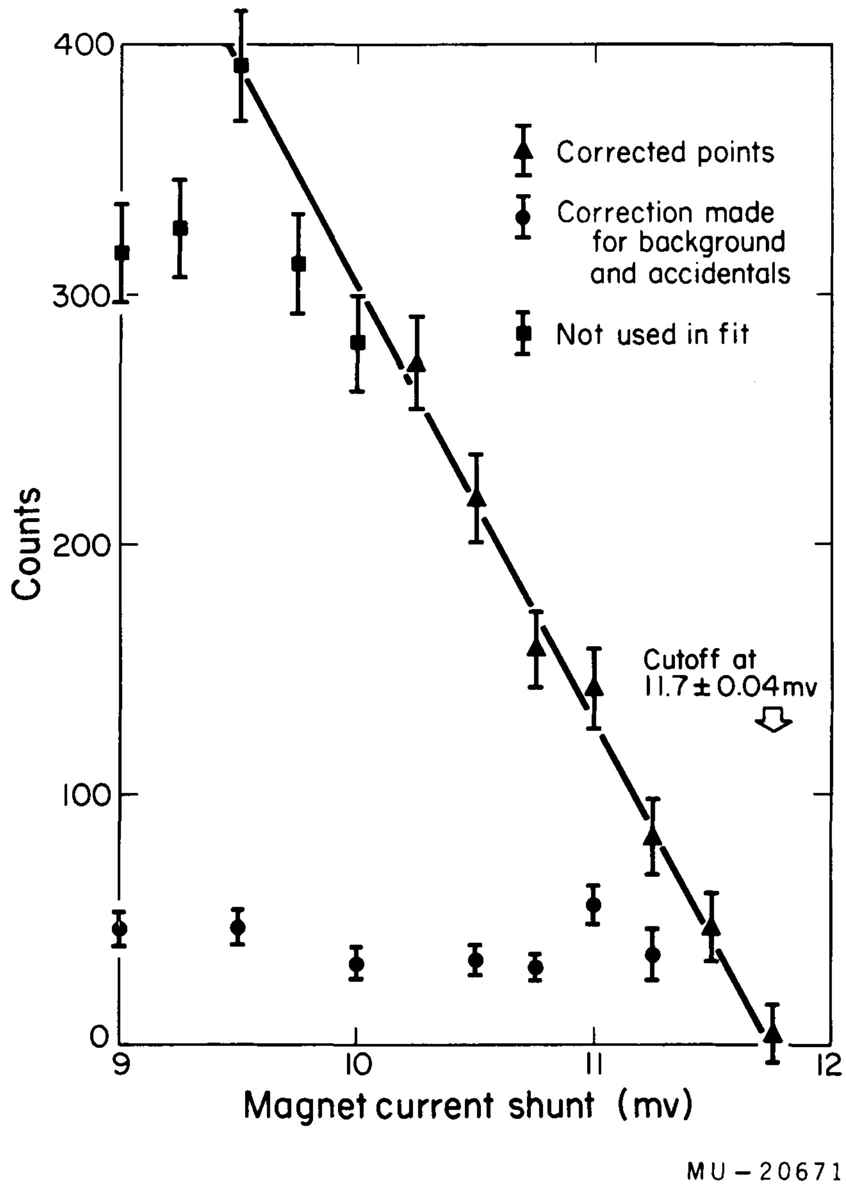

Fig. 18. Pair-spectrometer peak-energy cutoff for Channel (2 + 5). Seven experimental points, corrected for background and accidentals, were used in making the straight-line fit. The 11.76±0.04-mv cutoff point corresponds to a peak synchrotron energy of 193.7±0.1 Mev.

Table II

Least-squares extrapolations of the peak-energy cutoffs

Channel	Number of points used	χ^2	Cutoff point shunt voltage (mv)	Magnetic field (kgauss)	Sum of orbit radii (cm)	Calculated peak energy (Mev)
(2 + 5)	7	2.40	11.76±0.04	6.29±0.02	102.7±0.1	193.7±0.6
(3 + 6)	3	5.30	8.71±0.08	4.69±0.04	140.0±0.1	196.9±2.0

The weighted average of these extrapolations gives 194.0±0.6 Mev. An error of 1% is allowed for reproducing the meter reading on the synchrotron magnet power supply, giving 194±2 Mev. The photon energy at each cutoff was calculated from the formula

$$k = 0.2998\, H_{\text{kgauss}} \quad \Sigma\, \rho_{\text{cm}} \,. \tag{8}$$

For our 60-deg spectrometer, the sum of the radii was taken to be simply the sum of the direct distances from the center of the converter to the center of each counter, as shown in Fig. 19. The excellent fits of the points to straight lines justifies the use of the centers of the counters to determine the effective radii.

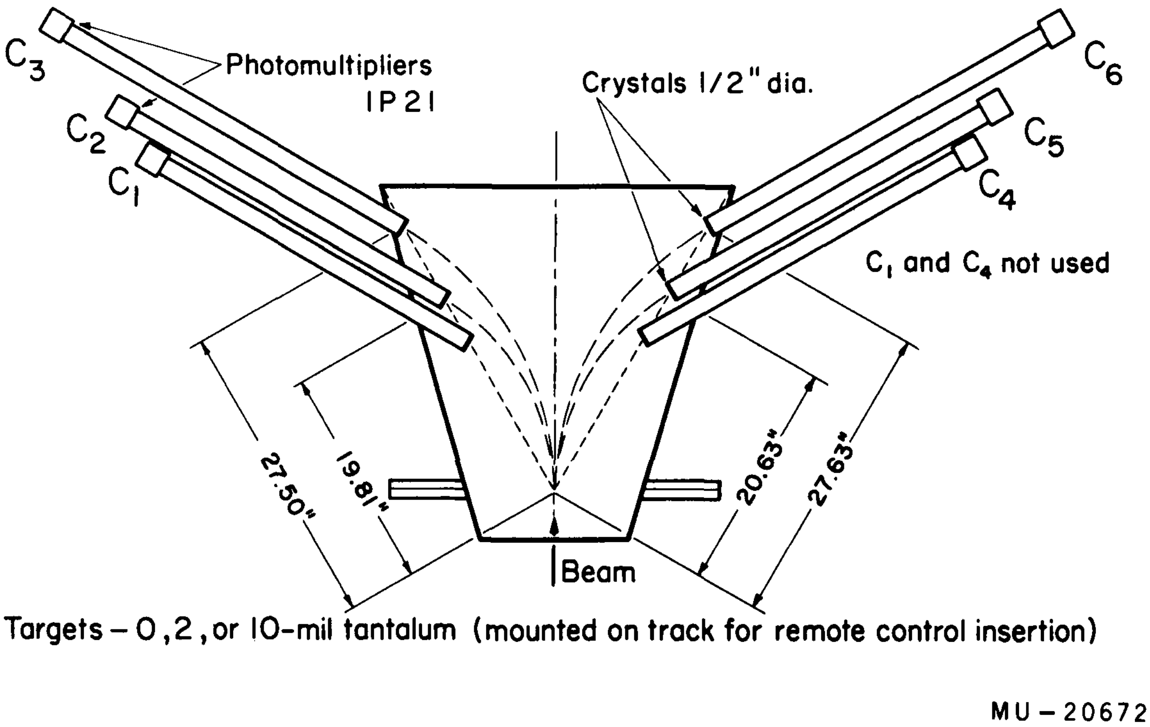

Fig. 19. Geometry of 60-deg pair-spectrometer pole tips, showing positions of the counters. Electron pairs produced in the thin Ta targets were detected in coincidence by counter pairs (2 + 5) and (3 + 6).

C. LiH Transmission Measurements

Low-Z material can be used as beam hardener because the Compton cross section is large compared with the pair-production cross section. At the photon energies used here, the ratio of these cross sections is approximately

$$\phi_C : \phi_P \approx Z \frac{8}{3} \pi r_0^2 : Z(Z+1) r_0^2/137 \approx 1000:(Z+1),$$

where r_0 is the classical electron radius. Since the Compton effect is largest at zero photon energy (the Thomson cross section) and decreases with energy, the lowest-energy photons will be predominantly absorbed. The logarithmic rise in the pair cross section with energy somewhat vitiates this, but the over-all effect is still in the desired direction.

The 74.5-inch LiH beam hardener was made up of six 2-in.-diameter Lucite tubes filled with powdered LiH and sealed on the ends with 1/8-in. Lucite disks. It was determined that the material in the tubes presented a surface density of 99.48 g/cm^2 to the beam. The transmission by the tubes was measured as a function of photon energy but using the pair spectrometer and counter arrangement just described, but with a peak bremsstrahlung energy E_{max} = 324 Mev. The experimental arrangement is shown in Fig. 17.

Results are presented in Fig. 20. Runs were made with a 10-mil or 2-mil Ta converter alternately in and out of the beam, and with the LiH inserted and removed. Accidentals were again counted with a 2.0×10^{-8}-sec delay in one counter channel of each coincidence pair. Runs were kept to a length of 5 or 10 minutes to avoid electronics drift and synchrotron parameter changes. No run was longer than 15 minutes. The entire cycle was repeated several times at each photon energy.

The transmission at a given pair-spectrometer magnet setting was calculated by the formula

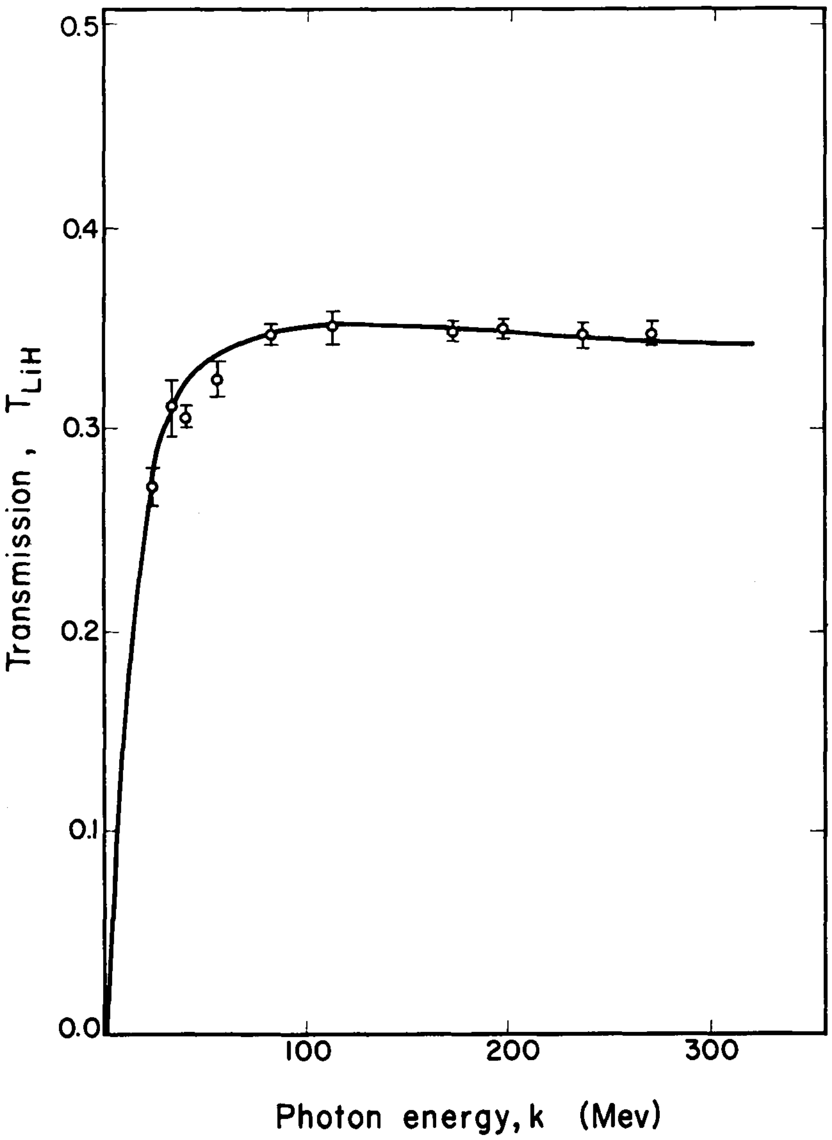

MU-18566

Fig. 20. Transmission measurements for the LiH beam hardener. The experimental points shown were fitted to a combination of the transmissions of elements Li, H, C, and 0, to include the effect of the absorbed H_2O and the Lucite ends.

$$T = \frac{\left[\left(\frac{R}{M} - \frac{A}{M}\right)_{\text{Ta in}} - \left(\frac{R}{M} - \frac{A}{M}\right)_{\text{Ta out}}\right]_{\text{LiH in}}}{\left[\left(\frac{R}{M} - \frac{A}{M}\right)_{\text{Ta in}} - \left(\frac{R}{M} - \frac{A}{M}\right)_{\text{Ta out}}\right]_{\text{LiH out}}}, \tag{9}$$

where R and A refer respectively to real and accidental counts, and M to the accompanying beam monitor reading. The thin-walled ionization chamber was used as a beam monitor, since absolute monitoring was not required, and the machine intensity was kept low to avoid any possibility of jamming. The photon energies were again calculated by means of Eq. (8).

The smooth curve through the data is derived from a linear combination of the theoretical attenuations of Lucite ($H_8C_5O_2$), LiH, and H_2O. The amount of Lucite in the beam hardener ends was easily measured and found to be 2.27 g/cm^2, and its attenuation curve was obtained in a straightforward way. A linear combination of the curves for LiH and H_2O was combined with this by means of a least-squares fit to the experimental points. It was determined in this way that LiH constituted 0.748±0.006 by weight of the material in the tubes, the remainder being H_2O. The attenuations due to the elements H, Li, C, and O used in this fit were obtained up to 100 Mev from Grodstein's tabulations.[70] Above 100 Mev, they were calculated directly from the Klein-Nishina formula[71] and the Bethe-Heitler pair-production cross section,[72] taking partial screening and Coulomb corrections[73] into account. The cross section assumed for electron pair production in the fields of orbital electrons was that estimated by Joseph and Rohrlich.[73]

Correlating the data by means of such a least-squares fit has the effect of increasing our knowledge of the transmission at any given point. The adjusted error in the transmission in the region 140 to 200 Mev is 0.5%, whereas the errors on the experimental points are around 1.5% each.

Measurements at 41.6 and 56.1 Mev were repeated with the first and second sweep magnets off. This had no effect within statistics, on the observed attenuation. The implication is that multiple Coulomb scattering is so effective in removing electrons produced in the beam hardener before they can reradiate in the beam direction that the sweeping fields make a negligible contribution to their removal.

In addition to the measurements made by using a 324-Mev bremsstrahlung beam, transmission measurements at 40.3 and 55.4 Mev were repeated with a lowered synchrotron energy E_{max} of 194 Mev. This was done to determine whether pair electrons produced within the beam hardener by high-energy photons would reradiate in the forward direction with sufficient probability to noticeably alter the spectrum at lower photon energies. No such effect was seen within statistics.

D. Spectrum

It was decided that the bremsstrahlung spectrum derived by Schiff[74] would be appropriate for our 20-mil Pt internal target. Spectrum tabulations for 200 Mev (screening constant = 111) published by Penfold and Leiss[75] were adapted for our use by multiplying the abscissa of each point by 0.96. This spectrum is shown in Fig. 21. The hardened spectrum on the same graph was obtained by multiplying by the transmissions given on Fig. 20.

E. Total Effective Flux

A thick-walled Cu ionization chamber of the Cornell design was used as beam monitor. The charge was collected on a 134.7±1.3-μμf low-leakage (Fast Corp.) condenser in connection with a 100% feedback dc electrometer and a Leeds and Northrup Speedomax recorder set at 10 volts full scale. The condenser was calibrated by comparing its charging rate with that of a standard 0.001-μf capacitor.

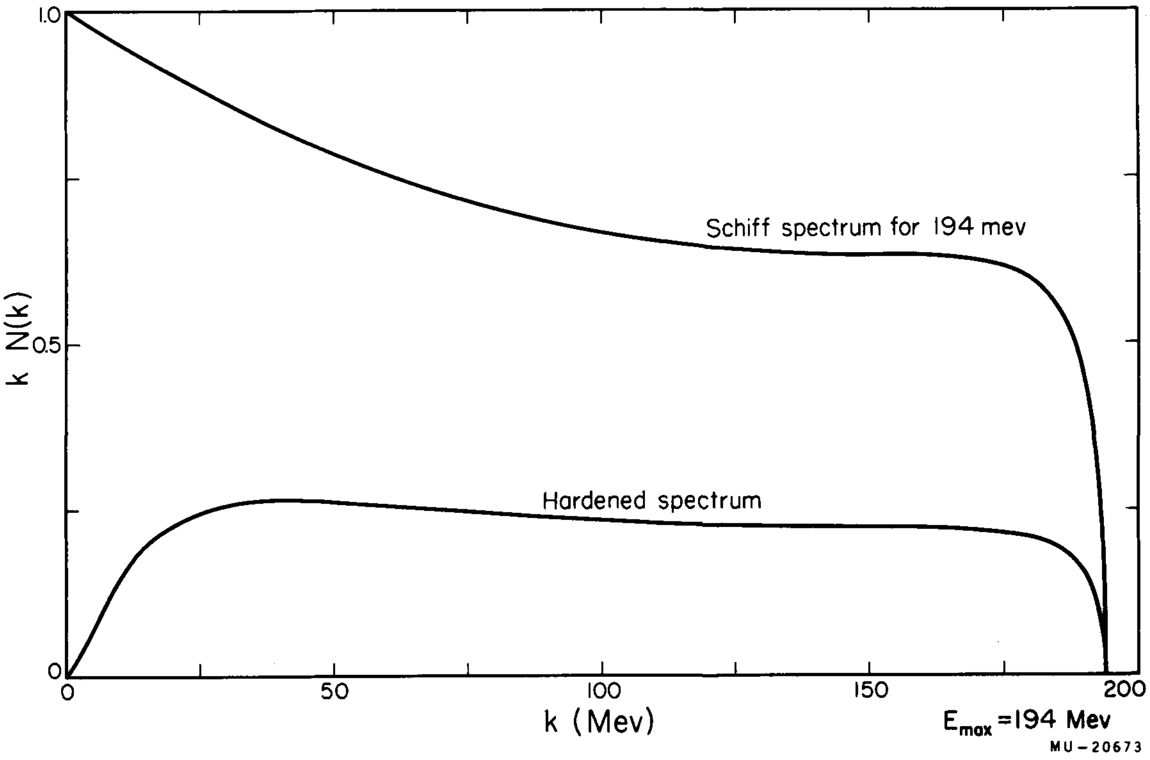

Fig. 21. Theoretical Schiff bremsstrahlung spectrum for 194 Mev, before and after the LiH beam hardener. The lower curve was obtained by multiplying the Schiff spectrum by the transmissions of Fig. 20.

In computing the effective beam flux per roll of film, it was assumed that the average flux per synchrotron pulse (at 6 per second) was the same as the average per bubble chamber expansion (one per 6 seconds). During the run, the Cornell integrated charge and the running time per roll were recorded. The average running time was 40 minutes for a roll of 400 exposures. The effective flux for each roll was calculated by the formula

$$\left\{\begin{array}{l}\text{Effective}\\ \text{hardened}\\ \mu\text{ coul}\\ \text{for roll}\end{array}\right\} = \left\{\begin{array}{l}\text{number of}\\ \text{usable frames}\\ \text{in roll}\end{array}\right\} \times \left\{\frac{\text{Cornell } \mu \text{ coul integrated}}{\begin{array}{l}\text{Total number of}\\ \text{synchrotron beam pulses}\\ \text{during exposure of roll}\end{array}}\right\}. \tag{10}$$

Of course, this refers to a hardened beam, so that this number could not be directly applied in computing numbers of photons in the bubble chamber.

Five times during the run, the Cornell chamber was calibrated against itself with an without the beam hardener. The thin-walled ionization chamber was used as an intermediate monitor. It was found that one μcoul integrated by the Cornell chamber with the hardener in place implied that 3.325 ± 0.046 μcoul of unhardened beam was incident on the LiH. The error was obtained from the standard deviation (± 0.11) of the five determinations, and probably arose from inaccurate repositioning of the LiH.

Thus, the numbers obtained from Eq. (10) had to be multiplied by 3.325 ± 0.046 and then by $(3.95 \pm 0.16) \times 10^{12}$ Mev/μcoul, the ionization-chamber constant[76, 77] for 194 Mev corrected for ambient temperature and pressure.

For the 444 usable rolls, a total of 0.03406 ± 0.00034 effective μcoul was collected with the beam hardener in place. The 1% error arises from the calibration of the integrating condenser. After multiplying by the factors just mentioned, we obtained $(0.373 \pm 0.017) \times 10^{12}$ Mev integrated flux incident on the beam hardener.

By taking ratios of the areas of the small energy bins to the total area under the primary spectrum of Fig. 21 and dividing by the central bin energy, we obtained the relative numbers of photons incident on the beam hardener. Multiplying by $(0.373 \pm 0.017) \times 10^{12}$ Mev times the transmission (Fig. 20) at each energy gave the absolute numbers of the photons passing through the bubble chamber. The numbers are tabulated in Table III.

Errors in these numbers arise from the following sources:

Ionization-chamber constant	4%
Ionization-chamber filling	0.8%
Integrating condenser calibration	1.0%
Beam-hardener positioning	1.4%
Beam-hardener attenuation	0.5%

A 4% error is assigned to the ionization-chamber constant to allow for the discrepancy between the compilations by Loeffler et al.[76] and Dewire,[77] as well as their stated absolute errors. The combined monitoring error is assumed to be 4.5% up to 180 Mev.

Table III

Effective numbers of photons incident on the bubble chamber
Flux incident on beam hardener = $(0.373 \pm 0.017) \times 10^{12}$ Mev

Photon energy interval (Mev)	$\frac{a_i}{Ak}$ from Schiff spectrum (number $\times 10^{-5}$)	Beam-hardener transmission	Number of photons (number$\times 10^7$)
145.83 to 147.5	5.223	0.351	0.6837
147.5 to 150	7.710	0.351	1.009
150 to 152.5	7.586	0.351	0.9932
152.5 to 155	7.457	0.351	0.9761
155 to 157.5	7.334	0.350	0.9575
157.5 to 160	7.214	0.350	0.9418
160 to 162.5	7.092	0.350	0.9258
162.5 to 165	6.963	0.350	0.9090
165 to 167.5	6.849	0.3495	0.8930
167.5 to 170	6.731	0.3495	0.8773
170 to 172.5	6.599	0.3495	0.8601
172.5 to 175.	6.453	0.395	0.8411
175 to 177.5	6.288	0.349	0.8187
177.5 to 180	6.098	0.349	0.7937
180 to 182.5	5.887	0.349	0.7665
182.5 to 185	5.618	0.349	0.7315
185 to 187.5	5.252	0.348	0.6818
187.5 to 190	4.695	0.348	0.6095
190 to 192.5	3.658	0.348	0.4748
192.5 to 194	1.278	0.348	0.1660

IV. ANALYSIS OF FILM

A. Introduction

The main problem in the data analysis was the separation of pion events from a background of photonuclear-product scatterings which could simulate the desired meson events. Since no magnetic field was used on the chamber, particles could not be identified by range-momentum relationships. Ionization measurements were only of qualitative value because of slight but continual fluctuations in bubble-formation conditions. Therefore, kinematical considerations (for π^- events) or decay modes (for π^+ events) were used for identification and analysis of the events.

The categories of events involving particles heavier than electrons are

$$\gamma + d \to \pi^- + 2p \,, \tag{1}$$

$$\gamma + d \to \pi^+ + 2n \tag{2}$$

$$\qquad\qquad \lfloor\!\!\to \mu^+ + \nu$$

$$\qquad\qquad\qquad\quad \lfloor\!\!\to e^+ + \nu + \bar{\nu} \,,$$

$$\begin{aligned} \gamma + d &\to \pi^0 + d \\ &\to \pi^0 + n + p \,, \end{aligned} \tag{3}$$

$$\gamma + d \to n + p \,, \tag{4}$$

$$\gamma + d \to \gamma + d \,. \tag{5}$$

Reaction (1) (Fig. 22), with Reaction (2), is of primary interest in this experiment. There are three charged particles in the final state, but not all of them may give visible tracks if either too short or too lightly ionizing. This reaction may appear as a three-, two-, or one-prong event. All such events with three prongs are fully analyzable (Sec. V. A), as also are those with two prongs if both prongs end in the chamber. No other track configurations are analyzable.

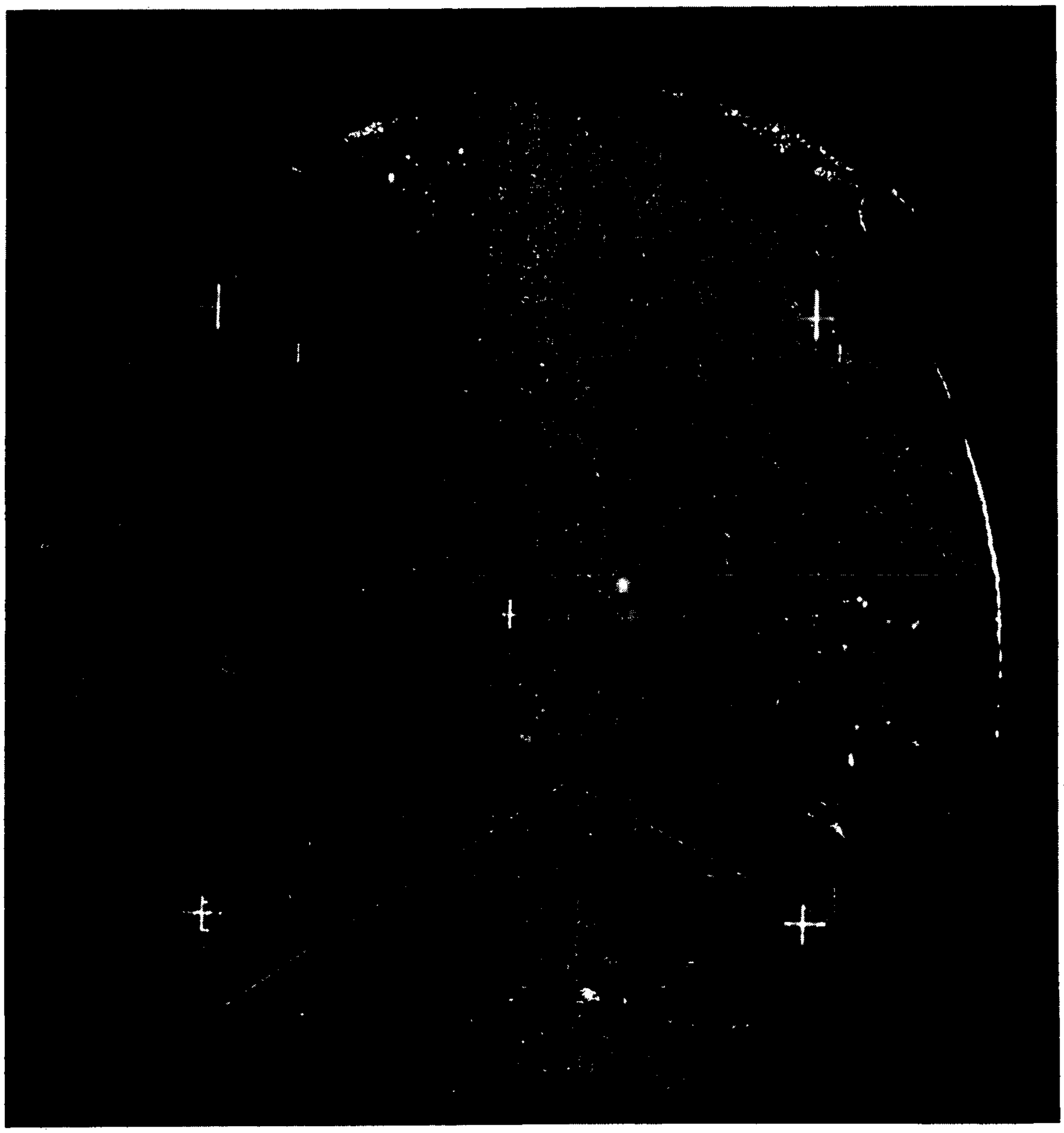

ZN-2532

Fig. 22. An example of the reaction $\gamma + d \rightarrow \pi^- + 2p$ in the 4-inch deuterium bubble chamber. Beam enters at top of picture.

Reaction (2) is also of major importance (Fig. 23). Since there is no way to identify a single track per se, the decay of the π^+ into a μ^+ with a well-defined range (1.004 ± 0.053 cm in bubble chamber deuterium, Sec. IV. F) is used as the identifying feature. Thus, only stopping positive pions which decayed into stopping muons were used. The difference in ionization between the stopping π^+ and the outgoing μ^+ also was a factor in identifying positive-meson events. In 26% of the cases, identification was made certain by a "visible" positron from the μ^+ decay.

Reaction (3) should occur less frequently than Reaction (1) or (2), since neutral-photopion production near threshold on protons is much lower[78] than positive-pion production, and neutral-photopion production occurs on protons and neutrons with about equal probability, as experimentally verified at higher photon energies.[79] Only the outgoing p or d track is visible in Reaction (3), and no sure identification of the event type is possible.

Photodisintegration of the deuteron (Fig. 23), Reaction (4), occurs very frequently, since it has a comparatively large cross section in the low-energy half of the spectrum,[80] where more photons are present. Interactions caused by photons of energy 20 to 60 Mev generally produce protons with visible tracks which stop in the chamber. These data will subsequently be analyzed. Photodisintegrations contribute the most troublesome form of background when the outgoing proton scatters on a deuteron and resembles a two- or three-prong event of Type (1).

Reaction (5), the deuteron Compton effect, rarely occurs, since its cross section is of the order

$$\frac{8}{3}\pi\left(\frac{e^2}{M_D C^2}\right)^2 \approx 5 \cdot 10^{-32}\ \text{cm}^2 .$$

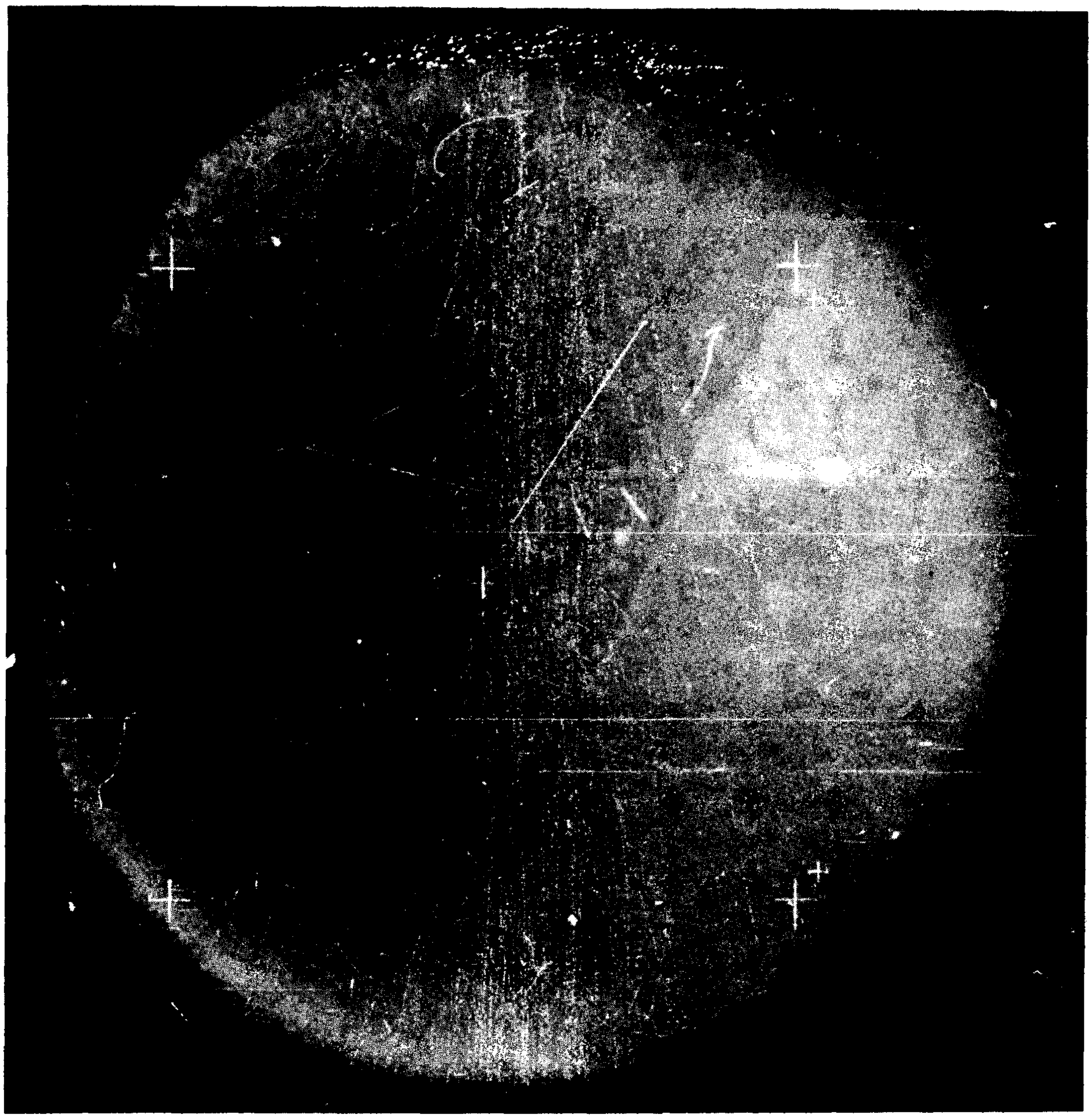

ZN-2524

Fig. 23. An example of the reaction sequence
$\gamma + d \rightarrow \pi^+ = 2n, \ \pi^+ \rightarrow \mu^+ + \nu \ , \ \mu^+ \rightarrow e^+ + \nu + \overline{\nu}$,
seen in the 4-inch deuterium bubble chamber. Positive pions are normally identified by their muon decay. In 26% of the cases, the positron track is also visible. A photoproton track is also visible here. Beam enters at top of picture.

B. Scanning Procedure

A stereoscopic viewer (Fig. 24) was used to read the film. Two complete scannings of each roll were made. Standard scanning sheets were used on which the roll and frame number, number of prongs, and number of leaving tracks were entered, along with a diagram of each event. All two- and three-prong track configurations that could reasonably be negative or positive production events were listed. Events with origins obviously outside the beam or with tracks obviously going the wrong direction by ionization were omitted. As the scanners were instructed to be conservative in omitting apparent nonmeson events, only 28% of the tabulated events were later determined to be analyzable meson events.

Twelve percent of the analyzable negative mesons and 4% of the positive mesons were found on the rescan, giving over-all human efficiencies of 98.4 and 99.8%, respectively. A typical full day of work for one scanner was eight rolls of film.

After the rolls had been scanned, measured, and kinematically analyzed, each event was re-examined by a team of two physicists. One perused the event in the viewer while the other looked in the kinematic analysis for an interpretation of the event agreeable to both. This could be done at the rate of five or six rolls an hour.

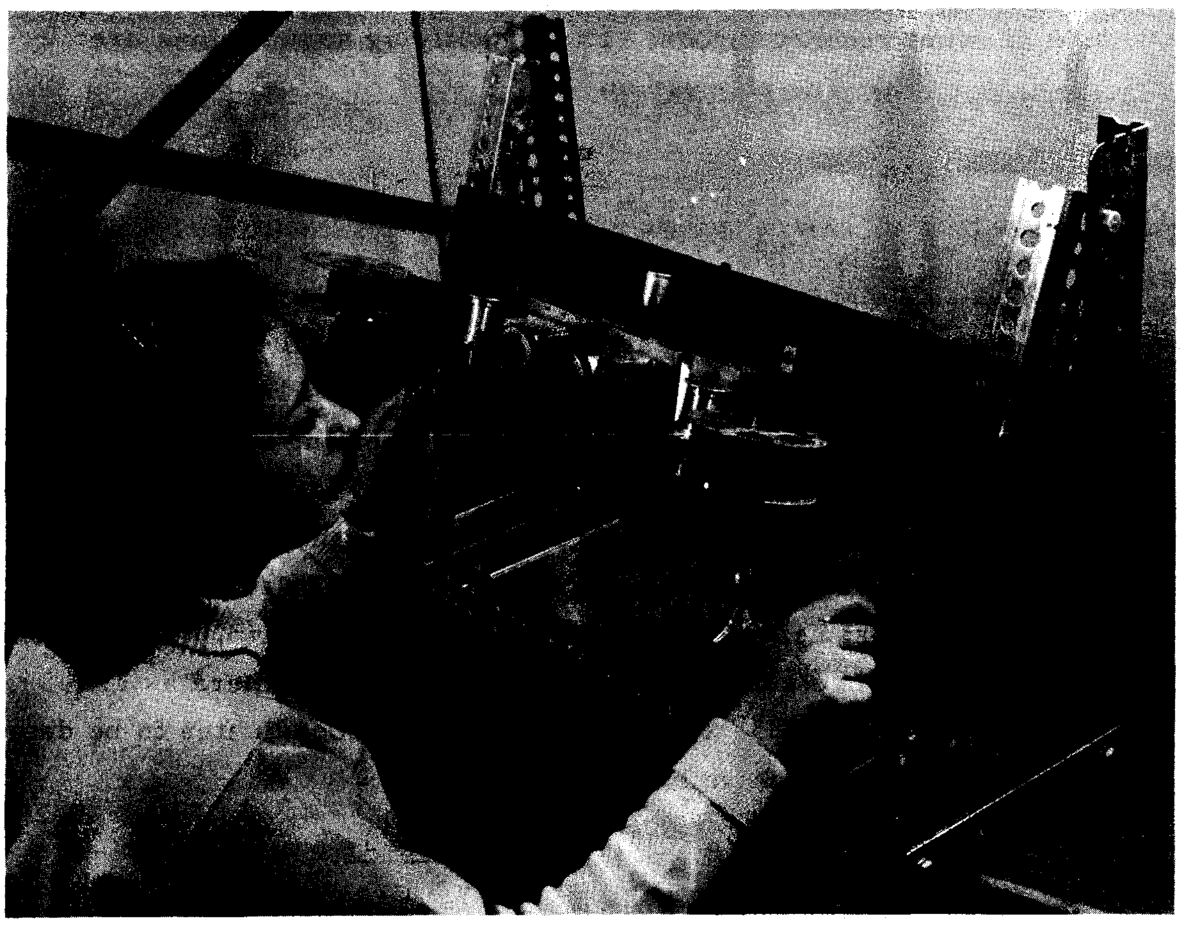

ZN-2516

Fig. 24. Use of the stereo viewer for film scanning.

C. Event Reconstruction

By virtue of the behavior of functions of small angles, a very simple and satisfactory solution was found for the geometrical problem of event reconstruction. The simplifying assumptions are:

(a) The expression

$$\frac{n_1 \tan \phi_1}{n_2 \tan \phi_2} \approx 1 \tag{11}$$

is a sufficiently accurate approximation of Snell's Law. At the largest angle encountered (11 deg) this ratio is actually 1.0033.

(b) The effects of 0.75-in. glass ($n \approx 1.5$) and 0.50-in. Lucite ($n \approx 1.5$) windows can be absorbed in a scaling factor.

The method used is illustrated in Fig. 25. A right-hand coordinate system was determined by demanding that the z axis be in the beam direction, the y axis be perpendicular to the windows, and the clearest reference fiducial mark be the origin. The bubble chamber windows were assumed perpendicular to the camera axis.

In Fig. 25, x, y, z are the bubble coordinates to be determined. Consider Line I: we have

$$\tan \alpha_1 = \frac{x - x'_1}{y - t} . \tag{12}$$

Similarly, for Line I', we have

$$\tan \beta_1 = \frac{(B + D) - x'_1}{(A + t) - t} . \tag{13}$$

By Eq. (11) we can write

$$n \frac{x - x'_1}{y - t} = \frac{(B + D) - x'_1}{A}, \tag{14}$$

where $n \approx 1.1$ is the index of refraction of the deuterium. Lines II and II' give

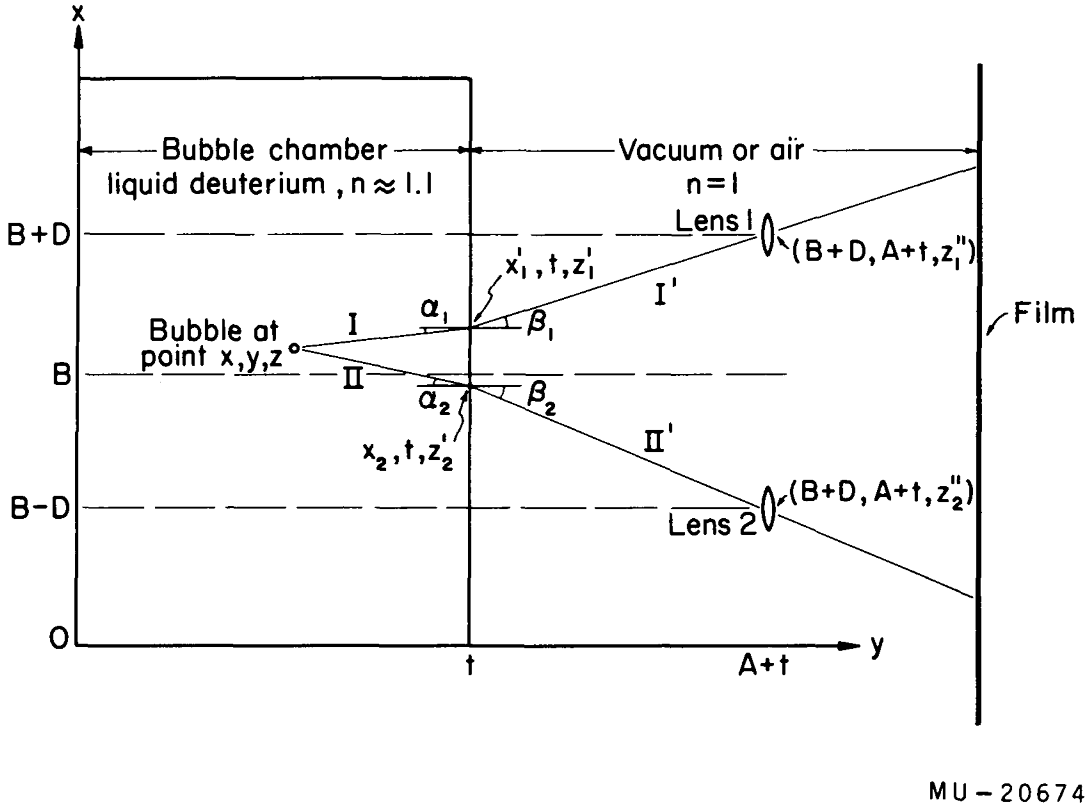

Fig. 25. Four-inch bubble chamber reconstruction optics (not to scale), showing the paths of light rays from a bubble at x, y, z to the film. The planes y = 0 and y = t are defined by the inside surfaces of the chamber windows.

$$n \frac{x - x'_2}{y - t} = \frac{(B - D) - x'_2}{A} \quad . \tag{15}$$

Combining Eqs. (14) and (15), we get

$$y = t + \frac{nA(x'_1 - x'_2)}{(x'_1 - x'_2) - 2D} \tag{16}$$

and

$$x = x'_1 + \frac{(B + D) - x'_1}{nA} (y - t) \ . \tag{17}$$

By analogy we may immediately write

$$z = z'_1 + \frac{(B' + D') - z'_1}{nA} (y - t) \ . \tag{18}$$

Now the two photographs taken by the camera simply contain images of the $y = t$ plane, scaled and inverted. In reality this plane, the inside of the bubble chamber window, has fiducial marks at the corners and center of a 2-in. square, which make measurements on the film very straightforward.

The error in using tangents rather than sines and Snell's Law (Eq. (11)) is 0.33% for the extreme case (an angle α_1 of 11%). This error is to be applied only to the second, "parallax-correction" term in Eq. (17) or Eq. (18). These terms are never larger than 1.0 cm. The error in y is largest when y is small, and is at most $0.3\% \times 5.5$ cm $=$ 0.016 cm.

Now, insert a 0.75-in. glass window in Fig. 25, with the plane $y = t$ as its left surface. It is obvious that the photographic image of a point on the plane appears farther from the lens axis than it should, because the ray must traverse the window at too small an angle β'. It appears to come from a point on the glass farther away than it should by $(0.75 \text{ in.})\cdot(\tan\beta - \tan\beta') \approx (0.75 \text{ in.})\cdot \tan\beta(1 - n_{\text{glass}}^{-1}) \approx (0.25 \text{ in})\cdot\tan\beta$. To a very good approximation this is equivalent to an increase in image size of $\frac{0.25 \text{ in. } \tan\beta}{18 \text{ in. } \tan\beta} = 1.4\%$. The error in this increment is only

1.3% at 11 deg. The effect of the 0.5-in. Lucite vacuum window is similarly small. Both effects may be absorbed in a scaling factor.

D. Film Measurements

For measurement of the events, a Benson-Lehner Oscar (Fig. 26) was used in connection with an IBM 026 readout punch. This system allows an operator to convert a set of coordinates on a 24 × 24-in. screen to IBM card punches by merely aligning cross hairs on a desired point and actuating a foot switch.

A stereoscopic projector was mounted so as to project either or both views onto the translucent screen from behind. The over-all chamber-to-screen magnification was 3.62. Each of the axes had 10,000 divisions across its entire range. This corresponds to 714 divisions per centimeter in the chamber or about 5 divisions per bubble diameter.

The entire system was so arranged that the operator had only to find the correct event, manually punch the frame number (three digits) and the number of prongs (one digit) once, move the cross hairs, and operate the foot switch. Projector view changes and all card-duplicating and -releasing functions were automatically programmed.

Every event had three Oscar cards: a master and two detail cards, each containing the roll number, frame number, and number of prongs as identifying punches. The master contained the coordinates (to four significant figures) of the reference fiducial marks as seen in both stereo views. The first detail card was punched with the coordinates, in View 1, of the event vertex and each track end point. The second detail card contained the same information but from View 2. Thus, the coordinates obtained from each view were: the reference fiducial mark, the event vertex, and the end point of each track. Positive-meson decays were handled in the same way as other two-prong events.

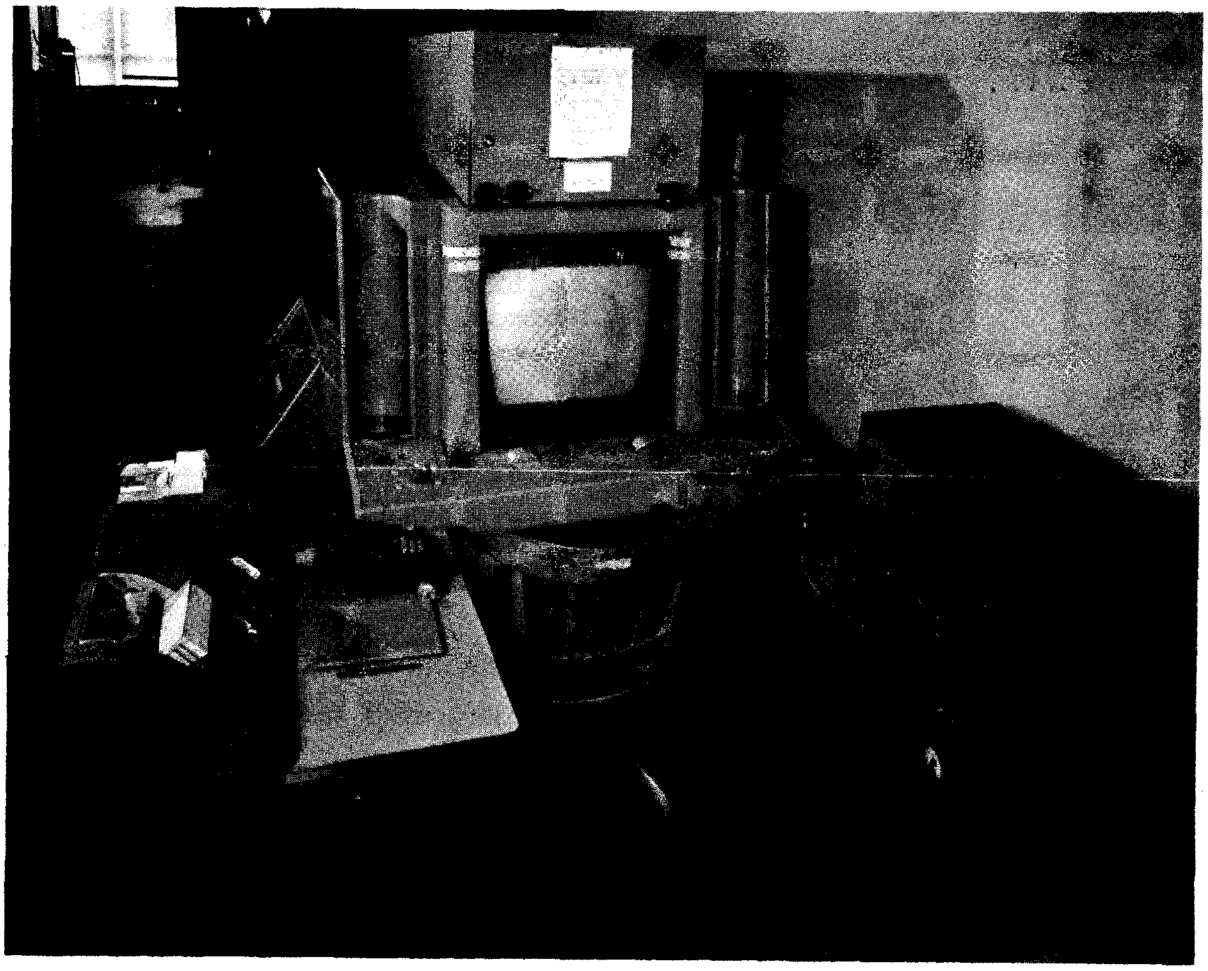

ZN-2515

Fig. 26. Benson-Lehner Oscar, showing operator's position before translucent screen. Projector view changes and IBM card-duplicating functions are controlled by the electronics at right. Cards are punched by unit at left.

No distinction was made between stopping and leaving tracks at this point. Forty-five minutes for a roll of 400 exposures is a typical Oscaring rate.

Careful Oscar measurements were made of the fiducial marks on both the front and rear windows, and the parameters in Eqs. (16), (17), and (18) were adjusted to give the correct answers. These measurements were checked on two different dates and it was found that the distances between fiducial marks varied as follows:

$$\frac{\delta\chi}{\chi} = -\frac{0.022 \text{ cm}}{5.075 \text{ cm}} = -0.43\%, \qquad \text{for 12 measurements,}$$

$$\frac{\delta y}{y} = +\frac{0.011 \text{ cm}}{5.454 \text{ cm}} = +0.20\%, \qquad \text{for 12 measurements,}$$

$$\frac{\delta z}{z} = -\frac{0.014 \text{ cm}}{5.075 \text{ cm}} = -0.28\%. \qquad \text{for 11 measurements.}$$

These data may be used as an indication of the systematic errors present. The fiducial spacing had been measured with a traveling microscope, and the chamber depth with a micrometer. Small corrections for thermal contraction were made to these measurements.

To measure the random errors, tracks were chosen that were closely parallel to the x, y, or z axis ($|\text{cosine} \geq| 0.9$). These tracks were measured twice at random intervals and half the rms value of their range differences obtained:

$\delta R_x = 0.028$ cm, for 53 tracks of random length,
$\delta R_y = 0.053$ cm, for 53 tracks of random length,
$\delta R_z = 0.037$ cm, for 55 tracks of random length .

The average over all space directions is $\delta R_{rms} = 0.041$. The rms errors ascribed to a coordinate x, y, or z are 0.707 of the above:

$\delta x = 0.010$ cm,
$\delta y = 0.038$ cm,
$\delta z = 0.026$ cm.

E. Rango Program

As a first step in the numerical analysis of the events, the Oscar cards were processed on an IBM 650 computer, using a specially written program called Rango. This program first calculated space coordinates of the vertices and end points of all tracks by using Eqs. (16), (17), and (18). From this information, the range R and direction cosines λ, μ, and ν were derived. These data were punched out, one card for each track. Each track was tested to determine whether it ended within 0.2 cm of the chamber boundaries. If so, it was considered a leaving track, and its card was punched following the stopping-tracks cards, if any.

A "tag" -- 888, 889, 899, 999, 88, etc. --was attached to each event indicating which tracks stopped (by an 8 punch) and which tracks left the chamber (by a 9 punch).

Besides R, λ, μ, and ν for each track, the cosines of the angles between tracks and a coplanarity index

$$\begin{vmatrix} \lambda_1\mu_1\nu_1 \\ \lambda_2\mu_2\nu_2 \\ \lambda_3\mu_3\nu_3 \end{vmatrix}$$

were printed to facilitate analyzing the events as scatterings.

The final card of the set contained data concerning the vertex: its space coordinates x_0, y_0, and z_0, and its distance r_0 from the center of the beam.

F. Range of the Decay Muons; Range-Momentum Curves

To determine the density of liquid deuterium under our expansion conditions, and to find range-momentum relationships, the average range of the decay muons ($T_\mu = 4.12 \pm 0.02$ Mev) track was determined. Only those $\pi^+ - \mu^+ - e^+$ decay chains in which the positron track was visible were used, in order to eliminate bias in choosing tracks. The average of 130 such events was found to be 1.0035 ± 0.0050 cm, with a standard deviation for a single measurement of 0.053 (Fig. 27). The error on the mean includes systematic errors ($\pm$ 0.0017 cm) as well as random errors ($\pm$ 0.0047 cm). When the rms measurement error $\delta R = 0.041$ cm is taken into account, the observed straggling is $\pm$ 0.034 cm.

Now, the mean excitation potentials of hydrogen and deuterium are closely the same. Since $Z = 1$ for both, only a small difference could arise from the difference in the reduced masses of the two atoms. Therefore ranges are the same in both media, if expressed in terms of electron densities. The density of bubble chamber deuterium may thus be determined:

$$\rho_d = \frac{M_d}{M_p} \cdot \frac{(\text{Range in hydrogen, g cm}^{-2})}{(\text{Range in deuterium, cm})} =$$

$$\frac{2.01471}{1.00813} \cdot \frac{(0.0656 \text{ g cm}^{-2})}{(1.0035)} = 0.1307 \pm 0.0013 \text{ g cm}^{-3} ,$$

where M_d/M_p is the ratio of the mass of a deuterium atom to the mass of a hydrogen atom.

Clark and Diehl[81, 82] determined the range of the μ^+ from the pion decay to be 1.103 ± 0.003 cm in bubble chamber liquid hydrogen, and published range-energy curves based on this range and the proton range-energy relation.[83, 84] We have simply scaled these curves in the ratio of the ranges to obtain those in Figs. 28 and 29.

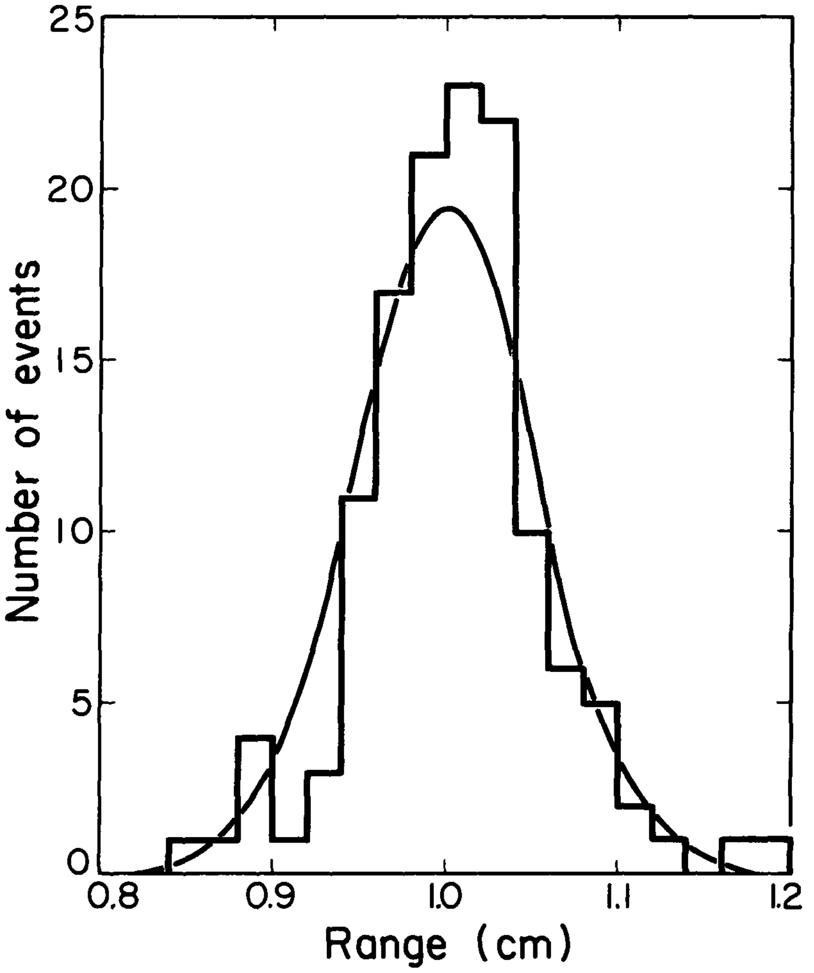

MU-20675

Fig. 27. Distribution of muon ranges from 130 $\pi^+ \rightarrow \mu^+ + \nu$ decays seen in the 4-inch deuterium bubble chamber. The Gaussian curve (standard deviation = 0.053 cm) is normalized to the same area as the histogram. The average range is (1.0035±0.0050)cm.

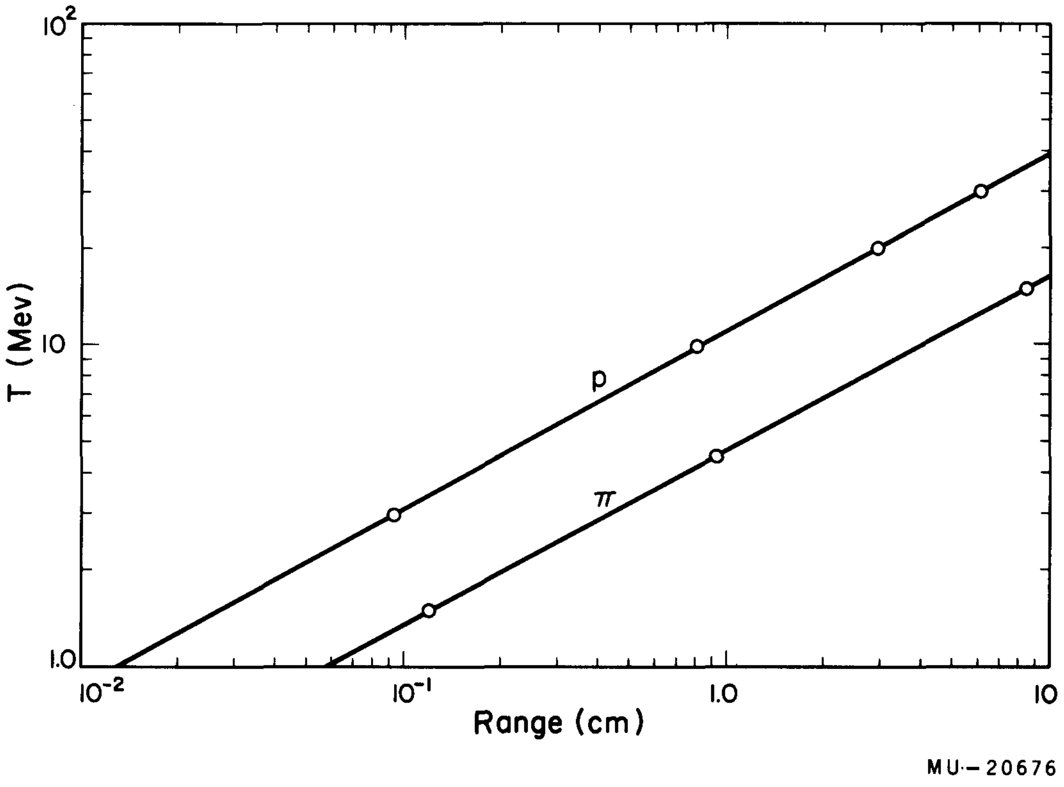

Fig. 28. Range-kinetic energy relationship for proton and π meson, based on the muon-range measurements of Fig. 27. The deuterium density is (0.131±0.0013) gm/cm^3.

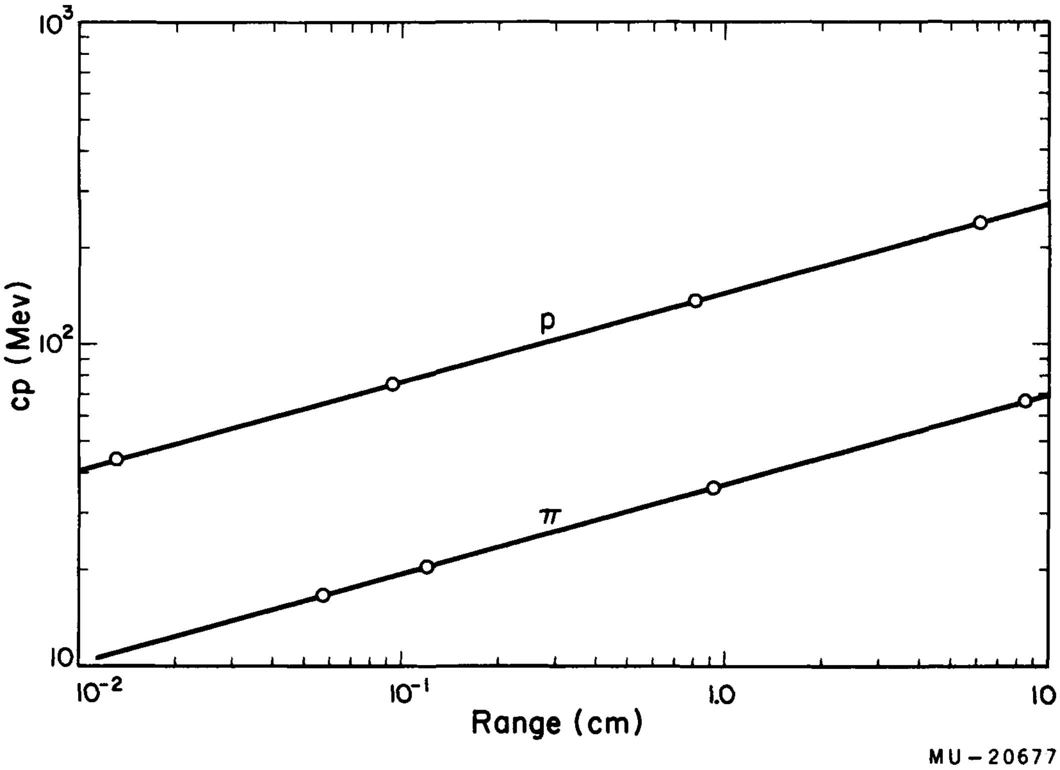

Fig. 29. Range-momentum relationships for proton and π-meson, based on the muon range measurements shown in Fig. 27. The deuterium density is (0.031±0.0013) gm/cm^3.

In the region of interest, R < 10 cm, the curves of Fig. 29 very closely follow the forms

$$P = 144\ R^{0.277}\text{(protons)}, \qquad (19)$$

$$P = 36.3\ R^{0.270}\text{(pions)}, \qquad (20)$$

where P is in Mev/c and R is in cm. These relationships were used in all programs that converted range to momentum.

V. KINEMATICAL ANALYSIS

A. General Considerations

In negative-meson production, the initial problem was to determine which of the three outgoing particles was the meson, and which were protons. To do this, each event was solved completely three times, each time with a different mass selection. An unambiguous choice was usually given by these results. Five IBM 650 programs, PEASOUP, PEAPOD, PEAGREEN, PINBALL, and PEAGARDEN,* were written to solve the five analyzable track configurations.

Ten fundamental quantities must be obtained or inferred from measurements on each event. These are the three momentum components for the three outgoing particles, and the photon energy, k. At most, nine of these can be obtained directly from measurements, using the range-momentum relationships of Fig. 29. Four conservation equations, one for each component of four-momentum, must be used in obtaining the photon energy and the other missing data:

$$F_1 = \sqrt{p_1^2 + M_1^2} + \sqrt{p_2^2 + M_2^2} + \sqrt{p_3^2 + M_3^2} - k - M_d = 0, \tag{21}$$

$$F_2 = \lambda_1 p_1 + \lambda_2 p_2 + \lambda_3 p_3 = 0, \tag{22}$$

$$F_3 = \mu_1 p_1 + \mu_2 p_2 + \mu_3 p_3 = 0, \tag{23}$$

$$F_4 = \nu_1 p_1 + \nu_2 p_2 + \nu_3 p_3 - k = 0, \tag{24}$$

where $\hbar = c = 1$,

---

*The leguminous names of these programs are due to Richard I. Mitchell, who wrote all of them except Pimiki, and noticed that the phrase "Photoproduction: Pi Plus Proton Plus Proton" contains seven P's.

k = photon energy or momentum,

M_D = deuteron mass = 1875.49 Mev,

$M_i = M_j$ = 938.213 Mev, M_k = 139.63 Mev, with $i, j, k = 1, 2, 3$ permuted.

If the event has three tracks and all leave the chamber, there are exactly four unknown data: three momentum magnitudes and the photon energy. However, if at least one track stops, conservation equations are left over that in general will not be satisfied by the derived data. It is important for two reasons that such an event be adjusted to conform to all the conservation equations: (a) Quantities derived from a nonconserving event (such as w^2 used in the extrapolation of Sec. I. D) are also nonconserving and sometimes fall outside physical limits. (b) Maximum use is made of the data since errors in independent measurements are reduced if they are correlated through the conservation laws.

B. Lagrange Multipliers

To make a least-squares adjustment to the conservation laws, the method of Lagrange multipliers,[85, 86] successfully used by the Alvarez group,[87] was adapted for our use. The problem is to minimize

$$S = \sum_{i=1}^{n} w_i \left(x_i^A - x_i^M\right)^2 \tag{25}$$

subject to m constraints of the form

$$F_j(x_i^A) = 0, \text{ for } j = 1, \ldots, m. \tag{26}$$

The quantities $x_1, \ldots, x_i, \ldots, x_n$ are statistically independent observables with which are associated weights $w_i = \sigma_i^{-2}$, where σ_i is the standard deviation in x_i. The superscripts A and M indicate adjusted and measured quantities, respectively.

The function

$$G = \sum_i^n w_i V_i^2 + 2 \sum_j^m \lambda_j F_j (x_i^M + V_i) \tag{27}$$

is formed, where $V_i = x_i^A - x_i^M$, the residual for x_i. The λ's are the Lagrange multipliers. To simplify the procedure, we expand

$$F_j(x_i^M + V_i) \approx F_j(x_i^M) + \sum_i \frac{\partial F_j}{\partial x_i} (x_i^M) V_i + \dots \quad . \tag{28}$$

Now if we demand that

$$1/2 \left(\frac{\partial G}{\partial V_i}\right) \approx w_i V_i + \sum_j \lambda_j \frac{\partial F_j}{\partial x_i} (x_i^M) = 0; \text{ for } i = 1, 2, \cdots n, \tag{29}$$

and

$$1/2 \frac{\partial G}{\partial \lambda_j} \approx F_j(x_i^M) + \sum_i \frac{\partial F_j}{\partial x_i} (x_i^M) V_i = 0, \text{ for } j = 1, 2, \cdots, m, \tag{30}$$

we get (n + m) linear equations which may be solved for V_i and λ_j. Because of the approximation used, the V_i 's will not be exact unless the constraints F are linear in x_i. However, an iterative procedure based on this technique can be used to give as good a solution to Eqs. (25) and (26) as desired. Moreover, after the residuals V_i have been calculated, and the adjustment made, it is easy to find the minimum value of S, i.e. χ^2, and to calculate errors on all derived quantities.

For an overdetermined negative-meson event, Eqs. (21)-(24) which are left over are used as the F's in Eqs. (26)-(30). As a compromise between completeness and speed, the four space variables x_0, y_1, y_2, and y_3-- i.e., the vertex x coordinate and the track end-point y coordinates--were chosen as adjustable variables. The y coordinates were chosen because they are the least accurately measured of the coordinates, being in the direction of the camera axis. Some adjustment in the x direction was needed to "line up" the event in the beam direction, therefore x_0 was also chosen.

The weights assigned to these variables are based on the measurements described in Sec. III. D: $\delta x_0 = 0.01$, and $\delta y_1 = \delta y_2 = \delta y_3 = 0.04$ cm. These variables are quite independent, since separate positionings of the cross hairs are required for each. However, the important effects of multiple Coulomb scattering and range straggling were ignored. This was done to keep the programs from becoming excessively complicated. A rough calculation of multiple scattering indicates that protons have a projected rms deviation from the line of their original direction of 1.2% of their range. For pions, the deviation is 2.9%. In addition, range straggling is on the order of a few per cent. For 1-centimeter proton tracks it is calculated to be 1.5% and for 1-centimeter pion tracks it is 3.5%.

For tracks several centimeters long, these effects are larger than the measurement errors. However, for tracks up to a few millimeters in length, the measurement errors greatly exceed those due to straggling and scattering. The practical result of these effects is that our distribution in the minimum value of S is not a good χ^2 distribution but has a long tail due mainly to events with long tracks.

After the adjustment programs had been written, it became apparent that a z adjustment was necessary to solve some events. An ad hoc z_0 adjustment was then incorporated in the programs which could be called in only when necessary. This adjustment was apart from the least-squares adjustment and could therefore introduce systematic errors. The z_0 steps were kept as small as practicable (-0.01 cm) to keep such errors to a minimum.

C. Outline of Programs

The initial step in the programs was to assign masses for each prong. One track was chosen as the pion and the other two were assumed to be protons. After preliminary calculations, a combined nonconservation constraint function

$$F = \sqrt{\sum_{j=1}^{m} F_j^2}$$ was tested. If it was greater than an arbitrary value (100 Mev, c = 1), that mass choice was discarded immediately and no iterations were made. Otherwise, iterations were continued until either (a) F was below a set limit (1 Mev), and the step in "residual space"

$$V = \sqrt{\sum_{i}^{m} V_i^2}$$ between successive iterations was below a chosen limit (0.001 cm), guaranteeing that S was near its minimum value, or (b) a maximum number of iterations (usually 10) had been made. The average of the number of iterations required for the correct mass choice was between 3 and 4.

When the adjustment was concluded, the programs tested that the results were as follows:

$$145.83 < k < 200 \text{ Mev}, \tag{31a}$$

$$r_0 \leq 1.0 \text{ cm}, \tag{31b}$$

$$-1.0 \leq z_0 \leq 6.0 \text{ cm}, \tag{31c}$$

$$F < 1.0 \text{ Mev}, \tag{31d}$$

$$\chi^2 < 10. \tag{31e}$$

These tests verified that the photon energy was reasonable, the event originated in the beam cylinder and within the chosen z_0 limits, the constraints were sufficiently satisfied, and χ^2 was small. If these conditions were met, further data were derived from the event analysis, such as the Baldin parameters[34] p and q, the quantities p^2 and w^2

used in the polology extrapolation (see Sec. I. D), and the pion momentum and direction in two reference frames: the γ-n center-of-mass and the γ-d center-of-mass frames.

The entire set of calculations was repeated for each of the three possible mass permutations.

D. PEASOUP, the "888" Case

The program handling the case (19% of all π^- events) in which there are three prongs, all stopping in the chamber, was named PEASOUP. Since we have $p \propto \mathbf{R}^{1/4}$, where p is the particle momentum for range **R**, momenta are relatively well determined compared with direction cosines, for tracks whose ranges are known. Therefore Eq. (21) was chosen to calculate the best initial value for k, and Eqs. (22), (23), and (24) were used as constraints.

The ad hoc z_0 adjustment was called in only if F_4 (Eq. (24)), the nonconservation in p_z, was above a certain limit (2 Mev/c). If so, z_0 was altered by an increment of -0.01 cm and the calculations repeated. Only 17% of the "888's" required such an adjustment.

E. PEAPOD, the "889" Case

To give the best initial solution for the case in which one track leaves the chamber, (50% of all π^- events) Eqs. (21) and (24) were solved for k and p_3, the unknown momentum. When solved these equations give

$$p_3 = \frac{-p' \nu_3 \pm \sqrt{p'^2 \nu^2_3 - (1 - \nu^2_3)(M^2_3 - p'^2)}}{(1-\nu^2_3)} \tag{32}$$

where

$$p' \equiv (E_1 - \nu_1 p_1 + E_2 - \nu_2 p_2 - M_D)$$

and

$$k = \nu_1 p_1 + \nu_2 p_2 + \nu_3 p_3 \, . \tag{33}$$

The sign of the radical cannot be determined generally, and both choices may give a reasonable photon energy for $\nu_3 > 0$. Events of this type were run with both signs and the solution with the smaller χ^2 was chosen. Approximately 5% of all "889" cases gave ambiguous results, but these were generally resolved by qualitative ionization considerations.

Good events, if not well measured, or if distorted sufficiently by multiple scattering, could give imaginary solutions for p_3. The radicand was tested on each iteration. If negative, z_0 was moved by -0.01 cm. Since this was again apart from the least-squares adjustment, a small systematic error may have been introduced. About 27% of the "889" events required a z_0 adjustment.

Besides the general requirements demanded of all events (Eq. (31)), Peapod also required $R(p_{3\,calc}) \geq R_3$ (observed). That is, the range derived from the adjusted p_3 had to be greater than the range of Track 3 observed in the chamber.

F. PEAGREEN, the "899" Case

In the "899" case in which two tracks leave the chamber, (10% of all π^- cases), there are three unknowns: k, p_2, and p_3. Equations (22) and (24), linear in these variables, were solved explicitly for p_2 and p_3 in terms of k:

$$p_2 = \frac{\lambda_3 k + p_1 (\lambda_1 \nu_3 - \lambda_3 \nu_1)}{\lambda_2 \nu_3 - \lambda_3 \nu_2}, \tag{34}$$

$$p_3 = \frac{\lambda k + p_1 (\lambda_1 \nu_2 - \lambda_2 \nu_1)}{\lambda_2 \nu_3 - \lambda_3 \nu_2} \tag{35}$$

These forms were substituted into Eq. (21), giving

$$\sqrt{p^2_1 + M^2_1} + \sqrt{p^2_2(k) + M^2_2} + \sqrt{p^2_3(k) + M^2_3} + k - M_D = 0, \tag{36}$$

which was solved for k by Newton's method.

Solving this set of three equations is equivalent to finding the points of intersection of a line with half of a hyperboloid of two sheets in p_2 - p_3 - k space. Obviously, two solutions (perhaps imaginary) are possible. Where necessary, the line was forced to intersect the hyperboloid by the ad hoc z_0 adjustment. Whenever the number of iterations in the Newton's-method solution for k exceeded 9, z_0 was altered by an increment of -0.01 cm and the calculations were repeated. Normally only 1 or 2 Newton iterations were needed to find a solution for k if a real one existed. In case both solutions for k fell within the range of interest (k = 145.83 to 200 Mev), both solutions could be found by running all events twice, first with the initial value k = 150 Mev for Newton's method, and the second time with k = 250 Mev as the initial value. No events were found which had both values of k in the acceptable region.

In addition to the general requirements on the results (Eq. (3.1)), we also demanded

$$R(p_{2\ \mathrm{calc}}) \geq R_{2\ \mathrm{observed}},$$

$$R(p_{3\ \mathrm{calc}}) \geq R_{3\ \mathrm{observed}}.$$

G. PIMIKI, the "999" Case

If all three tracks leave the chamber, there are four unknowns, p_1, p_2, p_3, and k, to be found by using the four conservation equations. This case(1% of all π^- events) was solved as follows:

$$p_i = a_i k, \quad \text{for } i, j, k, = 1, 2, 3, \text{ permuted, and} \tag{37}$$

$$\sqrt{a_1{}^2 k^2 + M_1{}^2} + \sqrt{a_2{}^2 k^2 + M_2{}^2} + \sqrt{a_3{}^2 k^2 + M_3{}^2 - M_3{}^2} - k + M_D = 0, \tag{38}$$

where

$$a_i = \frac{\begin{vmatrix} \lambda_j \lambda_k \\ \mu_j \mu_k \end{vmatrix}}{\begin{vmatrix} \lambda_1 \lambda_2 \lambda_3 \\ \mu_1 \mu_2 \mu_3 \\ \nu_1 \nu_2 \nu_3 \end{vmatrix}} \tag{39}$$

Again, Newton's method was used. Besides the requirements (Eq. (31)), the range of each track as calculated from its momentum had to be greater or equal to its observed range:

$$R(p_{3\ \text{calc}}) \geq R_{3\ \text{observed}},$$

$$R(p_{2\ \text{calc}}) \geq R_{2\ \text{observed}},$$

$$R(p_{1\ \text{calc}}) \geq R_{1\ \text{observed}}.$$

No adjustment is possible, since there are no constraint equations.

H. PEAGARDEN, the "88" Case

A two-prong event with both tracks stopping could be a negative meson event with one track too short or too lightly ionizing to be seen. It could also be a $\pi^+ - \mu^+$ decay. Both possibilities are considered by PEAGARDEN.

(a) The negative-meson case (22% of all π^- events). This has four unknowns: k and the three momentum components of the unseen track. It is solved by the series of steps:

$$p_{3x} = -(p_1\lambda_1 + p_2\lambda_2) , \tag{40}$$

$$p_{3y} = -(p_1\mu_1 + p_2\mu_2) , \tag{41}$$

$$k = \frac{M_3^2 + p_{3x}^2 + p_{3y}^2 - (M_D - E_1 - E_2)^2 + (p_{1_z} + p_{2_z})^2}{2(M_D - E_1 - E_2 + p_{1_z} + p_{2_z})} ,$$

where (42)

$$E_1 = \sqrt{p_1^2 + M_1^2} , \quad E_2 = \sqrt{p_2^2 + M_2^2} , \text{ and } p_{3z} = k - \nu_p p_1 - \nu_2 p_2 .$$

In addition to the tests (Eq. (31)), the calculations on the unseen track are examined. If this track is computed to be longer than 0.2 cm and yet stop within the chamber boundaries, it should have been seen with no difficulty. This is sufficient reason to discard the mass choice that gave such a third track.

(b) The positive-meson case. Since the identifying feature of a positive-meson event is its decay, both tracks of an "88" event are tested to determine whether either is within three standard deviations ($\pm$ 0.16 cm) of the muon range (1.00 $\pm$ 0.053 cm). If so, the event is handled as a possible $\pi^+ - \mu^+$ event. The origin of the assumed π^+ is examined to see whether it begins in the allowed beam region (Eqs. (31b) and (31c)). If the event satisfies these criteria, the momentum of the π^+ is calculated from the range-momentum relationships of Fig. 29, and this information is punched on a separate card.

I. Chamber Boundaries

In making corrections to the data for chamber geometry, the planes defined by the inner faces of the windows, $y = 0$, and $y = 5.454$ cm, formed two of the chamber boundaries. To determine the effective limits of visibility around the periphery of the chamber, the end points of 45 tracks that left the chamber through the walls were plotted, as shown in Fig. 30. The Oscar operators had been instructed to measure what they considered to be the last visible bubble of leaving tracks. Except in the region of the VP cell, the points lay close to a circle of radius 4.60 cm. The VP cell, which obscures part of the chamber, was fitted to an arc of a circle 6.80 cm in radius, whose center was displaced from the center of the chamber. Choice of the chamber boundary in the region of the VP cell was facilitated by measurements of the VP cell on a projection table.

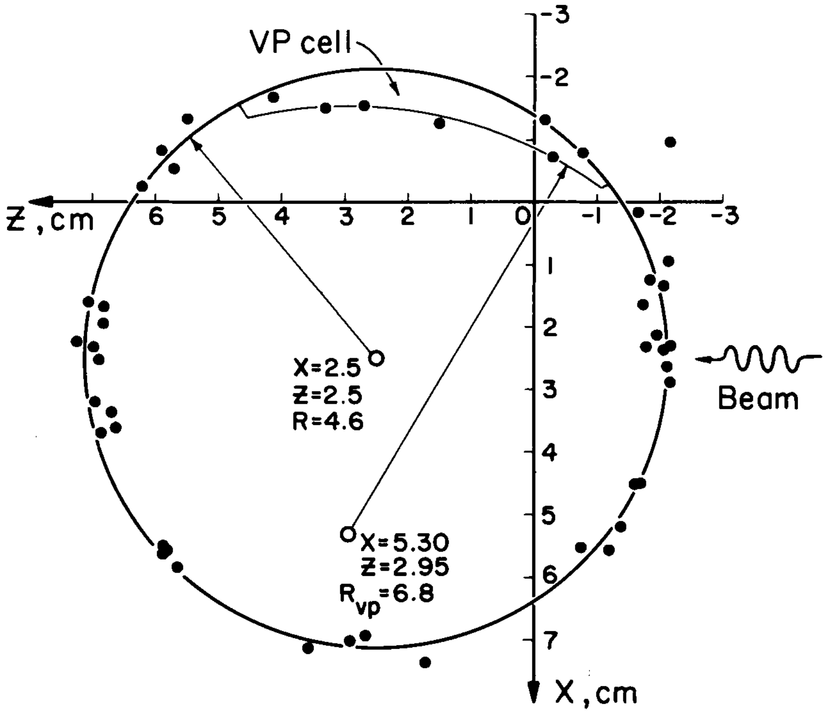

MU-20678

Fig. 30. Effective boundaries of 4-inch deuterium bubble chamber, determined by the end points of 45 leaving tracks. The choice of the boundary in the region of the VP cell was guided by measurements on a projection table.

J. JMC and POPINJAY: Weighting of Two-Prong Events

It is clear that an analyzable "88" negative-meson event or a $\pi^+ - \mu^+$ decay might have been unanalyzable had it occurred somewhere in the chamber where either or both visible tracks could have left the chamber. To weight each event accordingly, two Monte Carlo programs, JMC and POPINJAY, were written for the IBM 704 to randomly displace and reorient each event repeatedly, each time testing to see whether it remained entirely within the chamber. In JMC (Junior Monte Carlo), which handled negative-pion "88" events, the laboratory-system coordinates of each event that were randomly varied were r_0, θ_0, z_0, and ϕ_0. The quantities r_0 θ_0, and z_0 are the cylindrical coordinates of the event vertex with respect to the beam centerline, and ϕ_0 is the angular orientation of the event about a line parallel to the beam direction through the event vertex. Choices of r_0 were weighted so that they occurred with the probability actually observed for known events (Sec. III. A).

In POPINJAY (the name comes from the words "positive pion"), the same event parameters were randomly varied, except that the true production point of the pion, rather than the event vertex, was considered the origin. In addition to these parameters, the two coordinates, cos θ_μ and ϕ_μ, defining the muon decay direction were randomly varied so that the muon could go in any direction with equal probability.

The programs gave each event successive random positions until 100 analyzable positions had been counted, or until a total of 500 positions had been counted. The weight of the event was given by

$$wt = \frac{\text{(Total number of positions tested)}}{\text{(Number of analyzable positions found)}} .$$

The average weight of the negative pion events whose third track was invisibly short was 1.33 and that of the positive pions 1.14. Normally the counting ended when the number of analyzable positions counted reached 100. The statistical error due to the Monte Carlo procedure was negligibly small. In the testing of the events, the chamber boundaries estimated in the preceding section (V. I) were used.

K. Results of the Event Analysis

Events were selected from the general background of photoproton scatterings by a combination of IBM 650 analysis, as described previously, and judgment on the part of the physicists who examined each event visually. This judgment was based on qualitative track-density considerations, presence or absence of coplanarity, and rough momentum-balance requirements. With some experience, one can usually distinguish a meson from near-by protons because its average track density is smaller.

Table IV summarizes the results of the analysis and selection procedure. The numbers of events of different types are presented, along with their average laboratory-system photon energies and errors. The average chamber-geometry weighting factors (Sec. V. J) are also included for two-prong events. The numbers of photoproton scatterings which, according to the scanners, simulated meson-production events are also included in the lower lines of the table.

To estimate the number of photoproton scatterings that were accepted as meson events by the over-all selection procedure, the 20 rolls of film exposed at a peak bremsstrahlung energy E_{max}=138 Mev (below the meson-production threshold) were analyzed in exactly the same manner as the main data. These rolls were scanned, measured and visually examined at random times by individuals unaware of their nature.

To compare beam flux incident on the bubble chamber during the 138-Mev run with the beam incident during the 194-Mev run, the intensities were integrated over the limited photon energy interval k = 0 to 100 Mev. The background from photoprotons is mainly caused by photons of energy considerably below 100 Mev, so that this is a reasonable method of comparing beam flux for an estimation of background. When compared in this way, the total beam at $E_{max}=138$ Mev was 0.080 of that at $E_{max}=194$ Mev.

As shown in Table IV, 35 of the photoproton scatterings found in the 138-Mev data satisfied the programmed criteria (Eqs. (31), etc.) for analyzable meson events. Of these, only one was considered a meson event by the over-all selection and analysis procedure. This is evidence that our over-all procedure gave good background rejection.

On the other hand, the possibility existed that good events, poorly measured or difficult to measure owing to short tracks, may have been rejected as photoproton scatterings. Those events that were judged as good events by visual examination but did not satisfy the programmed criteria were remeasured twice. The result was that after a maximum of three measurements, 8.6% of the "888", 22% of the "889," 20% of the "899," and 7.2% of the "88" events did not satisfy the programmed criteria. The assumption was made that half of those events were photoproton scatterings that resembled meson-production events on visual inspection. A correction of half the above percentages was then applied to the results based on the acceptable events. As it happened, the results of Sec. VI were based mainly on the "888" and "88" events, so that the net correction was about 4%.

Table IV

Summary of the event analysis

Event type	Number found in data at 194-Mev peak energy	Average weight, based on chamber geometry	Average photon energy (Mev)	Rms error in photon energy due to measurement errors (Mev)	Number in data at 138-Mev peak energy that satisfied programmed criteria for meson events	Number in data at 138-Mev peak energy selected as meson events
π^-888	226		161	0.5	0	0
π^-889	650		174	3.3	0	0
π^-899	136		182	4.8	0	0
π^-999	6		184	-	1	0
π^-88 High*	22		192	2.6	4	0
π^-88 Low**	269	1.73	160	1.0	9	1
π^-89	706	Not analyzable				3
π^-99	55					0
π^+88	447	1.30			21	0
Photo-proton scatterings 3-prong	419				126	
Photo-proton scatterings 2-prong	496				180	

*Meson too lightly ionizing to be visible
**One proton invisibly short

VI. RESULTS

A. The σ^-/σ^+ Ratio from Deuterium

1. Pion energies and angles included

Because of the requirement that all positive pions stop in the bubble chamber, the pion energies were necessarily limited to small values. Pions included in the deuterium σ^-/σ^+ ratio were of energy 3 Mev to 9 Mev, corresponding to ranges of 0.44 cm to 3.3 cm. Thus, all pions were of sufficiently long range for reliable identification, and still short enough so that positive-pion tracks normally ended in the chamber. Three energy bins between these limits were used, as shown in Table V. The distribution of pions of 3 to 9 Mev kinetic energy was roughly isotropic in the laboratory system before chamber geometry corrections were made. The data were divided into six lab-angular bins each containing roughly equal solid angles, so that Coulomb corrections could be made as a function of pion energy and angle.

2. Positive pions

All together, 299 positive-pion events were found acceptable as data for the σ^-/σ^+ ratio. When corrected for chamber geometry by means of the POPINJAY program (Sec. V. J), this number became 342±33. Further corrections to the positive-meson data were estimated as follows:

Scanning efficiency	+0.2%
H^1 impurity in D_2	-1.0%
Muon range not acceptable	+0.01%
Pion decay in flight	+1.2%

The net correction was judged to be negligible. Errors, apart from those of a purely statistical nature, were also assumed negligible.

The average laboratory-system energy and angle of the mesons accepted were 5.95 Mev and 91 deg. Final data are presented in Table V.

Table V

Positive pions

Meson kinetic energy (lab) (Mev)		Meson angle (lab) (deg)					
		A 0 - 45	B 45 - 72	C 72 - 90	D 90 - 108	E 108-135	F 135-180
(1)	N_0*	17	19	21	15	23	17
3-5	N_w	17.26	19.02	21.05	15.05	23.08	17.30
(2)	N_0	17	26	18	19	25	11
5-7	N_w	18.82	26.35	18.78	19.76	26.88	12.18
(3)	N_0	6	16	10	10	19	10
7-9	N_w	7.76	23.62	15.72	17.66	28.59	13.47

*N_0 = observed number of pions

N_w = number weighted for chamber geometry

3. Three-Prong Negative Mesons

Since the identification of negative mesons depended on the configuration of the recoil protons, and since mesons belonging to a given bin were produced by a distribution of photon energies, it was necessary to study the dynamics for each meson bin at various photon energies to insure that no events could be missed because of particles' leaving the chamber without being seen.

It was found possible to choose z_0 limits for each meson bin such that three-prong events of up to 194 Mev photon energy were easily visible if they originated between these boundaries. The method used in assigning z_0 limits was the one that gave the larger usuable region:

(a) If the negative pion itself was of such low energy (3 to 5 Mev) that it always stopped in the chamber, the z_0 limits were chosen so that at least one-third of the range of the longer proton track lay within the chamber, if the shorter proton just stopped at the chamber boundary. This guaranteed that both protons were still easily visible even if neither remained entirely within the chamber. The requirement that one-third of a track lie within the chamber was established empirically, by examining the calculated ranges of all leaving tracks in the negative-pion data.

(b) If the negative pion itself was of high enough energy to leave the chamber, the z_0 limits chosen were such that one-third of the total range of the highest-energy proton possible be within the chamber. To account for those events produced in other parts of the chamber, the events were weighted in the ratio of the chamber length used for the positive pions (7.0 cm) to the path length used for the three-prong events. A total of 204 three-prong negative-pion events, mostly of the "888" type, with an average weight of 1.06, was included.

4. Two-Prong Negative Mesons

Two-prong events with negative mesons in the allowed energy range were individually corrected for chamber geometry by the JMC program described in Sec. V. J. Only those originating between the identical z_0 limits used for positive mesons were accepted.

Above a certain photon energy (k = 175 to 180 Mev) it is kinematically possible in some meson bins for one proton to be sufficiently energetic to leave the chamber with high probability, while the shorter proton track is still too short to be visible. A small correction was made such that the fraction of the two-prong events in this high-energy range was made to be the same as the fraction of three-prong events. This amounted to a correction of 4.4% of the net number of all negative-meson events included.

A total of 166 two-prong events was used, with an average weight, based on chamber geometry, of 1.28.

5. Instrumental Corrections to the Negative-Pion Data

If the energy of the photon producing a negative meson at a forward laboratory-system angle is too low (k = 145.83 to 155 Mev), too little energy may remain to guarantee that at least one of the protons has a visible range ($R > 0.1$ cm). The number of events missed for this reason was estimated in the following manner.

A histogram of the meson momentum distribution in the (γ+d) center of mass was obtained for all observed events of photon energy k = 150 to 155 Mev, as shown in Fig. 31. The momentum was plotted in units p/p_{max}, where p_{max} is the maximum possible c. m. momentum of the pion at the photon energy of the observed event. Only those events with c. m. momentum and angle for which at least one proton is guaranteed a visible range ($R > 0.1$ cm) in the laboratory system were included in this distribution.

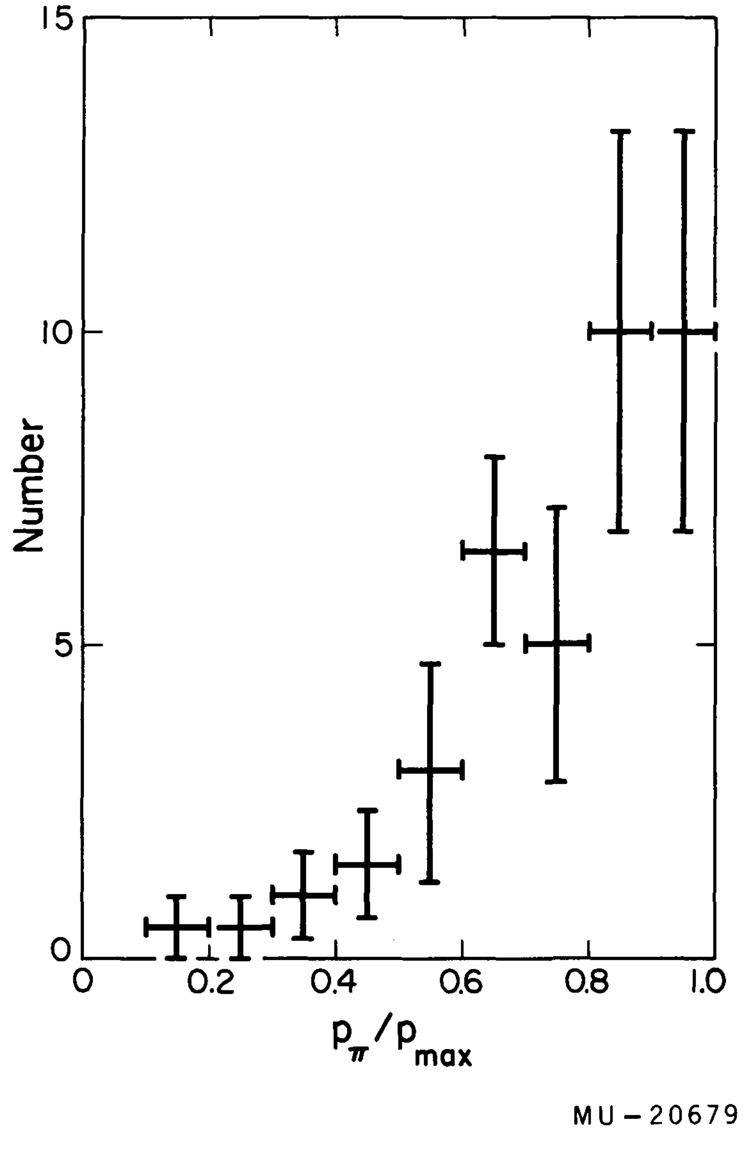

Fig. 31. Distribution of pion momentum in $\gamma + d$ c.m., for events of photon energy k = 150 to 155 Mev. Units are p_π/p_{max}, where p_{max} is the highest momentum possible at the photon energy of each event.

At each photon energy in the range 150 to 155 Mev, certain pion c. m. momenta and angles correspond to the lab meson bins of Table VI. Utilizing the observed c. m. momentum distribution and assuming isotropy, one obtains as a function of photon energy the fraction of all events at a given photon energy expected to occur with pion c. m. momentum and angle corresponding to one of the lab bins of Table VI. The number of actual events expected in each of these bins in the photon energy range 150 to 155 Mev was obtained by multiplying the calculated fractions by the total numbers of events seen in 1-Mev energy intervals within this range. For meson-energy bins 1, 2, and 3 (Table VI) the numbers expected were 2.3 ± 0.7, 4.6 ± 1.4, and 6.0 ± 1.8, respectively, distributed mainly in the region 0 to 45 deg (lab). The errors on these numbers are due to uncertainties in the c. m. momentum distribution.

An isotropic distribution, assumed above, was found by Adamovich et al.,[13] and is consistent with the data from this work (Sec. VI. C).

All the expected events might have been unobservable, had the two protons in each event divided the available energy equally. In that case, the correction for those missed would have been 12.9 events, or about 4% of the entire data. However, when the expected numbers were compared with the numbers corrected for chamber geometry actually observed--3.4, 4.3, and 9.7 in bins 1, 2, and 3, respectively--it was decided that no such correction was necessary.

A grand total of 369 acceptable events was corrected to 428 ± 22 by the chamber geometry weighting. Further corrections are summarized as follows:

Scanning efficiency (Sec. IV. B)	+ 1.6%
Meson charge exchange in deuterium	+ 0.05%
Events difficult to measure (Sec. V. K)	+ 4.0%
Net correction	+ 5.65%

Table VI

Meson kinetic energy (lab) (Mev)		Meson angle (lab) (deg) A 0-45	B 45-72	C 72-90	D 90-108	E 108-135	F 135-180
	N_w*	13.12 (13)	22.15 (22)	22.22 (21)	15.09 (14)	19.36 (18)	20.76 (18)
(1)	N_I	13.86	23.40	24.56	20.92	22.88	25.10
3-5	N_{pp}	14.69	24.81	25.27	22.21	24.15	25.97
	$N_{\pi p}$	11.94	20.50	21.42	18.98	20.82	22.58
	N_w	19.83 (19)	28.44 (27)	20.44 (19)	18.22 (14)	34.72 (30)	19.59 (15)
(2)	N_I	20.95	30.05	21.59	19.25	41.27	20.70
5-7	N_{pp}	21.44	31.28	23.46	20.26	42.62	23.17
	$N_{\pi p}$	18.32	26.97	20.40	17.77	37.72	20.61
	N_w	20.66 (17)	36.11 (31)	33.30 (26)	26.46 (22)	38.73 (30)	18.92 (13)
(3)	N_I	21.83	38.15	35.18	28.12	40.92	22.21
7-9	N_{pp}	22.61	40.33	38.05	30.58	42.45	23.46
	$N_{\pi p}$	19.66	35.53	33.67	27.30	37.90	21.40

*N_w = Number of events weighted for chamber geometry. (Observed number is given in parentheses.)

N_i = Number including all instrumental corrections.

N_{pp} = N_I corrected for proton-proton Coulomb interactions only.

$N_{\pi p}$ = N_{pp} corrected for pion-proton Coulomb interaction.

After these corrections were added, the net total became 471±31. The numbers N_I tabulated for each meson bin in Table VI include the chamber geometry weighting and the corrections discussed in this and the preceding subsection. Errors assumed for the corrected numbers include the statistical error and a 50% error in the corrections. The error introduced by the chamber geometry calculation is believed to be negligible in comparison with the ordinary statistical error.

The average laboratory-system energy and angle of the negative pions accpeted were 6.27 Mev and 90 deg.

6. Coulomb Corrections

a. The Proton-Proton Coulomb Correction (Positive)

Using the impulse approximation (Sec. I. C) Baldin[34] has calculated the cross sections for deuterium photopion production,

$$\frac{\partial^2 \sigma^{\pm}}{\partial p \partial q} = A(p, q) \left| K^{\pm} \right|^2 + B(p, q) \left| L^{\pm} \right|^2 , \tag{43}$$

where $\left| K^{\pm\ 2} \right|$ and $\left| L^{\pm\ 2} \right|$ are respectively the spin-flip and non-spin-flip matrix elements squared for free-nucleon photoproduction. The coefficients A(p, q) and B(p, q) include the effects of the deuteron internal momentum distribution and of the final-state nucleon-nucleon interaction, excluding the Coulomb interaction. Here,

$$p \equiv \left| \frac{\vec{p}_1 - \vec{p}_2}{2} \right| \quad \text{and} \quad q \equiv \left| \frac{\vec{p}_1 + \vec{p}_2}{2} \right| \quad \text{are the parameters}$$

chosen by Baldin to characterize the state of the recoiling nucleons. The vectors $\vec{p}_1$ and $\vec{p}_2$ are the nucleon (lab) momenta. By charge symmetry, Eq. (43) holds for both positive- and negative-meson production, if the appropriate matrix elements are inserted, and the final-state Coulomb interaction in negative-photopion production is ignored.

To take into account the additional proton-proton Coulomb interaction in negative-pion production, Baldin employed exact Coulomb final-state wave functions to calculate coefficients $A^c(p, q)$ and $B^c(p, q)$ to replace those in Eq. (43). Since we have $A(p, q) \gg B(p, q)$ in the ranges of p and q which concern us, it is the difference between $A(p, q)$ and $A^c(p, q)$ that chiefly determines the correction to be made to the data. Values of $A^c(p, q)$ are lower than those of $A(p, q)$ because of the Coulomb repulsion of the protons.

To facilitate making the proton-proton Coulomb correction, values of p and q had been derived for each observed event and were included in the IBM 650 printout. Values of $A(p, q)$ and $A^c(p, q)$ were interpolated from Tables I and II from Baldin,[34] and each event was individually weighted in the ratio A/A^c. The corrected numbers N_{pp} due to this procedure are shown for each bin in Table VI, and the size of the correction is plotted in Figs. 32 through 35, as a function of lab photon energy for the combined bins of Table VII. The average correction was +5.49%.

b. The Pion-Proton Coulomb Correction (Negative)

The pion-proton correction depends strongly on the momentum and angle of the meson but varies little with photon energy. A convenient way to obtain a correction for each meson bin is by use of the formula derived by Baldin;[34] the number of negative pions in each bin is divided by the quantity

$$1 + \frac{2\pi e^2}{\left|\vec{p}_\pi - \vec{q}/M\right|}, \qquad (44)$$

where $\vec{p}_\pi$ is the pion momentum (lab), $\vec{q}$ is the vector mean of the proton momenta defined above, $e^2 = 1/137$, and M is the proton mass ($\hbar = c = \mu = 1$). This correction is the same as the correction one would get from the interaction of the pion with a doubly charged particle moving with the same relative velocity as the protons' center of mass.

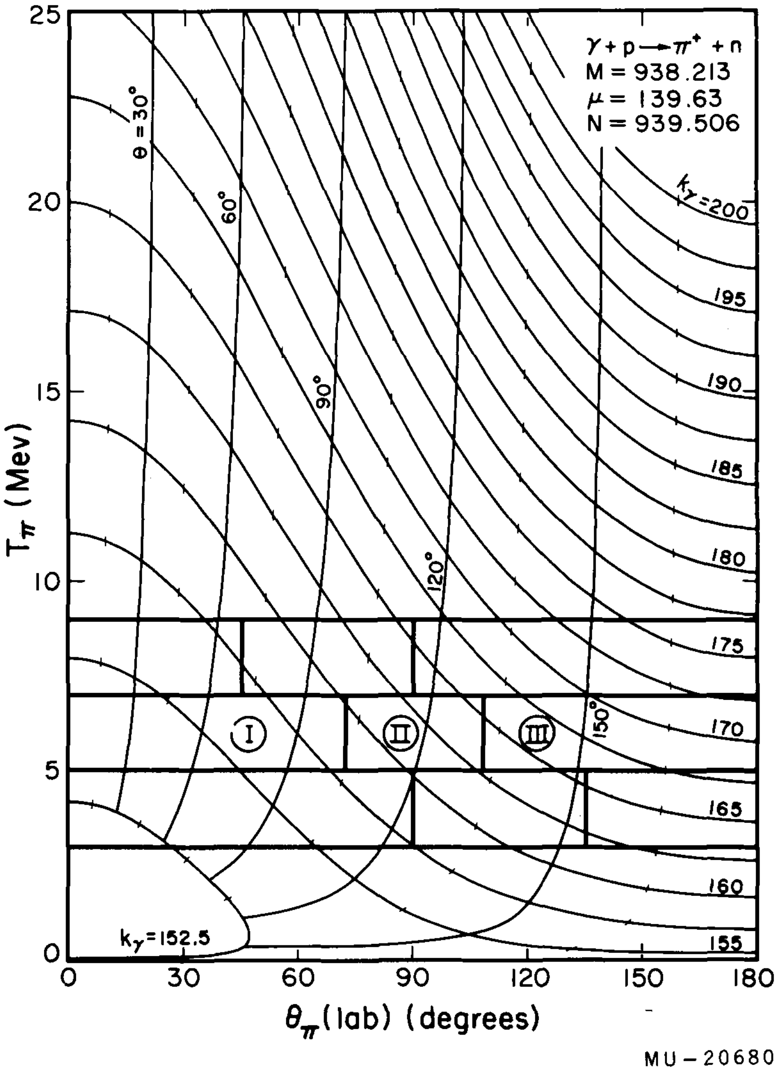

Fig. 32. Kinematics for the process $\gamma + p \rightarrow \pi^+ + n$. Curves for various photon energies (lab) and pion angles (c.m.) are shown. In obtaining the σ^-/σ^+ ratio, pions of kinetic energy T_π = 3 to 9 Mev were included. The data presented in Table VII and Figs. 33-35 are from events within the three bins I, II, and III.

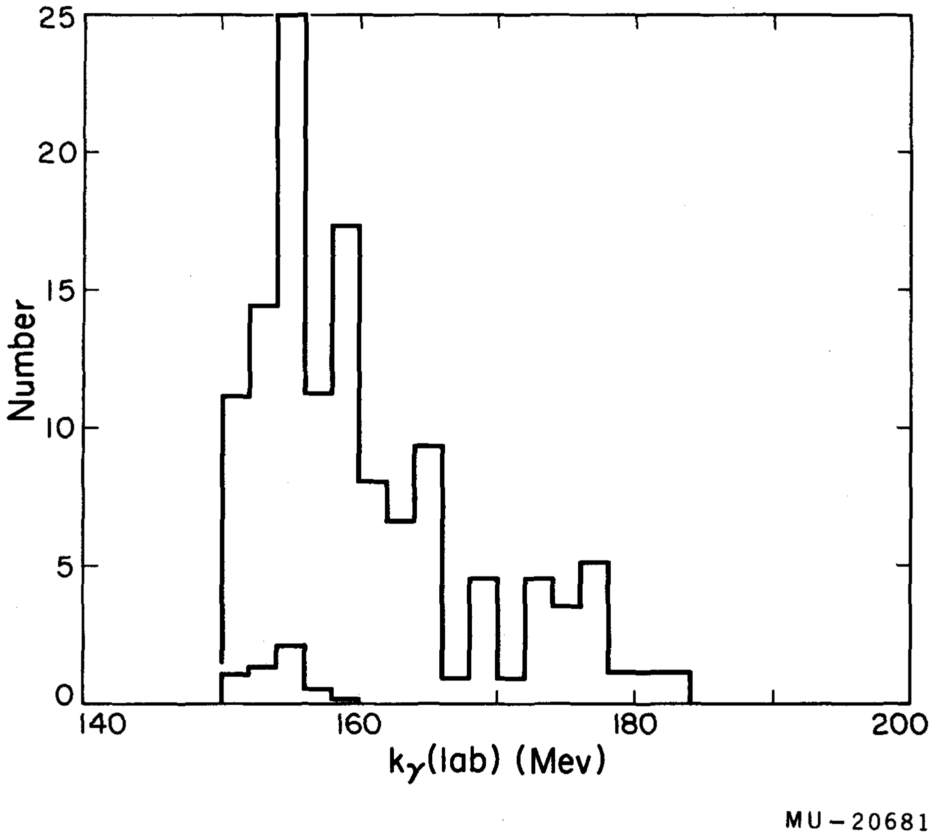

Fig. 33. Observed photon energy distribution for the mesons of bin I, Fig. 32 and Table VII.

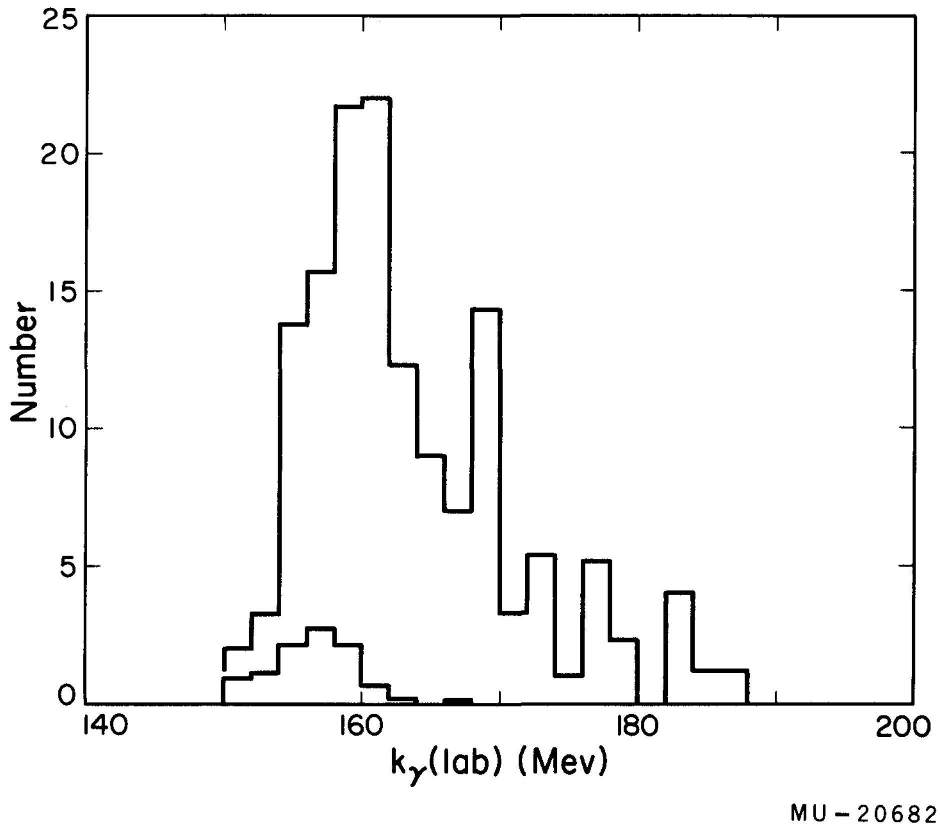

Fig. 34. Observed photon energy distribution for the mesons of bin II, Fig. 32 and Table VII.

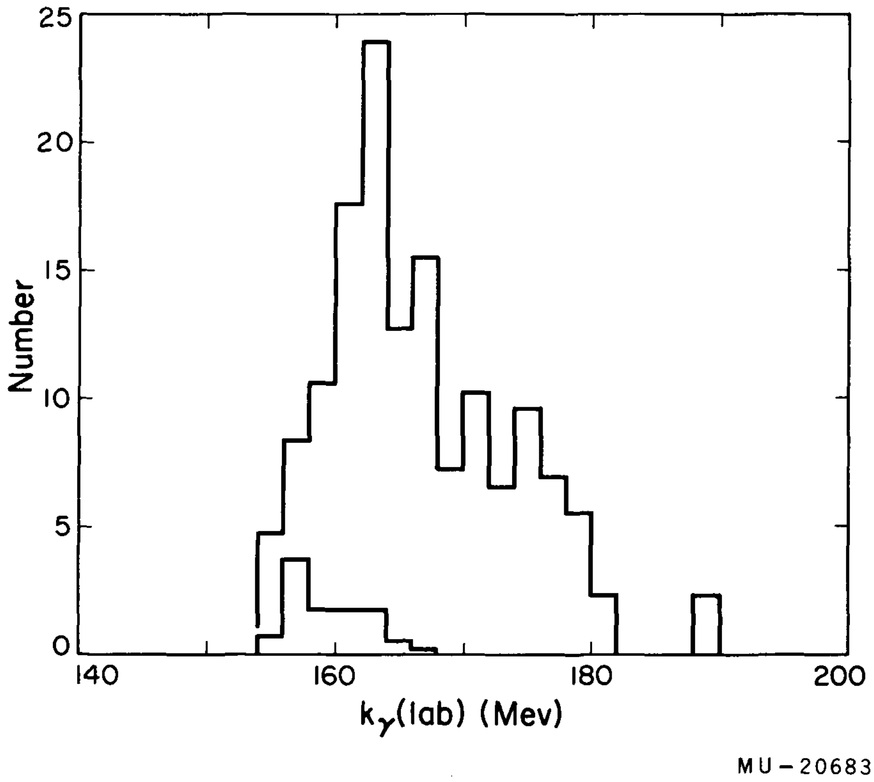

Fig. 35. Observed photon energy distribution for the mesons of bin III, Fig. 32 and Table VII.

The denominator in Eq. (44) was determined for the lab energy and angle of each meson by a simple graphical model. The corrected number $N_{\pi p}$ for each bin is indicated in Table VI. The average correction amounted to -14.6%.

After both the proton-proton and pion-proton Coulomb corrections had been applied, the net number of negative pions became 433 ± 29; the average net Coulomb correction amounted to -8.6%.

7. The Experimental σ^-/σ^+ Ratios

Before Coulomb corrections were applied, the observed over-all ratio was

$$\frac{\sigma^-}{\sigma^+} = \frac{471 \pm 31}{342 \pm 33} = 1.38 \pm 0.12 .$$

After Coulomb corrections were applied, the over-all ratio was

$$\frac{\sigma^-}{\sigma^+} = \frac{433 \pm 29}{342 \pm 33} = 1.27 \pm 0.11.$$

The average laboratory-system kinetic energy and angle of the observed mesons--6.15 Mev and 90 deg--correspond to the laboratory-system photon energy--162 Mev--and pion angle--120 deg--in the two-body ($\gamma + p$) center of mass. Spectator photon energies (those given by two-body kinematics) range from 152 Mev at forward pion angles to 177 Mev in the backward direction, as may be seen on Fig. 32. (If the deuteron binding energy and the neutron-proton mass difference are taken into account, Fig. 32 fairly accurately describes the kinematics for the process $\gamma + d \rightarrow \pi^- + p + (p \text{ at rest})$, as well as for $\gamma + p \rightarrow \pi^+ + n$.)

In order to get information on the dependence of σ^-/σ^+ on photon energy, the bins of Tables V and VI have been combined into three larger bins, roughly dividing the data according to spectator photon energy, as shown by the heavy lines in Fig. 32. The results for these larger bins are presented in Table VII.

Table VII

σ^-/σ^+ as a function of photon energy and meson angle

Bins included †	Spectator photon energy ‡ (Mev)	θ^*, pion angle ‡ (c. m.) (deg)	σ^-/σ^+ Before Coulomb correction	σ^-/σ^+ After Coulomb correction
1. A, B, C 2. A, B, 3. A	152-158	0-90	1.22 ± 0.16	1.08 ± 0.14
1. D, E, 2. C, D 3. B, C	158-165	90-140	1.36 ± 0.19	1.27 ± 0.18
1. F 2. E, F 3. D, E, F	165-175	135-180	1.54 ± 0.21	1.44 ± 0.20

† Bins are defined in Tables V, VI.

‡ The spectator photon energy (lab) and angle θ^* (c.m.) are from the $\gamma + p \rightarrow \pi^+ + n$ two-body kinematics of Fig. 32.

8. Distribution of Contributing Photon Energies

To roughly check on the validity of the use of two-body kinematics in determining the average photon energy, the distribution in photon energy of the negative mesons accepted for the σ^-/σ^+ ratio was plotted for the three bins of Table VII.

As seen in Figs. 32, 33, and 34, the distributions are in fact peaked around the spectator energy in each case, but with a high-energy tail which makes an important contribution.

The (positive) proton-proton Coulomb correction has been made to these data, and the size of the correction is indicated by the smaller histogram beneath the peak. As expected, it is most important at low photon energies. The pion-proton Coulomb correction has not been applied to the data in Figs. 32, 33, and 34. It would have little effect on the relative shapes of the distributions.

B. Extrapolations to Free-Nucleon Cross Sections $\sigma(\gamma + n \rightarrow \pi^- + p)$

1. The Prescription

To obtain points suitable for extrapolation, the form taken from Eq. (7) was used:

$$\sigma(k, p^2, w^2) = \frac{4\pi k^2}{\Gamma^2} \frac{M_D}{M_p} \frac{(p^2 + a^2)^2}{(w^2 - M_N^2)} \frac{\partial^2 \sigma}{\partial p^2 \partial w^2} . \tag{45}$$

The essential constants are

$$\Gamma^2 = 3.11,$$
$$a^2 = 0.107,$$
$$M_D/M_p = 1.999,$$
$$M_N^2 = 45.27,$$

where $\hbar = c = \mu = 1$. Values for Γ^2 and a^2 (sec. I. D) are based on the deuteron constants,[88] B. E. = (2.226 ± 0.002 Mev) and r_{ot} = $(1.702 \pm 0.029)10^{-13}$cm.

The differential cross section is obtained from the data,

$$\frac{\partial^2 \sigma}{\partial p^2 \partial w^2} = \frac{A}{N_0 \rho t} \frac{N_e}{N(k)\Delta k \Delta p^2 \Delta w^2} , \tag{46}$$

where A = 2.015 AMU, deuteron mass,

$N_0 = 6.025\ 10^{-23}$, Avogadro's number,

ρ = 0.1307 gm cm^{-3}, deuterium density (Sec. IV. F),

t = 7.0 cm, target length,

N_e = Number of events in three-dimensional bin $\Delta k \Delta p^2 \Delta w^2$,

$N(k)\Delta k$ = Number of photons in interval Δk (Table III)

$\Delta p^2 \Delta w^2$ = Size of two-dimensional bin in p^2 and w^2 (Figs. 2, 36).

When the constants are inserted, Eq. (45) becomes

$$\sigma(p^2, w^2, k) = 3.029\ 10^{-26}\ \frac{(p^2 + 0.107)^2}{(w^2 - 45.27)}\ \frac{(k_{Mev})^2\ N_e}{N(k)\Delta k \Delta p^2 \Delta w^2}\ cm^2, \tag{47}$$

where p^2 and w^2 are in pion units, and k is in Mev.

2. Averaging over Photon Energies

Since the data for a given $\Delta p^2 \Delta w^2$ bin is produced by a spectrum of photon energies, some way of averaging over the spectrum is required. The averaging is complicated by the fact that some photon energies are capable of contributing events to only part of an entire bin $\Delta p^2 \Delta w^2$. The procedure used was to effectively assign a weight

$$wt = N(k)\ \Delta k\ \delta p^2\ \delta w^2 \tag{48}$$

to the contribution to a given $\Delta p^2 \Delta w^2$ bin from photons in the energy interval Δk. Here, $\delta p^2\ \delta w^2$ is the subarea of $\Delta p^2\ \Delta w^2$ within which the events may occur. These subareas are found by examining graphs such as Figs. 2 and 36.

This choice of weight can be made plausible in the following way: Assume the cross section $\frac{\partial^2 \sigma}{\partial p^2 \partial w^2}$ to be constant over the region $\Delta p^2 \Delta w^2$. (This assumption has already been made when data are averaged). In a greatly extended experiment, the number of counts observed in the subregion $\delta p^2 \delta w^2$ is expected to be proportional to the area $\delta p^2\ \delta w^2$ times the number of available photons $N(k)\ \Delta k$. Thus, the weight would be proportional to this product. That $\frac{\partial^2 \sigma}{\partial p^2 \sigma w^2}$ may vary with k is not important if the same photon energies are included for all p^2 bins at a given w^2. When the weights are normalized to unity and the contributions to G averaged over k, we obtain

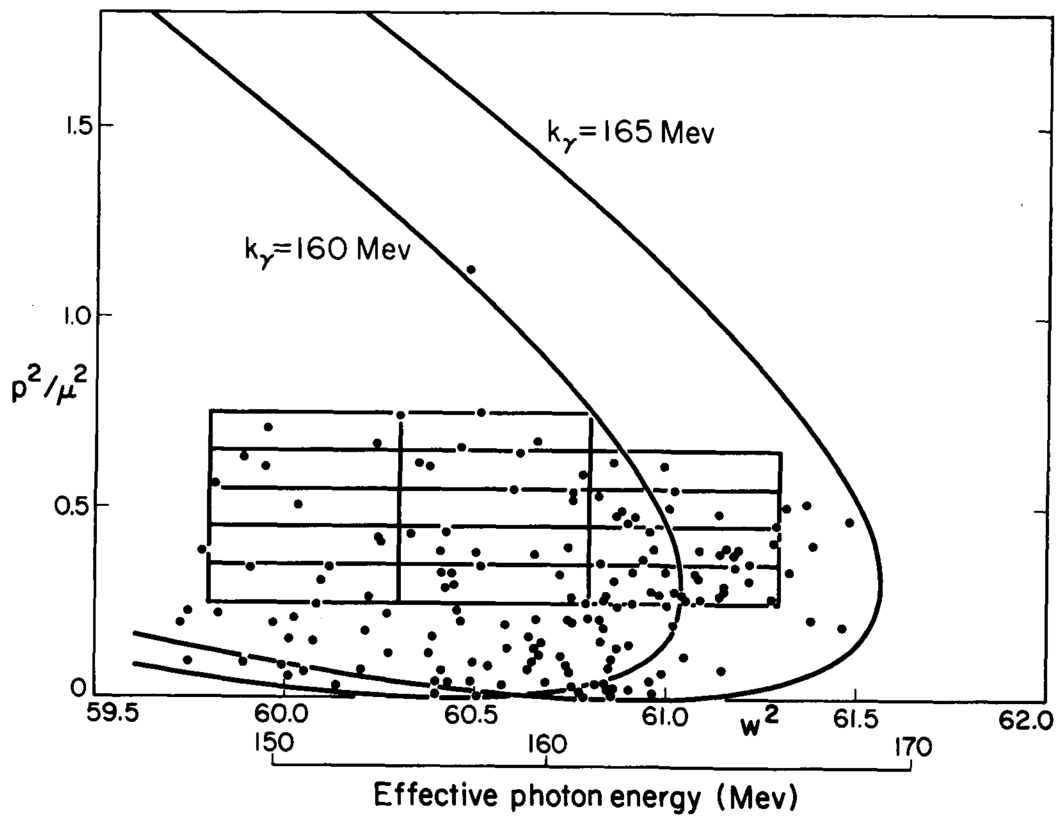

MU-20684

Fig. 36. Polology diagram in p^2 and w^2 (see Fig. 2). Here p^2 is the square of the momentum of the spectator proton, (lower lab kinetic energy) and w^2 is the total internal energy of the remaining $\pi^- + p$ system ($\hbar = c = \mu = 1$). The curves are kinematical boundaries in p^2 and w^2 within which events of the corresponding photon energy must fall. The rectangular bins are those used in obtaining the points in Figs. 37 - 41. Event of photon energy (lab) h = 160 to 165 Mev one plotted here.

$$\sigma(p^2, w^2) = 3.029\ 10^{-26}\ \frac{(p^2 + 0.107)^2}{(w^2 - 45.27)} \left\{ \frac{\Sigma (k_{Mev})^2\ N_e}{\Sigma N(k) \Delta k \delta p^2 \delta w^2} \right\} \mathrm{cm}^2. \tag{49}$$

Evaluation of the numerator was facilitated by first plotting the events in photon energy bins 5 Mev wide, extending from $k = 150$ to $k = 180$ Mev, as illustrated in Fig. 36. The data in each photon interval were restricted to those events occurring in the chamber between definite z_0 boundaries, depending on the photon energies included. Events in each photon energy interval were weighted to account for events occurring elsewhere in the 7.0-cm chamber path length used. Weights varied from 1.0 to 1.4. The method of assigning z_0 limits was discussed in Sec. VI. A.

The weighted number of events per $\Delta p^2 \Delta w^2$ bin in each photon energy interval Δk was multiplied by the square of the central photon energy. The numerator in Eq. (49) was formed from the sum of these products.

In the photon energy intervals in which the area $\Delta p^2 \Delta w^2$ lay entirely within the allowed region for all photon energies (e. g., the bins at $w^2 = 60.05$, Fig. 36), contributions to the denominator for a given $\Delta p^2 \Delta w^2$ bin were obtained in a straightforward way by multiplying the number of photons by the bin area. However, for photon energies whose $p^2 - w^2$ boundary curves crossed the $\Delta p^2 \Delta w^2$ bin (e. g., $w^2 = 61.05$, Fig. 36), a numerical integration had to be performed by dividing the bin into subareas $\delta p^2\ \delta w^2$ which fitted between the successive boundary curves in such a way that an average Δk for the subarea could be determined easily. N(k) was considered constant over the 5-Mev photon energy intervals.

As mentioned above, the use of photon energies for a given $\Delta p^2 \Delta w^2$ bin for which such an integration is required may lead to systematic errors, since the photon energy ranges averaged are not identical for all p^2 values at a constant w^2. For example, in Fig. 36

it is clear that photon of energy $k = 160$ to 180 Mev contribute to the bin centered at $w^2 = 61.05$, $p^2 = 0.3$, whereas only photons of energy $k = 161$ to 180 Mev contribute to the bin centered at $w^2 = 61.05$, $p^2 = 0.9$. However, the error introduced should be small, if σ varies slowly with k.

3. Experimental Points and Extrapolations

Experimental values of σ are presented as a functions of p^2 and w^2 in Figs. 37 - 41. The errors on each point are statistical only. Only data in the region $p^2 \geq 0.3$ are used. Events at the higher photon energies with recoil protons of energy $p^2 < 0.3$ ($R < 0.1$ cm) are generally unanalyzable because the spectator proton is invisibly short, and another track leaves the chamber.

The fact that the form of the extrapolating curve is not known puts us at a disadvantage. However, since the p^2 region that concerns us is far from any singularity in σ, we expect a simple behavior in the extrapolating curve. Three different polynomials were fitted to the data: a weighted average (zero-order) a straight line (first-order), and a parabola (second-order). These results are summarized in Table VIII.

Although the data are a bit ambiguous, a line seems preferable to the mean or the parabola. At the three lower photon energies (153.4, 158.6, and 163.7 Mev, Figs. 37-39) the straight-line fit gives a lower value of χ^2/M than the other fits, as may be seen in Table IX. The Fisher F test[89, 90] gives the weighted average only a small probability of being a correct fit to the data ($\approx 5\%$ for $k=163.7$ Mev, Fig. 39, and smaller for the lower photon energies). In addition the Fisher test indicates that the probability is 65% or greater that the highest-order coefficient for the parabolic fit can be zero for these three extrapolations. Thus a straight-line fit is indicated by both these criteria.

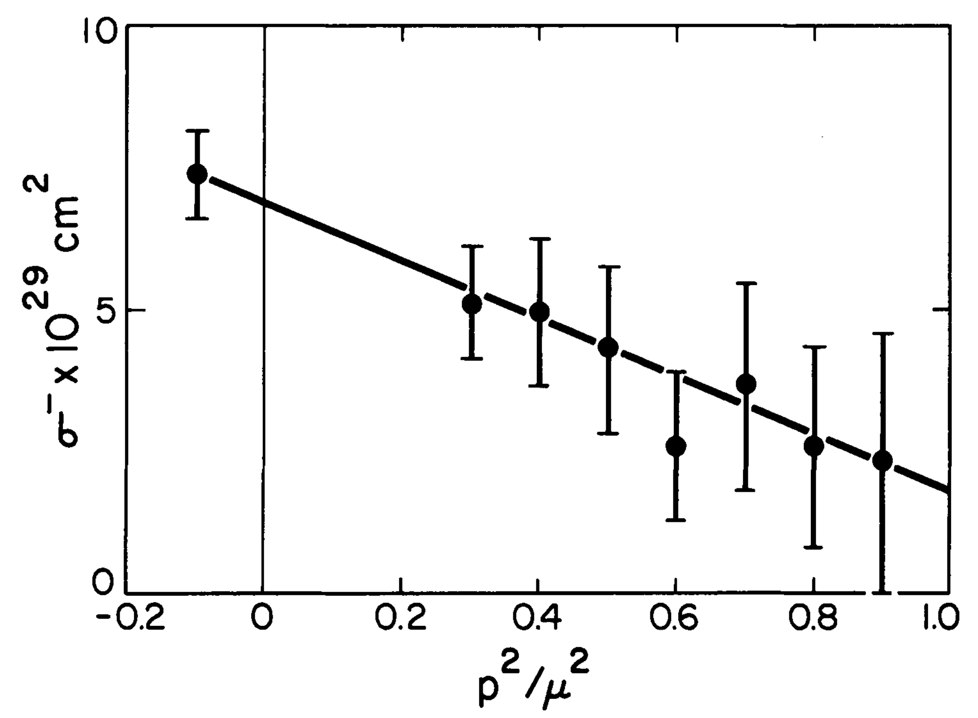

MU-20685

Fig. 37. Pology extrapolation for $w^2 = 60.05$ (k_{eff} (lab) = 153.4 Mev). The data in the interval $0.3 \leq p^2 \leq 0.9$ are extrapolated by means of a straight line to the nonphysical value $p^2 = -0.107$. At the extrapolated point, we obtain $\overline{G}(w^2) = \sigma(\gamma + n \rightarrow \pi^- + p)$.

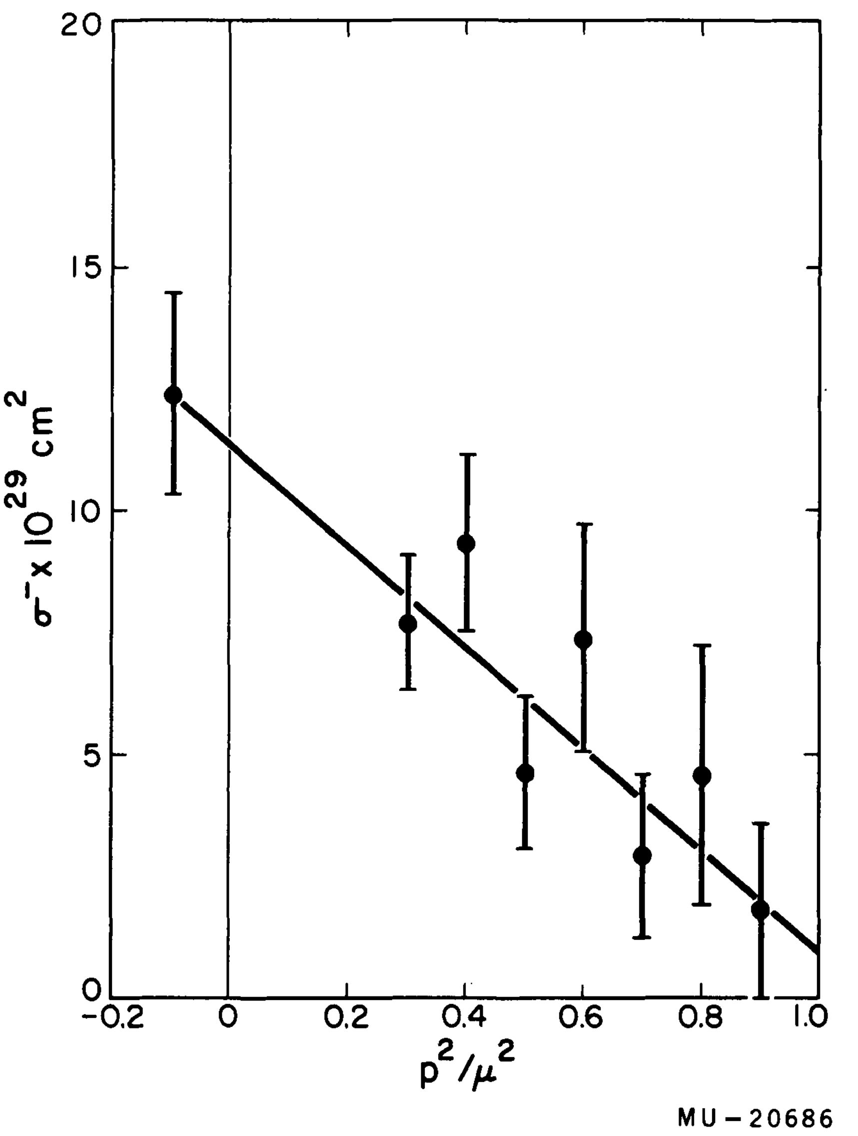

Fig. 38. Pololgy extrapolation for $w^2 = 60.55$ (k_{eff}(lab) = 158.6 Mev). The data in the interval $0.3 \leq p^2 \leq 0.9$ are extrapolated by means of a straight line to the nonphysical value $p^2 = -0.107$. At the extrapolated point, we obtain $\bar{G}^-(w^2) = \sigma(\gamma + n \rightarrow \pi^- + p)$.

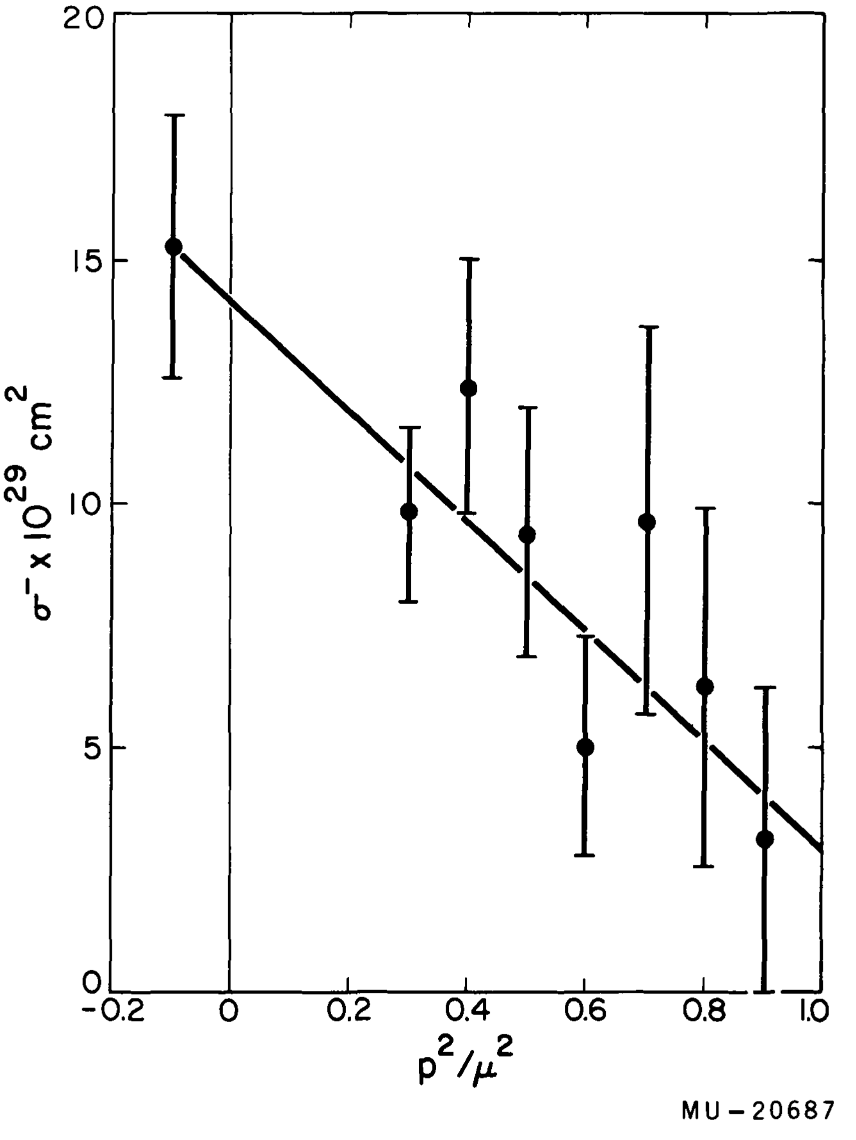

Fig. 39. Polology extrapolation for $w^2 = 61.05$ (k_{eff}(lab) = 163.7 Mev). The data in the interval $0.3 < p^2 < 0.9$ are extrapolated by means of a straight line to the nonphysical value $p^2 = -0.107$. At the extrapolated point, we obtain $\bar{G}(w^2) = \sigma(\gamma + n \rightarrow \pi^- + p)$.

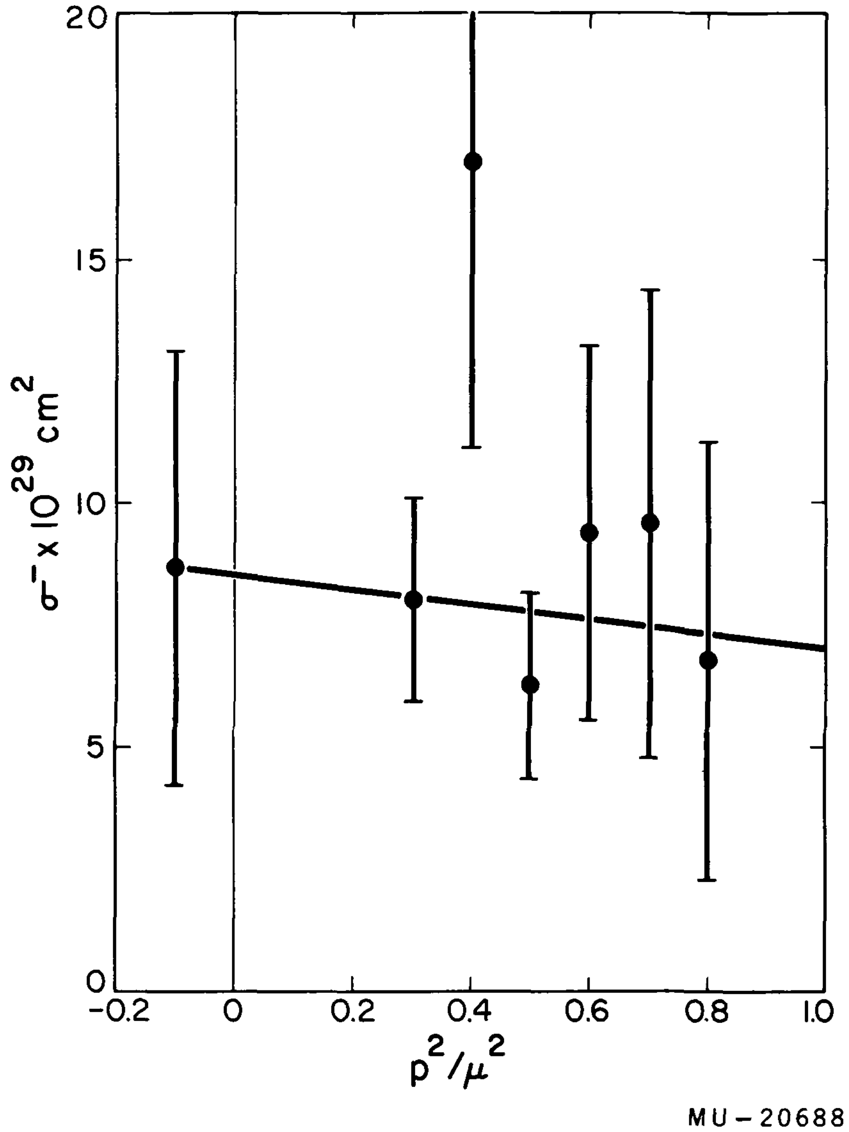

Fig. 40. Polology extrapolation for $w^2 = 61.55$ (k_{eff}(lab) = 168.9 Mev). The data in the interval $0.3 \leq p^2 \leq 0.9$ are extrapolated by means of a straight line to the nonphysical value $p^2 = -0.107$. At the extrapolated point, we obtain $\overline{G}\ (w^2) = \sigma(\gamma + n \rightarrow \pi^- + p)$.

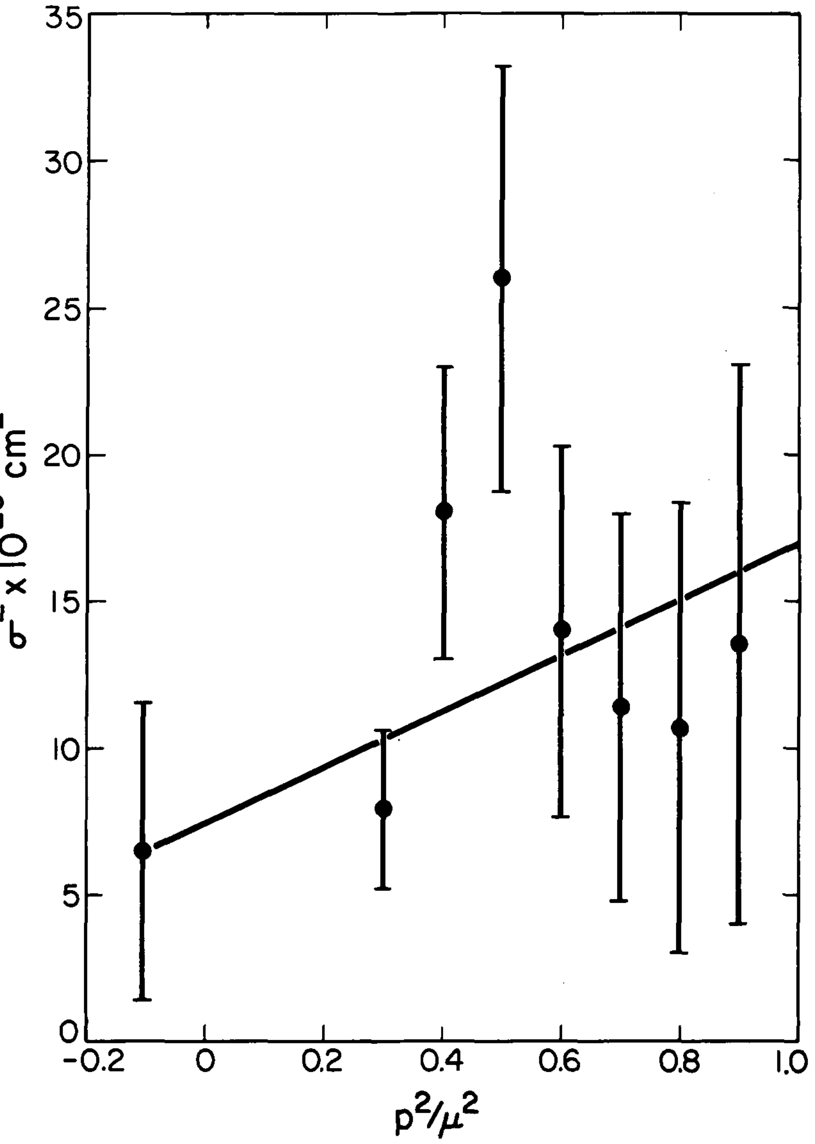

MU-20689

Fig. 41. Polology extrapolation for $w^2 = 62.05(k_{eff}$(lab) $= 174.1$ Mev). The data in the interval $0.3 \leq p^2 \leq 0.9$ are extrapolated by means of a straight line to the nonphysical value $p^2 = - 0.107$. At the extrapolated point, we obtain $\overline{G}\ (w^2) =$. $\sigma(\gamma + n \rightarrow \pi^- + p)$.

Table VIII

$\sigma(\gamma + n \rightarrow \pi^- + 2p)$ extrapolations

Extrapolation polynomial		Photon energy (lab) (Mev)				
		153.4 ($w^2 = 60.05$)	158.6 ($w^2 = 60.55$)	163.7 ($w^2 = 61.05$)	168.9 ($w^2 = 61.55$)	174.1 ($w^2 = 62.05$)
	N^*	7	7	7	6	7
One-	M	6	6	6	5	6
parameter	χ^2/M	0.73	2.46	1.45	0.70	1.19
	S_m	-	-	-	-	-
(Weighted average)	$\sigma:10^{29}, cm^2$	4.05±0.45	5.53±1.04	8.34±1.16	7.80±1.00	11.83±2.07
	N	7	7	7	6	7
Two-	M	5	5	5	4	5
parameter	χ^2/m	0.16	0.86	0.72	0.86	1.26
	S_m	22.64	12.21	7.17	0.04	0.66
(Line)	$\sigma:10^{29}, cm^2$	7.33±0.72	12.38±2.06	15.23±2.70	8.67±4.45	6.73±6.66

Table VIII (continued)

Extrapolation polynomial		Photon energy (lab) (Mev) 153.4 ($w^2 = 60.05$)	158.6 ($w^2 = 60.55$)	163.7 ($w^2 = 61.05$)	168.9 ($w^2 = 61.55$)	174.1 ($w^2 = 62.05$)
	N	7	7	7	6	7
Three-	M	4	4	4	3	4
parameter	χ^2/M	0.19	1.07	0.87	1.13	0.86
	S_m	0.31	0	0.11	0.04	3.33
(Parabola)	$\sigma \cdot 10^{29}$, cm^2	8.91±2.93	12.18±8.58	11.74±10.85	12.42±18.55	35.84±23.96

*N = number of points to be fitted

M = number of degrees of freedom

$S_{\overline{m}}$ = parameter for Fisher F test (Ref. 89)

σ = extrapolated cross section $\sigma(\gamma + n \rightarrow \pi^- + p)$

The two higher-energy extrapolations (168.9 Mev and 174.1 Mev, Figs. 40 and 41) are less clear, one (168.9 Mev) being better fitted by a weighted average, and the other (174.1 Mev) by a parabola.

Somewhat arbitrarily, the straight line was chosen to correlate the data at all five photon energies. As Table VIII shows, the errors on the extrapolated points depend strongly on the extrapolation form, and those associated with the straight-line extrapolation perhaps should not be taken at face value. Since the actual errors cannot be easily estimated, those based on the straight-line extrapolation are used for purposes of comparison with other data.

4. <u>The Cross Sections $\sigma^-(\gamma + n \rightarrow \pi^- + p)$</u>

The cross sections σ^- $(\gamma + n \rightarrow \pi^- + n)$ based on straight-line extrapolations are plotted as a function of photon energy in Fig. 42. This cross section may be expressed in terms of the expansion[8]

$$\frac{\partial \sigma^-}{\partial \Omega} = \left[a^-_0 + a_1^- \cos\theta^* + a^-_2 \cos^2\theta^*\right] W, \tag{50}$$

where

$$W = \frac{q\omega}{(1 + \nu/M)^2}, \tag{51}$$

and θ^* is the pion angle q is the pion momentum, ω is the pion total energy, ν is the photon energy, all in the center-of-mass system, and M is the nucleon mass ($\hbar = c = \mu = 1$). If S-wave production predominates, a^-_1 and a^-_2 are small, and

$$a^-_0 \approx \frac{\sigma(\gamma + n \rightarrow \pi^- + p)}{4\pi W}. \tag{52}$$

Values of a^-_0 determined in this way are presented in Fig. 43. The lower curve in this figure is taken from a preprint of Hamilton and Woolcock,[39] and represents the dispersion relations of

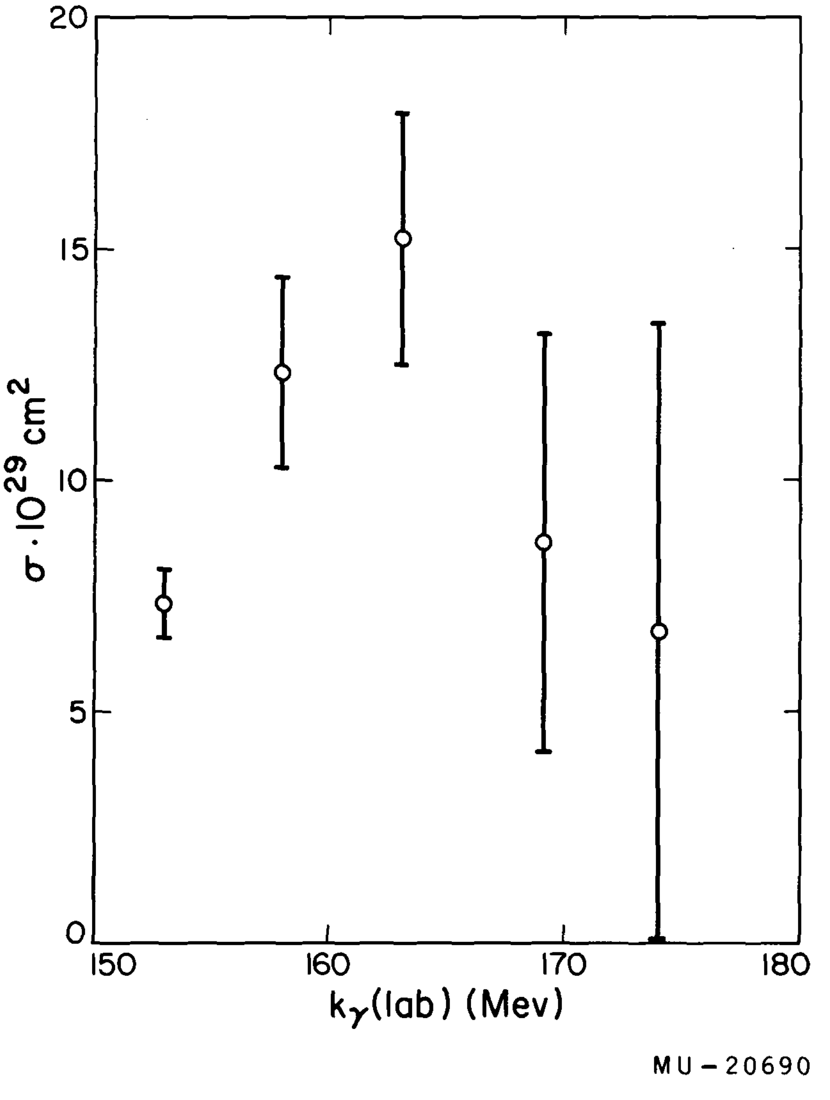

Fig. 42. Free-nucleon cross sections $\sigma(\gamma = n \rightarrow \pi^- + p)$ obtained by the straight-line extrapolations of Figs. 37 - 41.

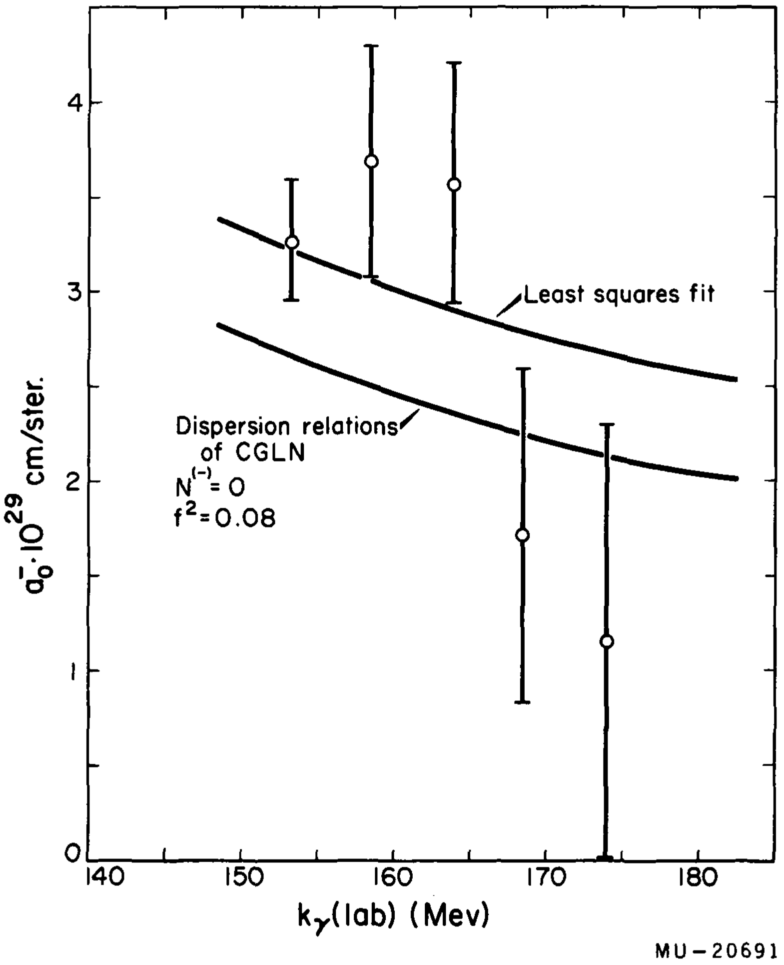

Fig. 43. Values of a^-_0 obtained by dividing the extrapolated cross sections of Fig. 42 or Table IX by the phase-space factor, $4\pi W$. The lower curve is based on the dispersion relations of Chew et al., and is taken from the paper of Hamilton and Woolcock. The upper curve differs from the lower one by an additive constant.

et al.,[20] assuming the term $N^{(-)}$ in the electric dipole amplitude to be zero, and $f^2 = 0.08$. The upper curve was obtained by a least-squares fit to the form

$$a^-_0 = \left[CGLN\ (f^2 = 0.08,\ N^{(-)} = 0\right] + C, \tag{53}$$

where CGLN refers to the dispersion relations prediction. The constant C was analyzed to be $(0.54\pm0.24)\ 10^{-29}\ \text{cm}^2$.

When the extrapolated data, as correlated by Eq. (53), were compared with data[38] for the reaction $(\gamma + p \rightarrow \pi^+ + n)$, the average ratio $\sigma^-/\sigma^+ - 1.7 \pm 0.2$ was obtained in the lab photon-energy region from threshold to 175 Mev.

C. Absolute Cross Sections $(\gamma + d \rightarrow \pi^- + 2p)$.

1. Total Cross Sections

Absolute cross sections were obtained for the process $(\gamma + d \rightarrow \pi^- + 2p)$ in a limited photon energy range $k = 150$ to 157.5 Mev. This range was chosen because, for $k < 150$ Mev, too few events were found to make such a cross section statistically meaningful. Above $k = 157.5$ Mev, the reactions had sufficient total energy that events with one invisibly short proton were frequently unanalyzable because the pion had a range long enough to leave the chamber. Since the cross section is expected to vary rapidly near threshold ($k_T = 145.83$ Mev), three bins, each 2.5 Mev wide, were chosen within this energy range.

Events were limited to those occurring within a definite 7-cm region in the bubble chamber defined by z_0 limits. A total of 70 two-prong "88" events was corrected to 78.7 by the Monte Carlo chamber geometry weighting procedure (Sec. V. J). An additional 63 three-prong events (mostly of the "888" type) were added, to give a total of 141.7 events. The 5.65% correction for scanning efficiency, difficulty in measurement, and charge exchange discussed in Subsection VI. A. 5 brought the total to 149.7 events.

The total cross sections were obtained by means of the formula

$$\sigma_t(\gamma + d \rightarrow \pi^- + 2p) = \frac{N_e}{\frac{N_0 \rho t}{A} N(k)\,\Delta k} . \tag{54}$$

The notation is that of Sec. VI. B. 1, and $N(k)\,\Delta k$ values are given in Table III. The total cross sections thus obtained are presented in Table IX and Fig. 44. As may be seen in Fig. 44, the data from this work are about 32% below the interpolated results of Adamovich et al.[13]

Table IX

Total cross section, $\sigma_t(\gamma+d\rightarrow\pi^-+2p)$			
Photon energy (lab) (Mev)	150-152.5	152.5-155	155-157.5
$\sigma_t \cdot 10^{29}\ \mathrm{cm}^2$	1.06±0.20	1.91±0.27	2.72±0.35

2. Angular Distribution in the (γ + d) Center of Mass

For sufficient statistics in making an angular distribution,all data used for the total cross sections in Subsection 1 were combined. Differential cross sections were obtained from the formula

$$\frac{\partial \sigma}{\partial \Omega} = \frac{N_e}{\frac{N_0 \rho t}{A} N(k)\,\Delta k\,\Omega} , \tag{55}$$

where the notation is the same as in Eq. (54) and Ω is the solid angle in steradians, in the γ + d c.m. frame. Results are plotted in Fig. 45 and tabulated in Table X.

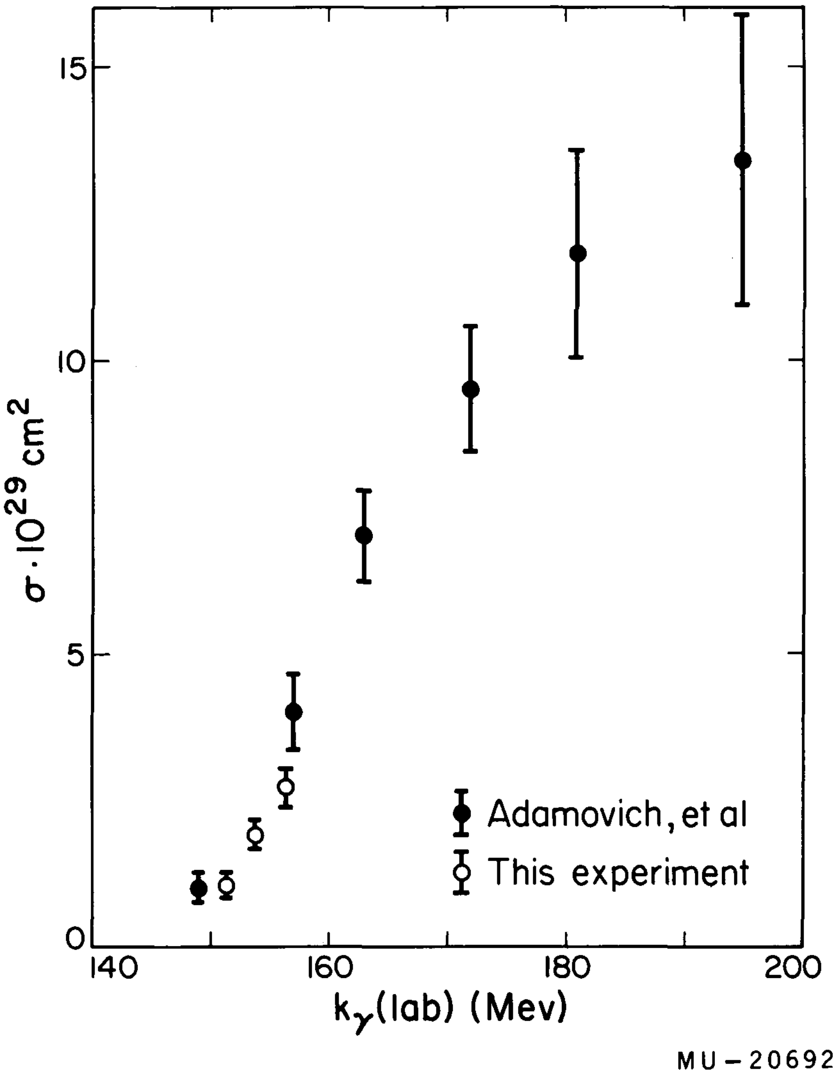

Fig. 44. Total cross section for the process $\gamma + d \rightarrow \pi^- + 2p$ as a function of lab photon energy.

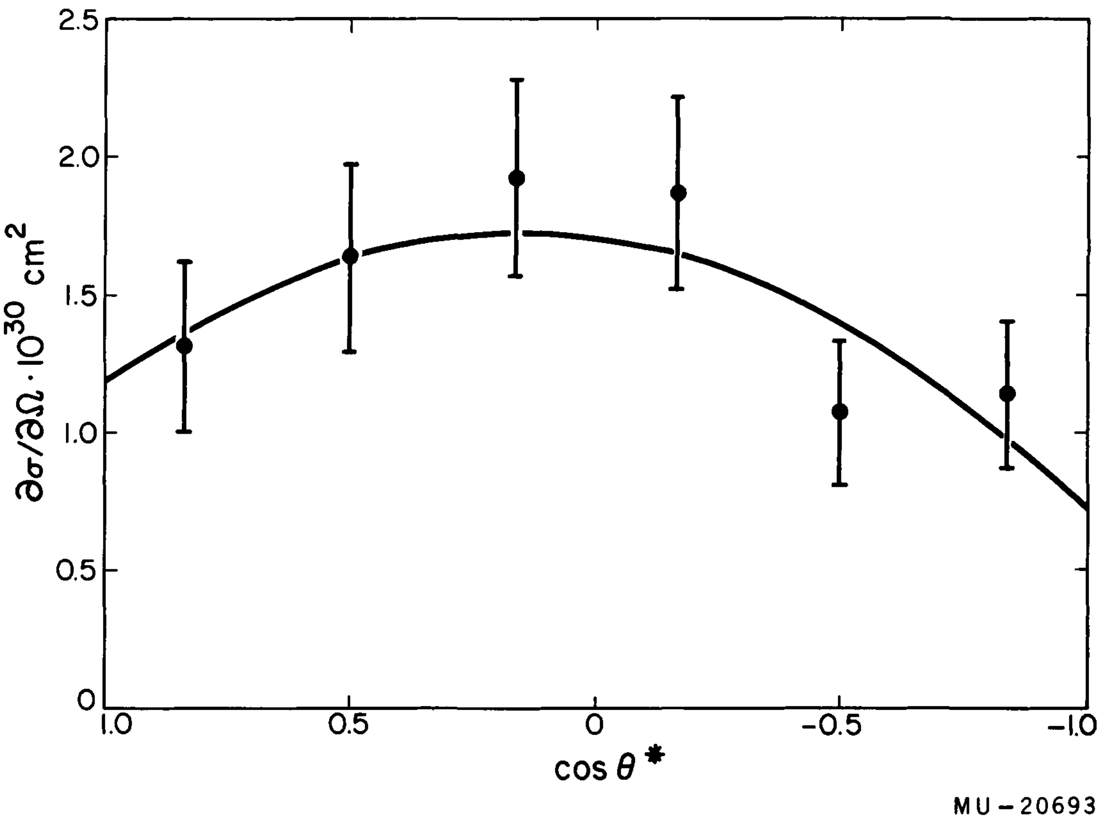

Fig. 45. Pion angular distribution in the $\gamma + d$ c.m. frame for the process $\gamma + d \rightarrow \pi^- + 2p$ at lab photon energy k = 150 to 157.5 Mev. The curve is a least-squares fit to a second-order polynomial in cos θ^*.

Table X

Differential cross sections for the process $\gamma + d \rightarrow \pi^- + 2p$ at laboratory photon energy k = 150 to 157.5 Mev

†$\cos\,\theta^*$	0.83	0.50	0.17	-0.17	-0.50	-0.83
$\frac{\partial\sigma}{\partial\Omega} \cdot 10^{30}\ \frac{cm^2}{sr}$	1.31	1.63	1.92	1.87	1.07	1.14
	±0.31	±0.34	±0.36	±0.35	±0.26	±0.27

†$\cos\,\theta^*$ is measured in the $\gamma + d$ c. m. frame

As shown in Fig. 45, the data were fitted to an assumed isotropic distrubiton and also to a second-order curve of the form

$$\frac{\partial\sigma}{\partial\Omega} = A_0 + A_1 \cos\,\theta^* + A_2 \cos^2\theta^* . \tag{56}$$

These results are summarized in Table XI .

Table XI

Coefficients in the angular distribution of Fig. 45

Type of fit	M	χ^2	A_0	A_1	A_2
Isotropic distribution	5	6.94	1.41±0.15	--	--
Second order in $\cos\,\theta^*$	3	2.65	1.71±0.20	0.23±0.20	-0.76±0.42

M = number of degrees of freedom.

As can be judged from the χ^2 test, the second-order form is preferable (40% probability that a random sample gives no better fit), but the isotropic distribution is not ruled out (30% probability that a random sample gives no better fit). This may be compared with the work of Adamovich,[14] who obtained a very good fit to an isotropic distribution.

Predicted angular distributions for various combinations of nucleon final states with meson S and P final states are tabulated by Adamovich.[14] According to these predicted angular distributions, a negative $\cos^2 \theta^*$ term implies a $^3P_1$ nucleon final state and a P meson final state with electric dipole absorption of the photon. Although the direct interaction term[54] mixes in higher meson angular momentum states and the deuteron structure may introduce anisotropy, S-wave photopion production is expected to predominate this close to threshold.

VII. CONCLUSIONS

A. The Observed Ratio σ^-/σ^+

The dependence of the ratio σ^-/σ^+ on photon energy and pion angle can be seen most readily in Fig. 46, on which the final data of Table VII are plotted with those of other workers. Coulomb corrections based on Baldin's work[34] have been applied to all points by this author, except where stated otherwise , two-body kinematics (Fig. 32) is assumed. The curves in Fig. 46 are the predictions of the dispersion relations of Chew et al.[20] as calculated in the paper by Beneventano et al.[*10]

The data in this work show an upward trend with increasing photon energy and c.m. angle. This undoubtedly is due in part to the angular dependence of σ^-/σ^+, which is predicted by the dispersion relations. (See Sec. I. A.).

Of the data presented here, the two points at higher energy are in agreement both with theory and with previous work. The single point at photon energy k = 155 Mev is lower than expected. This may reflect the influence of the photon—three-pion interaction[24] mentioned in Sec. I. A. If so, this point would correspond to a value Λ on σ^-/σ^+ is not strongly energy-dependent.

Generally, the data presented here are in agreement with previous results, and except for the low point just discussed, tend to confirm the consistency which seems at this time to exist among the low-energy pion parameters (Sec. I. B).[90]

The peaking of the true event energy around the photon energy given by two-body kinematics (Figs. 33-35) is in qualitative agreement with the calculations of Beneventano et al.[10] Because of this peaking, the use of two-body kinematics to determine the photon energy and pion c.m. angle can be considered a satisfactory method.

*That the curves of Fig. 46 extrapolate to a threshold value **R** = 1.36 rather than 1.30 or lower may be due to the neglect of a $(1+\omega/M)^{-1}$ term in the expression for $\mathcal{F}^{(0)}$ taken from Reference 20.

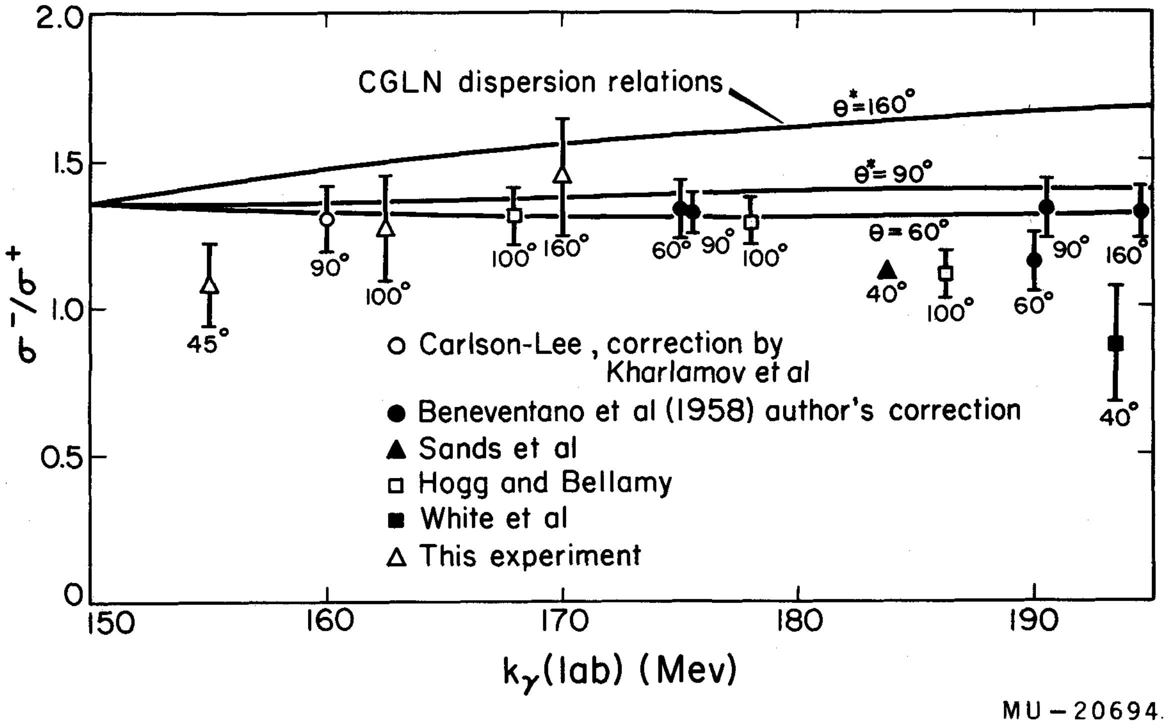

Fig. 46. The observed ratios σ^-/σ^+ corrected for final-state Coulomb effects compared with the predictions of the dispersion relations of Chew et al. for various c. m. angles. The curves are from the paper of Beneventano et al. Two-body kinematics is used to determine the photon energy (lab) and angle (c. m.) except where noted, the Coulomb corrections were made by this author.

B. Extrapolations to Cross Sections ($\gamma + n \rightarrow \pi^- + p$)

Cross sections for the reaction $\gamma + n \rightarrow \pi^- + p$ were obtained by using straight-line extrapolations of data from the reaction $\gamma + d \rightarrow \pi^- + 2p$ to a negative (nonphysical) value of the kinetic energy of the lower-energy proton. These results, when compared with other workers' cross sections for the reaction $\gamma + p \rightarrow \pi^+ + n$, gave a ratio $\sigma^-/\sigma^+ = 1.7 \pm 0.2$ near threshold. The data obtained by this method are not definitive in themselves. However, as a first attempt at the Chew-Low polology extrapolation procedure, they serve as a valuable illustration of the technique. The difficulty of this method is as apparent here as is the inherent feasibility. More data will improve the situation. Even more valuable than an extension of this experiment would be a similar experiment with a larger bubble chamber. In a larger chamber, events at higher photon energy with spectator protons of very low energy would generally be analyzable, since the pion has a greater chance of stopping within the chamber volume. The extrapolations would then be improved by data closer to the point to which the extrapolations are made.

C. Absolute Cross Sections

The absolute cross sections obtained in Sec. VI. C are surprisingly different from those interpolated from the data of Adamovich et al.[13, 14] The total cross sections are about 32% lower than the Russian data, and the differential cross sections, although consistent with isotropy, contain a strong suggestion of a negative $\cos^2\theta^*$ term in the $\gamma + d$ c.m. reference frame.

The discrepancy in the total cross section could conceivably be due to a number of causes:

(a) a statistical fluctuation,

(b) a bremsstrahlung monitoring error,

(c) poor estimation of scanning efficiency, or

(d) an error in event energy determination.

The monitoring arrangement at the Lebedev Physical Institute has never been directly intercalibrated with those of other laboratories, so that a systematic error could be found here. However, the ratio σ^-/σ^+ based on the negative photopion experiments of Adamovich et al. and on the positive photopion work at other laboratories,[39] is in agreement with the average ratio obtained in the present work. A monitoring error in this experiment could have occurred if we incorrectly assumed (Sec. III. E) that the average beam flux per bubble chamber pulse was the same as that per synchrotron pulse. It is difficult to imagine how this could have occurred. That the Chew-Low polology extrapolations were higher than expected is not consistent with this speculation.

An overestimation of scanning efficiency may affect this experiment. However, the double scanning procedure used throughout should have given a very high over-all efficiency. Events could have been missed because both protons had invisibly short tracks, but this can happen only at forward pion angles. If we assume that events missed for this reason are the cause of anisotropy as well as a low total cross section, we should expect more events lost at forward pion angles than at backward pion angles. This is not the case, judging from Fig. 45.

The event energy determination depends on the range-energy relationship and on the elementary-particle mass values. That this could be the source of the discrepancy seems very unlikely, so we are left with (a), (b), and (c) as causes about which to speculate.

Concerning the angular distribution, the suggested presence of a negative $\cos^2\theta^*$ term is an interesting new development. However, since the data are also consistent with isotropy, and in light of Adamovich's results, we should regard this development with some skepticism until further data are available.

ACKNOWLEDGMENTS

The author would like to express his sincere appreciation to Professor A. C. Helmholz for his continued encouragement and guidance throughout the course of this work.

Particular thanks are also due to Dr. Robert W. Kenney, who suggested this experiment and gave invaluable help and encouragement throughout, and to the other collaborating physicists, Dr. John D. Anderson, Mr. Duane C. Gates, and Dr. Thomas L. Jenkins, whose help and advice contributed to the successful performance of this work.

To Mr. Rudin M. Johnson and the synchrotron crew, we are indebted for many weeks of steady beam under unusual operating conditions.

Our appreciation goes to Mr. Richard I. Mitchell for his thorough work in programming the kinematics analysis.

Thanks are due to Professor Luis W. Alvarez for the use of the bubble chamber and scanning equipment. Mr. Arnold J. Schwemin and Mr. Douglas Parmentier, Jr., provided valuable help with the chamber in earlier runs, Mr. Clyde R. Brown modified the chamber for us, and Mr. Donald A. McPherson gave us much help operating the chamber.

Grateful acknowledgment goes to Miss Betty Blaine, Mr. Robert Brians, Dr. Graham Conroy, Mr. Lloyd Fisher, Mr. Gordon Hamilton, Mrs. Helen Schneider, and Mr. Charles Welsh for help in carrying out the arduous analysis, and to Miss Miriam Machlis for preparing the manuscript.

To Professor Geoffrey F. Chew and Dr. Michael J. Moravcsik we are grateful for several illuminating discussions of the results. We would also like to express our appreciation to the supporting groups of the Lawrence Radiation Laboratory whose efforts allowed this work to proceed smoothly to a conclusion, but whose members are too numerous to mention here.

This work was performed under the auspices of the U. S. Atomic Energy Commission.

REFERENCES

1. R. S. White, M. J. Jacobson, and A. G. Schulz, Phys. Rev. 88, 836 (1952).
2. M. Sands, J. G. Teasdale, and R. L. Walker, Phys. Rev. 95, 592 (1954).
3. M. Beneventano, G. Stoppini, D. Carlson-Lee, G. Bernardini, and E. L. Goldwasser, Nuovo cimento 12, 156 (1954).
4. D. Carlson-Lee, G. Stoppini, and L. Tau, Nuovo cimento 2, 162 (1955).
5. M. Beneventano, G. Stoppini, L. Tau, and G. Bernardini, Proceedings of the CERN Symposium on High Energy Accelerators and Pion Physics, Geneva, 1956, II, p. 259.
6. M. I. Adamovich, V. I. Veksler, G. V. Kuzmicheva, V. G. Larionova and S. P. Kharlamov, Proceedings of the CERN Symposium on High Energy Accelerators and Pion Physics Geneva, II, p. 265.
7. K. M. Watson, J. C. Keck, A. V. Tollestrup, and R. L. Walker, Phys. Rev. 101, 1159 (1956).
8. M. Beneventano, G. Bernardini, D. Carlson-Lee, G. Stoppini, and L. Tau, Nuovo cimento 4, 323 (1956).
9. M. J. Moravcsik, Nuovo cimento 7, 442 (1958). In this paper, Moravcsik critically examines the extrapolation to threshold of Ref. 7 and shows how it could be significantly altered with no change in assumptions.
10. M. Beneventano, G. Bernardini, G. Stoppini, and L. Tau, Nuovo cimento 10, 1109 (1958).
11. D. Carlson-Lee, Bull. Am. Phys. Soc., Ser. II, 3, 334 (1958). and private communication.
12. W. R. Hogg and E. H. Bellamy, Proc. Phys. Soc. 72, 895 (1958).
13. M. I. Adamovich, G. V. Kuzmicheva, V. G. Larionova, and S. P. Kharlamov, J. Exptl. Theoret. Phys. (U. S. S. R.) 35, 27 (1958). Translated in Soviet Phys. JETP 8, 21 (1959).

14. M. I. Adamovich, J. Exptl. Theoret. Phys. (U. S. S. R.), 35, 39 (1958). Translated in Soviet Phys. JETP 8, 29 (1959).

15. S. P. Kharlamov, M. I. Adamovich, and V. G. Larionova, J. Exptl. Theoret. Phys. (U. S. S. R.) 36, 945 (1959), translated in Soviet Phys. JETP 9, 668 (1959).

16. G. F. Chew and F. E. Low, Phys. Rev. 113, 1640 (1959).

17. K. A. Brueckner and M. L. Goldberger, Phys. Rev. 76, 1725 (1949).

18. K. A. Brueckner, Phys. Rev. 79, 641 (1950).

19. For summaries of the work at higher energies than k = 200 Mev, see M. J. Moravcsik, Phys. Rev. 105, 267 (1957); and G. Bernardini, "Pion Photoproduction and Compton Effect on Nucleons," 1959 Annual International Conference on High Energy Physics at Kiev (to be published).

20. G. F. Chew, M. L. Goldberger, F. E. Low, and Y. Nambu, Phys. Rev. 106, 1345 (1957) and G. F. Chew in, Encyclopedia of Physics (Springer Verlag, Berlin, in press).

21. M. J. Moravcsik, "Selected Topics in Low Energy Pion Physics," Brookhaven National Laboratory Report. BNL-459 (T-100), March 1957.

22. N. Kroll and M. Ruderman, Phys. Rev. 93, 233 (1954).

23. A. Klein, Phys. Rev. 99, 998 (1955).

24. J. S. Ball, "The Application of the Mandelstam Representation to Photoproduction of Ions from Nucleons" (Thesis), UCRL-9172, April 1960.

25. How-Sen Wong, Bull. Am. Phys. Soc. 4, Ser. II, 407 (1959).

26. H. L. Anderson and E. Fermi, Phys. Rev. 86, 794 (1952).

27. H. P. Noyes, Phys. Rev. 101, 320 (1956).

28. J. M. Cassels, Proceedings of the Seventh Annual Rochester Conference on High-Energy Physics, 1957 (Interscience Publishers, Inc., New York, 1957) II, 1.

29. G. Puppi, Proceedings of the 1958 Annual International Conference on High Energy Physics at CERN, 46-51 (1958).

30. M. J. Moravcsik, "The Low-Energy Parameters of Pion Physics," paper submitted to the Eighth Annual Rochester Conference on High Energy Physics, Geneva. The discussion in this section is based partly on Moravcsik's paper.

31. M. J. Moravcsik, Phys. Rev. 111, 1657 (1958).

32. J. Fischer, R. March, and L. Marshall, Phys. Rev. 109, 533 (1958).

33. A. M. Baldin, Proceedings of the CERN Symposium on High Energy Accelerators and Pion Physics 1956, II, p. 272.

34. A. M. Baldin, Nuovo cimento 8, 569 (1958).

35. A. M. Baldin and P. K. Kabir, Nuovo cimento 9, 547 (1958).

36. M. Cini, R. Gatto, E. K. Goldwasser, and M. Ruderman, Nuovo cimento 10, 243 (1958).

37. J. M. Cassels, Suppl. Nuovo cimento 14, 259 (1959).

38. G. Bernardini, "Pion Photoproduction and Compton Effect on Nucleons," 1959 Annual International Conference on High Energy Physics at Kiev (to be published).

39. J. Hamilton and W. S. Woolcock Phys. Rev. 118, 291 (1960).

40. W. K. H. Panofsky, R. L. Aamodt, and J. Hadley, Phys. Rev. 81, 565 (1951).

41. M. C. Rinehart, K. C. Rogers, and L. Lederman, Phys. Rev. 100, 883 (1955).

42. J. M. Cassels, G. Fidecaro, A. M. Wetherell, and J. R. Wormald, Proc. Phys. Soc. (London) A70, 405 (1957).

43. J. A. Kuehner, A. W. Merrison, and S. Tornabene, Proc. Phys. Soc. (London) 73, 545 (1959).

44. E. L. Koller and A. M. Sachs, Phys. Rev. 116, 760 (1959).

45. N. P. Samios, Bull. Am. Phys. Soc., Ser. II, 5, 71 (1960).

46. G. S. Janes and W. L. Kraushaar, Phys. Rev. 93, 900 (1954).

47. G. Bernardini and E. L. Goldwasser, Phys. Rev. 94, 729 (1954); Phys. Rev. 95, 857 (1954).

48. J. E. Leiss, C. S. Robinson, and S. Penner, Phys. Rev. 98, 201 (1955).

49. G. M. Lewis and R. E. Azuma, Proc. Phys. Soc. (London) 73, 873 (1959).

50. A. Barbaro, E. L. Goldwasser, and D. Carlson-Lee, Bull. Am. Phys. Soc. 4, 23 (1959).

51. M. Adamovich et al., results reported in Ref. 38.

52. J. E. Leiss, S. Penner, and C. S. Robinson, results reported in Ref. 38.

53. D. C. Gates, R. W. Kenney, D. A. McPherson, and W. P. Swanson (Lawrence Radiation Laboratory) (to be published).

54. M. J. Moravcsik, Phys. Rev. 104, 1451 (1956).

55. H. A. Bethe and F. de Hoffmann, Mesons and Fields (Row, Peterson, and Co. Evanston, Ill., 1955, Vol. II, 97.

56. J. Orear, Nuovo cimento 4, 856 (1956).

57. G. F. Chew and H. W. Lewis, Phys. Rev. 84, 779 (1951).

58. G. F. Chew and G. C. Wick, Phys. Rev. 85, 636 (1952).

59. G. F. Chew and M. L. Goldberger, Phys. Rev. 87, 778 (1952).

60. The Cornell 300-Mev Synchrotron, ONR Report, July, 1953.

61. H. C. Dittler and T. F. Gerecke, "Liquid Hydrogen Bubble Chambers" (M. S. Thesis), UCRL-2985, May 1955.

62. D. Parmentier, Jr., and A. J. Schwemin, Rev. Sci. Instr. 26, 954 (1955).

63. H. A. Bostick, "Spectrum and Yield of Neutrons from 31.5-Mev Proton Bombardment of Selected Isotopes of Cobalt and Nickel" (Thesis), UCRL-8528, Oct. 1958.

64. H. E. Adelson, "Energy Spectra and Angular Dependences of Neutrons from the 31.5-Mev Proton Bombardment of Beryllium-9, Nitrogen-14, and Aluminum-27" (Thesis), UCRL-8568, Dec. 1958.

65. H. E. Adelson, H. A. Bostick, B. J. Moyer, and C. N. Waddell, "Use of the Four-Inch Hydrogen Bubble Chamber as a Fast-Neutron Spectrometer" (UCRL-8604, Jan. 1959); Rev. Sci. Instr. 31, 1 (1960).

66. D. C. Gates, R. W. Kenney, D. A. McPherson, and W. P. Swanson, "Operation of Hydrogen Bubble Chambers in High-Energy Photon Beams" Rev. Sci. Instr. 31, 565 (1960).

67. J. D. Anderson, D. C. Gates, T. L. Jenkins, R. W. Kenney, C. A. McDonald, Jr., and W. P. Swanson, Proceedings of the Second United Nations International Conference on the Peaceful Uses of Atomic Energy, 30, 250 (1958); and D. C. Gates, et al., (Lawrence Radiation Laboratory) (to be published.)

68. W. I. Linlor, Q. A. Kerns, and J. W. Mark, Rev. Sci. Instr. 28, 535 (1957).

69. J. D. Anderson, R. W. Kenney, and C. A. McDonald, Jr., Phys. Rev. 102, 1626 (1956).

70. Gladys W. Grodstein, "X-Ray Attenuation Coefficients from 10 kev to 100 Mev," National Bureau of Standards-C-583, April 1957, p. 23-27.

71. W. Heitler, "The Quantum Theory of Radiation" (Oxford) University Press, Amen House, London, E. C. 4, 1954), 3rd ed., p. 221.

72. W. Heitler, op. cit., p. 260.

73. J. Joseph and F. Rohrlich, Revs. Modern Phys. 30, 367 (1958).

74. L. I. Schiff, Phys. Rev. 83, 252 (1951).

75. A. S. Penfold and J. E. Leiss, "Analysis of Photo Cross Sections," Physics Research Laboratory, University of Illinois, Champaign, Illinois, 1958.

76. F. J. Loeffler, T. R. Palfrey, and G. W. Tautfest, Nucl. Instr. and Methods, 5, 50 (1959).

77. J. W. DeWire, (Cornell University) "Calibration Data for the Quantameter and the Cornell Thick-Walled Ionization Chamber," private communication, Nov. 1959.

78. H. A. Bethe and F. de Hoffmann, Mesons and Fields (Row, Peterson, and Co., Evanston, Ill., 1955 Vol. II. Sec. 36c.

79. H. A. Bethe and F. de Hoffmann, op. cit. Sec. 36e.

80. E. A. Whalin, B. D. Schriever, and A. O. Hanson, Phys. Rev. 101, 377 (1956).

81. G. Clark and W. F. Diehl, "Range-Energy Relation for Liquid Hydrogen Bubble Chambers" UCRL-3789, May 1957, (M. S. Thesis, Navy).

82. L. Reed and R. Tripp, "Density of Hydrogen at Operation Conditions of 15-inch Bubble Chamber," UCRL Engineering Note 4320-01M2, Oct. 1958, give a 1.5% upward correction of Clark and Diehl's calculation of the density of hydrogen in the 10-in bubble chamber, due to a new calculation of the proton range-energy relationship (Ref. 83).

83. W. Whaling, Encyclopedia of Physics (Springer Verlag, Berlin, 1958), Vol. 34, p. 208.

84. W. A. Aron, "The Passage of Charged Particles through Matter" (Thesis), UCRL-1325, May 1951.

85. C. F. Gauss, "Supplementum Theoriae Combinations Observationum Erroribus Minimis Obnoxiae" (Göttingen, 1826) Werke, vol. 4, art. 11.

86. W. E. Deming, Statistical Adjustment of Data (John Wiley and Sons, Inc., New York, 1943), Chap. 4.

87. J. P. Berge, F. Solmitz, and H. Taft, Digital-Computer Analysis of Data from Bubble Chamber III. Rev. Sci. Instr. (submitted to The Kinematical Analysis of Interaction Vertices (UCRL-9097, March 1960).

88. Lamek Hulthén and Masao Sugawara, Encyclopedia of Physics (Springer Verlag, Berlin, 1957), Vol. 34, p. 2.

89. R. A. Fisher, Statistical Methods for Research Workers, 12th ed. rev. (Hafner, New York, 1954).

90. P. Cziffra and M. J. Moravcsik, "A Practical Guide to the Method of Least Squares," UCRL-8523, Oct. 1958.

This report was prepared as an account of Government sponsored work. Neither the United States, nor the Commission, nor any person acting on behalf of the Commission:

A. Makes any warranty or representation, expressed or implied, with respect to the accuracy, completeness, or usefulness of the information contained in this report, or that the use of any information, apparatus, method, or process disclosed in this report may not infringe privately owned rights; or

B. Assumes any liabilities with respect to the use of, or for damages resulting from the use of any information, apparatus, method, or process disclosed in this report.

As used in the above, "person acting on behalf of the Commission" includes any employee or contractor of the Commission, or employee of such contractor, to the extent that such employee or contractor of the Commission, or employee of such contractor prepares, disseminates, or provides access to, any information pursuant to his employment or contract with the Commission, or his employment with such contractor.